

Quantum Spin Hall Effect

A new generation of microstructures

Dissertation

zur Erlangung des naturwissenschaftlichen Doktorgrades
der Julius-Maximilians-Universität Würzburg
vorgelegt von

Michel Kalle Bendias

aus Sulz am Neckar



Würzburg, 2017



Eingereicht am:

bei der Fakultät für Physik und Astronomie

1. Gutachter: Prof. Dr. Hartmut Buhmann

2. Gutachter: Prof. Dr. Jens Pflaum

3. Gutachter: Prof. Dr. Björn Trauzettel

der Dissertation

Vorsitzender: Prof. Dr. Fakher Assaad

1. Prüfer: Prof. Dr. Hartmut Buhmann

2. Prüfer: Prof. Dr. Jens Pflaum

3. Prüfer: Prof. Dr. Björn Trauzettel

im Promotionskolloquium

Tag des Promotionskolloquiums: 13.07.2018

Doktorurkunde ausgehändigt am:

To all my friends.

Contents

I Introduction

Quantum Spin Hall States	3
------------------------------------	---

II Development

1 The Hall Bar Process	10
State of the Art	10
Photo Resist ARU 4040	11
Positive Photo Resist ECI 3012	12
Technistrip P1316	13
Negative Photo Resist ARN 4340	14
1.1 The Novel Hall Bar Process	16
Hall Measurements	17
2 Efficient Gate Control of the Charge Carrier Density	20
Low Temperature ALD	21
3 Wet Etch Process	28
A Comparison of wet and dry etch process	28
The Conventional Dry Etch Method	31
The Wet Etch	33
3.1 The Wet Etch Evolution	36
Free Standing Structures	39
Etch Progression	40
The Frame	41
3.2 The Sample Story	46
Q2745 I	46
Q2745 III	48
QC0167	49
Novel Contact Metalization	52
Q2745 IV	53
QC0285	55

QC0348	58
QC0347 I, II and III - Contact Configuration	61
QC0167 II, QC0348 - MIBK-Cleaning	66
3.3 The Novel Micro Hall Bar Process	69

III Quantum Spin Hall

1 Quantum Spin Hall Effect	76
Backscattering	76
Potential Inhomogeneities	82
1.1 Temperature and Magnetic Field Dependence	85
QC0285	85
Q2745 V	91
1.2 Nonlocal Resistance	95
Q2745 V	95

Summary and outlook

Summary	100
Outlook	103
Zusammenfassung	104
References	108
Acknowledgments	117
List of Publications	118

Part I

Introduction

Quantum Computation - In a nutshell

Information in conventional computation is stored in bits (binary digits). A bit can have one of two values, 0 and 1, and the amount of encoded information is proportional to n , the number of bits.

Quantum computation, however, relies on fundamental principles of quantum mechanics. A quantum-bit (qubit) state $|\Psi\rangle$ can therefore be described as the superposition of two other states, $|0\rangle$ and $|1\rangle$ in the proportions α and β :

$$|\Psi\rangle = \alpha |0\rangle + \beta |1\rangle .$$

The information encoded in n of such 2-level systems doubles for each additional qubit and scales exponentially with 2^n .

Once realized, the enormous computational power of a quantum computer will have consequences in and beyond our everyday life. Quantum algorithms are proposed to solve any quantum system and thereby allow to simulate chemical reactions and complex molecules. New search algorithms have the potential to escalate the significance of big data and enable tremendous commercial success. The factorization of large integer numbers is supposed to become easy in an exponential speedup [1]. The encryption of data by such integer numbers is broadly used, e.g. in internet security, banking and military communication. However, breaking the state-of-the-art encryption would require an advanced model with millions of entangled qubits [2].

Ironically, quantum cryptography might enable a fully confidential data transfer. Once the information of a quantum state is read out, it is destroyed and the receiver will immediately know, as the signal randomizes.

Since proposed around 1980, the interest in quantum computing has accelerated to a race. The prospects of potential applications have lead to an enormous scientific effort towards quantum computation. Google, Microsoft, IBM and others are working on commercial use. Considering the technological and strategical advantage, it comes as no surprise that the NSA also takes part in the competition [3].

There are different approaches and concepts on how to engineer a quantum computer. Google and others are putting effort in systems with superposition of ground ($E=0$; $|0\rangle$) and excited state ($E>0$; $|1\rangle$). They claim to perform a computation that is beyond even the most powerful "classical" supercomputers already this year [4]. However, the decay of excited states into their ground state leads to quantum decoherence and thereby to errors.

Microsoft is therefore focusing on the development of a topological quantum computer. Proposed in 2003, the computation might become fault-tolerant by a spacial separation

and topological protection of superposed zero energy states [5]. Local disturbances of the system have no influence on the states entangled over distance. In their ground state and without energetic excitation, decoherence is excluded. As for two different knots, that cannot be transformed into each other, the information is robustly stored in the topology of the system. The actual computation is then executed by moving the so called anyons around each other in a process named braiding [6]. Employing Leo Kouwenhoven in 2016, Microsoft is not the first company to hire famous fundamental researchers in expectation of device fabrication. Two Majorana zero modes, found at the interface of superconductor and semiconductor in nanowire devices by his group in 2012 [7], are predicted to form one anyon. Kouwenhoven is cited to tell his students, 2017 would be the year of braiding [4].

However a different system, our HgTe QW structures are also foreseen to host Majorana states when their one-dimensional Quantum Spin Hall (QSH) edge channels are in proximity to a superconductor [8, 9]. The discovery of the QSH effect by König et al. in 2007, is considered a scientific sensation [10]. It complements insulators, semiconductors and metals by a new class of material: the topological insulator. Predicted first to exist in graphene (2005), then in HgTe quantum well structures (2006), it took only months to publish experimental proof [11, 12, 13].

In the QSH phase, electrons of opposite spins counter-propagate at their ground state in two channels along the edge of a sample with insulating bulk. As they are asymmetric in their wave functions, the electrons have nowhere to backscatter.

Leaving aside the hype about possible applications in Majorana detection and Quantum Computing devices, the unique properties of topological insulators remain fundamental research. The length of a proper quantized spin Hall edge channel has never been reported to exceed four micrometer. Although predicted to be protected by its topology, backscattering is present in almost every sample. Many reasons are discussed within the theoretical community. However, due to the lack of data, none has been approved experimentally.

Here, a re-evaluation of every single lithography step in the fabrication process will be described, leading to a new generation of microstructures. Its development is further motivated by an introduction into the specific properties of the topological phase in HgTe QWs.

Quantum Spin Hall States

In the Bohr-model of atoms, electrons are orbiting the positive charged nucleolus on discrete and quantized energy levels. Built into the lattice structure of a solid, the orbitals of the single atoms are interconnecting to bands of electronic states and forbidden areas

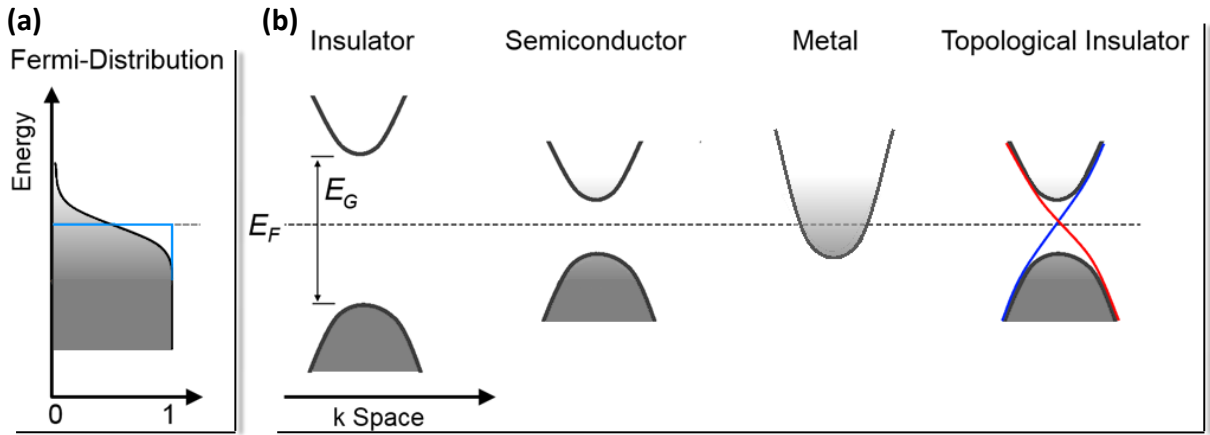


Figure 0.1: **(a)**, Fermi distribution for zero temperature (blue) and with temperature broadening from gray (occupied) to white (unoccupied). **(b)**, schematic of the energy dispersion in k-space around the Fermi level E_F , characterizing four different classes of material.

(energy gap). If states are available, an electron can propagate through the lattice and the solid is conducting. The amount of electrons in the system and the energy level up to which they fill available states in the characteristic energy bands thereby determine their class.

At ideal zero temperature, all electrons are at their lowest energy state and fill the bands up to a discrete level. Above this Fermi level, all states are empty (white), below all are occupied (gray). At finite temperature, the step-like Fermi function (blue) in Figure 0.1 **(a)** broadens following a Boltzmann distribution. Temperature activated electrons from below the Fermi level now reach states in the Boltzmann tail above. For classical systems the broadening can be estimated to $2k_B T$ in energy, with k_B being the Boltzmann-constant. At room temperature, this corresponds to an energy window of 25.8 meV in which excited electrons can occupy states around the Fermi level.

Figure 0.1 **(b)** schematically depicts relevant energy bands close to the Fermi level for different classes of solids in reciprocal space (k).

Insulators have a large band gap (E_G). Even at room temperature, electrons cannot reach from the fully occupied band below, to the unoccupied band above the Fermi level. No current is flowing.

In semiconductors, the smaller band gap remains insulating at low temperatures. If $k_B T$ is high enough to excite electrons over the band gap, they can freely propagate via available empty states in the conduction band. The solid acts as an insulator at low temperatures and a conductor at elevated temperatures.

In metals, the relevant band at the Fermi level is half occupied. The electrons can conduct at all temperatures.

Topological insulators at low temperatures have a insulating bulk, but conducting surface states (red and blue). Electrons exclusively conduct in highly mobile states along the material surface.

The topological surface states arise from an inversion of bands at the Γ -point in the band dispersion. Figure 0.2 (a) shows the relevant bands close to the Fermi level (dashed line) for a trivial band ordering (CdTe) and an inverted band structure (HgTe) [14]. Due to strong spin-orbit coupling and relativistic corrections, the positions of the two degenerate $|p\rangle$ -like Γ_8 -bands in HgTe are found to lay above the $|s\rangle$ -like Γ_6 band. The $|p\rangle$ - and $|s\rangle$ -type arise from the symmetries of the orbital forming the band. Their ground states are marked with red ($\Gamma_{6;(\frac{1}{2})}$) and blue dots ($\Gamma_{8;(\frac{1}{2},\frac{3}{2})}$). Inverted and with no effective band gap, pure HgTe is a semimetal.

Grown as a sandwich layer in (Cd,Hg)Te/HgTe/(Cd,Hg)Te quantum wells, the reduced degrees of freedom lead to a further quantization of the energy bands. The degeneracy of $\Gamma_{8;(\frac{1}{2})}$ and $\Gamma_{8;(\frac{3}{2})}$ is thereby lifted and an energy gap opens up [12]. In Figure 0.2 (b), the energy of the ground states in the quantized subbands are plotted against the HgTe QW thickness. Whereas lifted for strong confinement below 6.3 nm, the inversion of E1 ($\Gamma_{6;(\frac{1}{2})}$) and H1 ($\Gamma_{8;(\frac{1}{2})}$) remains in QWs of thicker layers. Within the gray marked area in

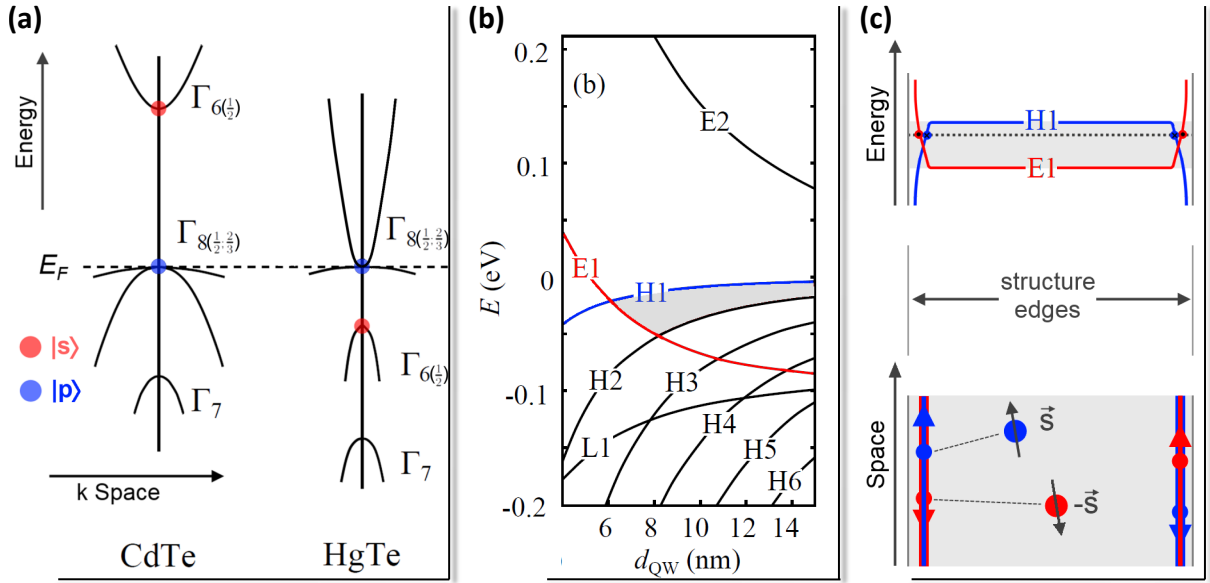


Figure 0.2: (a) Schematic energy dispersion for a trivial (CdTe) and an inverted band ordering (HgTe) around the Fermi level. From [14] (modified). (b) Subband energies at the Γ -point as function of quantum well thickness d_{QW} . The inverted regime is marked in gray. From [29] (modified). (c) Energy of the lowest subbands versus the sample dimensions (on top) and the QSH edge channels resulting from the reversed band inversion along the edges (below).

Figure 0.2 (b) and (c), the confinement opens an energy gap of up to 22 meV. The bulk therefore remains insulating when the Fermi level is in the energy gap and the temperature low enough. The band inversion, however, needs to adopt to the trivial symmetry of the outside. H1 (blue) and E1 (red) interchange in energy towards the edge of the sample, restoring the trivial band ordering [See Fig. 0.2 (c)]. At the Fermi level, electronic states are now available on the edges of the sample. Two edge channels of electrons with opposite spins are moving in opposite directions. Asymmetric in the spin component of their wave functions and in absence of magnetic impurities, electrons cannot backscatter into the counter propagating edge channel. Protected through topology, the zero energy modes are always present and no net current is flowing.

If a voltage is applied along a stripe of such a HgTe QW, the resistance along one edge of the sample quantizes to $h/2e^2$ in the pure QSH phase. This corresponds to the conductance of two one-dimensional channels. Its measurement in 2007 is considered the first experimental prove of the QSH effect [10]. In the following years, Molenkamp et al. further have proven the ballistic edge channel character by nonlocal resistance [15], with micro squid measurements [16] and via induced superconductivity [17]. The localization width is thereby determined from 180 to 408 nm. The spin polarizations are found to be perpendicular to the plane of the QW [18]. In hybrid structures, the QSH effect has been used as a spin current injector and detector for the metallic spin Hall effect, thereby allowing an all-electrical detection of spin polarization.

The QSH effect is increasingly foreseen in some material systems, but experimentally confirmed in very few. Until today, only one other quantized measurement of the QSH conductance has been published in InAs/GaSb double QW [19]. Other than through the thickness of the QWs in HgTe, the inversion is achieved by gate-tuning an electron-like in one, and a hole-like band in another QW of an InAs/GaSb double QWs structure [20, 21]. A recent candidate is a monolayer of tungsten ditelluride (WTe₂). For now it reaches half the conductance [22] and is approved by ARPES methods to host QSH states [23].

Even though predicted to be topologically protected by time-reversal symmetry, the length of a proper quantized spin Hall edge channel has never been reported to exceed a 4 μm [24, 25, 13, 15]. Possible explanations for the breakdown of the quantized conductance in the QSH regime in longer devices are subject of current research, where e.g. inelastic scattering accompanied by electron-electron interactions [26], Rashba-puddles tunnel coupled to the QSH edge states [18, 27], two-particle- and/or Kondo-back-scattering have been theoretically discussed [28].

In order to observe the QSH effect it appears to be essential to fabricate structures with a homogeneous density distribution and a minimum of scatterers. Good figures of merit are the mobility μ or the elastic mean free path (λ_{mfp}). The presence of scatterers limits both μ and λ_{mfp} .

Mobilities of $2\text{-}5 \times 10^5 \text{ cm}^2/\text{Vs}$ are routinely obtained due to good crystalline quality of molecular beam epitaxial (MBE) grown HgTe-QWs for carrier densities of a few 10^{11} cm^{-2} . This corresponds to a mean free path of several micrometers. However, using conventional ion milling, the mobility severely decreases when defining devices in a few micrometer range.

Here, we present a new fabrication route which provides a superior alternative to overcome severe damages on micro-structures caused by routinely used ion-milling based processes. Instead of physical etching, a chemical wet etch solution is used to shape the micro-structures. It leaves the crystalline structure of the material undamaged and permits to examine the intrinsic material parameters as well as to perform experiments with sample dimensions $\geq \lambda_{mfp}$.

A re-evaluation of every single lithography step in *Development*, furthermore leads to a robust and easy to handle fabrication process. The reader is invited to follow and understand the changes step by step. From the optical lithography techniques in *The Hall Bar Process*, to a novel insulator gate electrode application in *Efficient Gate Control of the Charge Carrier Density* and the novel chemical mesa etch method in *Wet Etch Process*, the changes can be traced in micrographs, scanning electron microscope images and most of all measurement feedbacks.

In *The Wet Etch Evolution* the process details, design requirements and particularities of the novel mesa fabrication can be followed throughout their developments. *The Sample Story* then allows a qualitative evaluation of the improving measurement signals from the very first wet etched sample to the current state of the art, summarized in *The Novel Micro Hall Bar Process*.

Measurements of the QSH resistances are presented in unprecedented quality and details in *The Quantum Spin Hall Effect*. Their temperature and magnetic field dependence give an idea of the complex interplay of possible backscattering mechanisms. Characteristic features provide experimental data to the widely discussed theories on backscattering in QSH edge channels. The measurements presented here, represent the best realization of the QSH effect since its discovery in 2007 and thus emphasize the impact of this work.

Part II

Development

The Hall Bar Process

Optical lithography is the working horse of sample preparation. Optical resists allow to define resist patterns with a resolution down to 1 μm . They are used in the fabrication processes of all sample types. Even high resolution devices, fabricated with electron microscope lithography (EBL) techniques, require optically defined mesas, contact leads and gate electrodes. Eliminating its error-prone increases the general processability, output and quality of all devices.

Here, developed improvements are presented along the example of the standard characterization Hall bar process. Hall measurements allow to extract information such as the carrier density n and their mobility μ , characterizing the wafers [see Hall measurements on page 18]. An insulated gate electrode allows to tune n and conduct experiments at different carrier densities. The formerly used process is shown in the beginning, its challenges and solutions are discussed and *The Novel Hall Bar Process* is presented at the end of this chapter.

Figure 1.1 shows four steps of the old Hall bar process:

First, the wafer is spin-coated with ARU 4040 at 6000 rpm for 20 s. The 1.2 μm thick optical positive resist is baked at 80 $^{\circ}\text{C}$ for two minutes. In a mask aligner the surface is brought into contact with a partly transparent glass mask with chromium coverage in mesa shape. Exposed with the i-line of a mercury vapor lamp, the resist is solved in the developer AR 300-26 within 40 s. The mask-covered areas remain, while the exposed areas are gone and the wafer is revealed. Accelerated Ar^+ -ions are then used to physically etch the wafer beneath the conductive layer. The ion milling process is conducted in an ultra high vacuum (UHV) chamber with an ion current of 8 mA at 1 kV energy. Acetone at 50 $^{\circ}\text{C}$ and excited in an ultrasonic bath solves the resist. An image of the mesa structure taken with the optical microscope is shown in Figure 1.1 (a). The elevated light brown structure are the mesas of the $(200 \times 600) \mu\text{m}^2$ and the $(10 \times 30) \mu\text{m}^2$ Hall bar and their contact leads.

Second, the ion milling is repeated with the same process on the area of the later ohmic contacts. The insulating (Cd,Hg)Te capping is etched down, 20 nm close to the conductive HgTe layer [see Fig. 1.1 (b)].

Third, an insulator stack of eleven layers of alternating 10 nm SiO_2 and 10 nm Si_3N_4 is homogeneously grown via plasma-enhanced vapor deposition (PECVD)[see *Insulator* on page 20]. A wet etch mask is defined with the above described ARU 4040 process, covering the Hall bars and parts of the conduction leads. The uncovered insulator is etched away

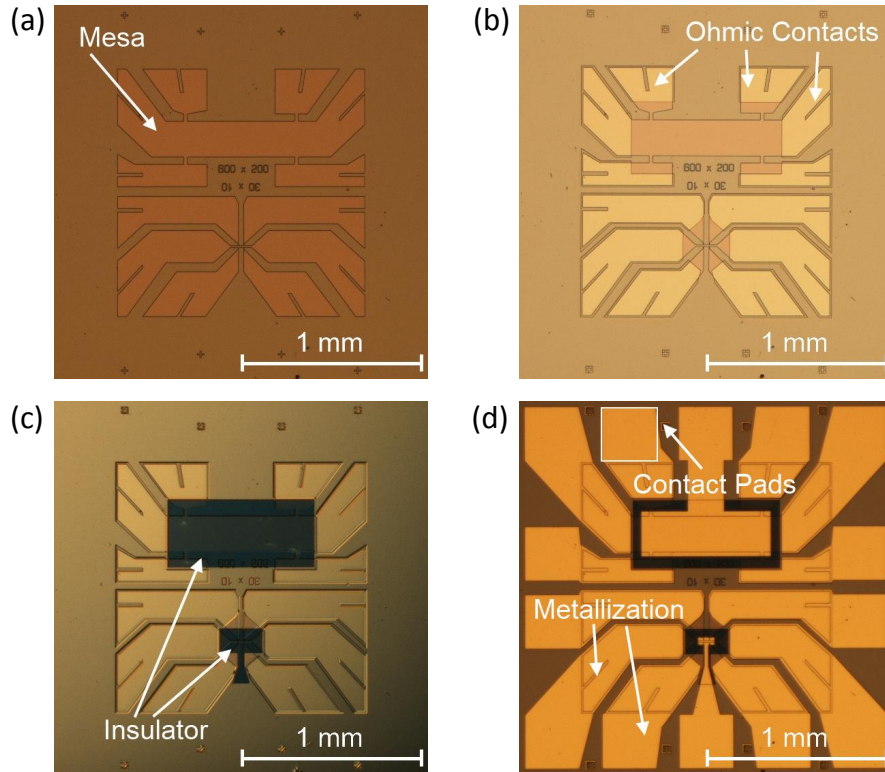


Figure 1.1: Previous Hall bar process: **(a)** Mesa definition, **(b)** cap layer removal via ion milling for ohmic contacts preparation, **(c)** insulator application and etching and **(d)** metallization of the ohmic contacts and gate electrode.

with buffered oxide etch, the mask stripped in acetone. The result is shown in Figure 1.1 **(c)**.

Forth, once again the ARU 4040 is spin-coated, exposed and developed. Metalized with e-gun evaporated AuGe (50 nm) and Au (50 nm) the resist is stripped in acetone. Only the metal layer on the ohmic contacts of the mesa, the contact pads and the gate electrode remain [see Fig. 1.1 **(d)**].

The challenges and solutions leading to a novel Hall bar process, are now discussed in order of appearance throughout the lithographic process.

The ARU 4040, if only baked out at 80°C, is comparably sensitive to UV light. This does not only lead to short exposure times of 2.6 s (8 W), but also to an unwanted development of partly exposed resist. The shape of the resist profile is not suitable for ion milling processes. The secondary electron microscope (SEM) image in Figure 1.2 **(a)** shows the etch mask of an later alignment cross. The simple cross of the shadow mask is deformed by the deflection exposition at the edges and the dark solubility results in an

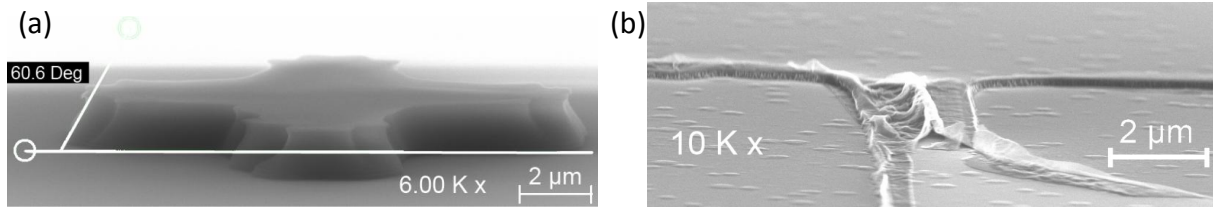


Figure 1.2: (a) SEM image of an ARU 4040 resist mask. (b) SEM image of the mesa after ion milling and the acetone stripping. Remaining sidewalls are folded onto the voltage probe of the Hall bar. The spots on the surface originate from growth defects.

side angle of about 60° . Thus, the resist edge is exposed to the Ar^+ in the ion milling of mesa and ohmic contacts. Its surface hardens out and the cross-linked resist mixes with redepositing material sputtered away in the etched area. As a consequence, hardened organic resist and II-VI-redeposition material form a compound that does not dissolve easily. Even after the lift-off and intense acetone and ultrasonic (US)-bath treatment, the compound remains as sidewalls. The SEM image in Figure 1.2 (b) shows them folded onto the mesa of the voltage probes of a small Hall bar. It is easy to imagine that those sidewalls will not only cause problems in the subsequent lithography steps such as the insulator deposition and insulator etch, but will also create an inhomogeneous potential beneath the later applied gate electrode.

Two measures are taken to minimize the risk of sidewalls. The resist is exchanged with the better performing positive resist *ECI 3012* and the stripping is supported by the combination of organic and inorganic solvents in *Technistrip P1316*.

The ECI 3012 results in a $1.4\ \mu\text{m}$ thick layer, if spin-coated at 6000 rpm and baked for 2 min at 80°C (10°C below the recommended process temperature). The optimal resist shape is achieved at 5.6 s exposure time (8 W) and 22 s development in *AZ 726 MIF* [see Fig. 1.3 (a)]. The cross shape of the photo mask is properly transferred onto the wafer. Exhibiting an side angle of 77° , the result is 15° steeper than that of the best outcome with *ARU 4040*. Therefore, the resist edge is less exposed to the Ar^+ milling,

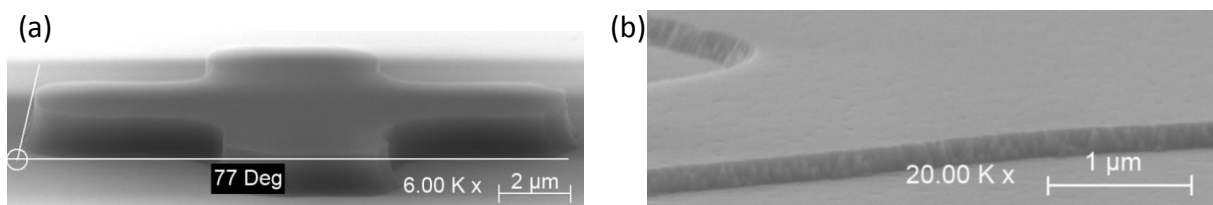


Figure 1.3: (a) SEM image of an *ECI 3012* resist mask. (b) SEM image of the mesa after ion milling, the acetone and Technistrip P1316 stripping.

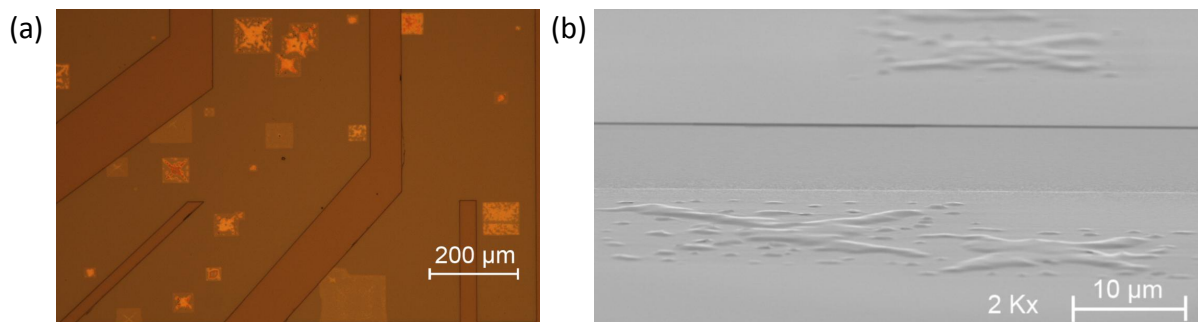


Figure 1.4: Images of the Technistrip defects arising on the mesa of specific wafers during the stripping taken with (a) an optical microscope and (b) an SEM.

fewer resist cross-links and the component is more solvable in the stripping. However reduced, the risk of sidewalls is still present.

Technistrip P1316 is an industrial stripper, used to solve cross-linked photo resist and residuals. Directly after the acetone stripping, the sample is treated for 5 min in 50°C *Technistrip P1316* combined with an US-bath. This reliably removes the sidewalls. Figure 1.3 (b) shows an SEM image of the mesa after *Technistrip P1316* stripping. No sidewalls remain and the resist mask is completely stripped.

More than fifty characterization samples have been fabricated with Technistrip P1316. No influence can be determined on the carrier density, nor the mobility. However, some specific wafers suffer severe damage from *Technistrip P1316*. Figure 1.4 (a) shows an optical microscope image of a damaged mesa structure after the stripping. The defects in different stages can only be seen on the mesa, not in the etched area. Their rectangular shape has orientations along the $(1\bar{1}0)$ and (110) crystalline direction of the wafer. Their sizes scale from several to over hundred micrometers. The yellowish, partly diagonal cross-like structures within the rectangles, are elevated [comp. Fig. 1.4 (b)]. In the affected areas without elevated parts, the cap layer of the wafer is gone.

If exposed to *Technistrip P1316*, both, an untreated piece and a wafer piece solely covered and striped with the resist process, do not show those defects. Only if resist and ion milling are combined, the Technistrip treatment is selectively etching the crystal defects of those wafers.

This irregularity is only arising on wafers on GaAs-substrates which have been taken out of the UHV after the CdTe-buffer growth, cleaved in smaller peaces, etched with hydrogen chloride (HCl) and then one by one overgrown with the (Cd,Hg)Te/HgTe/(Cd,Hg)Te layer stack. Hall measurements on samples of those wafers, produced without Technistrip, show an elevated intrinsic carrier density and a reduced mobility. This allows to draw the conclusion, that their defect density is much higher and the Technistrip P1316 is effectively etching the growth defects arising from the intermediate treatment during growth. As a consequence, this type of wafer growth is no longer practiced.

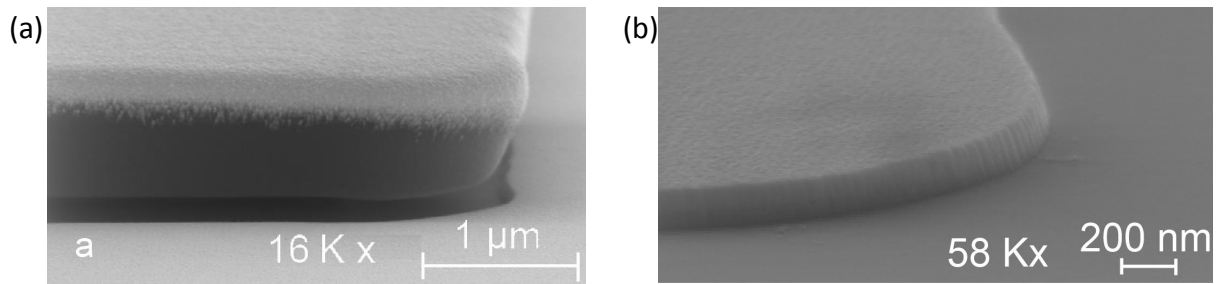


Figure 1.5: Images of the Technistrip defects arising on the mesa of specific wafers during the stripping taken with (a) an optical microscope and (b) an SEM.

The negative resist ARN 4340 replaces the *ARU 4040* positive resist in the lift-off for the metalization. As shown in Figure 1.2 (a), the *ARU 4040* exhibits an profile angle of about 60 deg. During the metalization, material is therefore also deposited along the edges of the resist. After the striping, it can partly remain as metalization sidewalls. The better suited negative resist *ARN 4340* is applied with the spin-coater at 6000 rpm for 20 s and baked out for 2 min at 80 °C, resulting in a 1.3 μm thick layer. Exposed for 20 s (8 W) and post exposure baked (PEB) for 6 min at 80 °C the exposure-activated short polymer chains are linked during the PEB. The non-exposed area beneath the shadow mask is then stripped during the development in *AR 300-47*, the previously exposed areas are remaining. Three main advantages arise from the use of the negative resist:

First, the shadow mask is transparent on most of the sample piece and chromium covered on the area of the later metal. In contrast to positive resist, this allows to see most of the sample during the alignment in the mask aligner, reducing the risk of scrunching the sample, when the mask is approached to contact.

Second, an undercut can be created during the development. If developed for 35 s the unexposed areas of the resist are fully removed and the resist edge has an inclination of about 90°. Longer development up to 60 s leads to an undercut, with an only minor loss of resolution in the upper resist layer. Figure 1.5 (a) shows the SEM image of an *ARN 4340* lift-off mask after 45 s of development and e-gun evaporation of 150 nm Au. With a positive resist masks the edge of the resist [comp. resist masks in Fig. 1.2 (a) and Fig. 1.3] is covered during the directed e-gun evaporation. Sidewalls remain on the verge of the metal layer and the lift-off requires a US bath. Here, the metal does not cover the resist edge. The resist is easy to access, which allows a simple lift-off in acetone and results in a deposition layer of homogeneous thickness [see Fig. 1.5 (b)].

Third, the *ARN 4340* can also be used as a resist mask for ion milling. This enables to combine the (Cd,Hg)Te-cap layer removal [see Fig. 1.1 (b)] and the metalization of the ohmic contacts [see Fig. 1.1 (d)] into one step. The ion milling chamber is connected

with the e-gun metalization chamber via UHV transfer. Thus, surface oxidation and contamination due to the insulator application and HF-etching (Fig. 1.1 (c)) at the contact interface can be avoided.

The above mentioned advantages of the novel resist systems for the optical lithography processes are implemented into the sample fabrication. In the following, the improvements are summarized along the novel Hall bar process and changes in the mask design are discussed.

1.1 The Novel Hall Bar Process

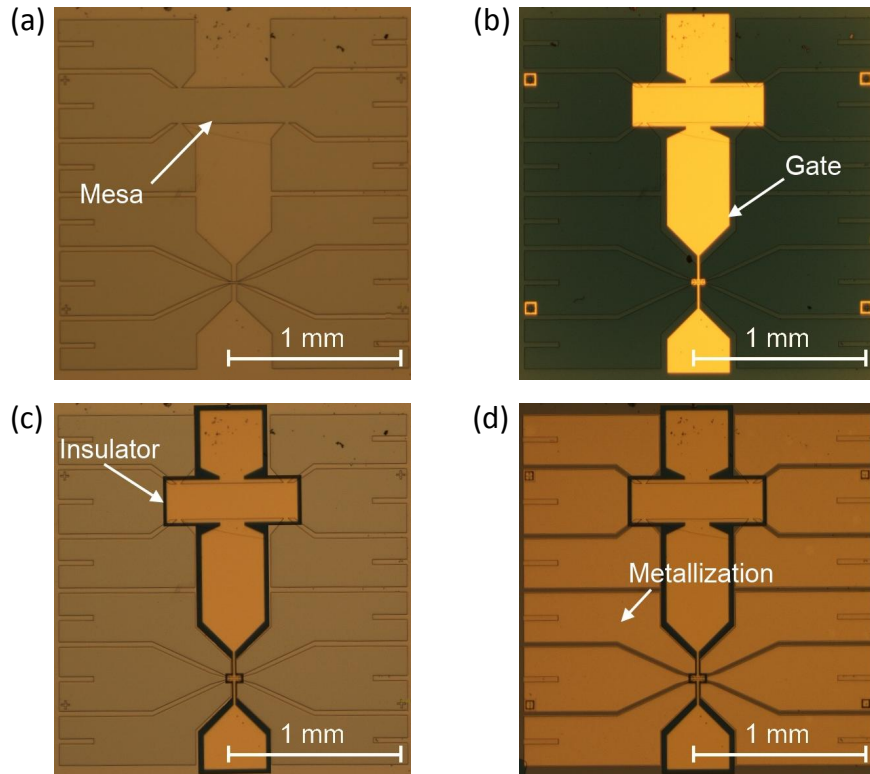


Figure 1.6: Novel Hall bar process. **(a)** Mesa definition, **(b)** insulator application and gate metalization. **(c)** Insulator etching. **(d)** In situ cap layer removal and metalization of the ohmic contacts.

Figure 1.6 shows four steps of the improved sample fabrication process.

(a) The piece of wafer is spin-coated with the *ECI 3012*, baked, exposed, and developed. Ion milling below the conductive layer defines the shape of the conductive Hall bar and leads. The resist mask is first stripped in 50°C acetone, then in *Technistrip P1316*.

(b) In contrast to the previous process, the gate is defined directly after the mesa step. PECVD insulator is applied homogeneously. The gates are deposited using the novel *ARN 4340* lift-off process.

(c) An *ECI 3012* wet etch mask is processed, the insulator removed with HF and the mask is stripped in acetone.

(d) An *ARN 4340* lift-off and etch mask is fabricated. The (Cd,Hg)Te-cap layer is removed via ion milling, the sample is transferred in situ to the e-gun evaporation chamber and metalized with 50 nm AuGe/50 nm Au. The lift-off in acetone reveals the ohmic contacts and contact pads. The mesa is enlarged, as the design is changed. The leads are extended further out and increase the area of the ohmic contacts. The use of *ECI 3012* and *Technistrip P1316* in the process leaves no sidewalls whatsoever. Applying the insulator and gate directly after the mesa definition ensures a minimum of residuals at the

interface. Clean and without sidewalls, the insulator is less likely to crack or be under-etched during the gate and insulator etch process. The use of *ARN 4340* and separation of gate and contact metalization allows to combine the cap-layer removal in situ with the metalization of the ohmic contacts. Thus, the contact interface is clean and the adhesion of the bonding pads is maximized. No more pads are ripped off, when the sample is connected with a chip carrier using Au wires in the later wedge bonding.

Hall Measurements. Magneto resistance measurements in magnetic field perpendicular to the QW and sample surface are conducted at 4.2 K. Figure 1.7 (c) shows a schematic of the sample. A current is sent from contact 1 to 4, the Hall voltage U_{xy} is measured perpendicular to the current (contacts 2 and 6, or 3 and 5), the longitudinal voltage U_{xx} is measured along the current path (contacts 2 and 3, or 6 and 5). Both are normalized with the sample current. A measurement of a $(200 \times 600) \mu\text{m}^2$ Hall bar is displayed in Figure 1.7 (a) with the longitudinal (black) and Hall resistance (red) as a function of magnetic field. The Hall resistance in low magnetic fields follows a linear increase. The proportionality is given by the Hall coefficient $R_H = -1/ne$ and, with the elementary charge e , allows to conclude on the carrier density n within the system [32]. The longitudinal resistance at zero magnetic field serves to infer the mobility μ at this given density via the resistivity $\rho_{xx}(\text{O T}) = 1/en\mu$.

With increasing magnetic field the quantization in Landau levels is resolved and the Hall resistance evolves in plateaus at quantized resistance, the quantum Hall effect (QHE). Figure 1.7 (b) shows a schematic of the Landau energies along a cut through a mesa. The continuous adaptations of the Landau levels to the vacuum energy at the sample edge lead to an intersection with the Fermi energy. This gives rise to quantum Hall edge states. Edge channels are counter-propagating along each mesa side, spatially separated and with nowhere to backscatter. Every edge channel carries a conductance precisely quantized at the fundamental unit of the von Klitzing constant e^2/h , whereas h is the Planck constant.

In higher magnetic field, the Landau levels are further split and one by one lifted above the Fermi level. With only one ballistic edge channel contributing (filling factor $\nu = 1$), the Hall resistance quantizes in the von-Klitzing-constant $R_K = h/e^2 = 25812.807557(18) \Omega$ [33, 35]. Once the Landau splitting is larger than the temperature broadening of the Fermi energy, the described effect can be observed in the measurements. Above a magnetic field of 1 T, the Hall resistance (red) in Figure 1.7 (a) develops from the linear Hall into the plateau-like Quantum Hall regime. At plateau-to-plateau transitions of R_{xy} , the longitudinal resistance R_{xx} (black) increases to peaks. These Shubnikov-de-Haas (SdH) oscillations arise from the Landau levels crossing the Fermi energy. With states available in the bulk of the sample, electrons can backscatter into the counter-propagating channel on the other edge [34].

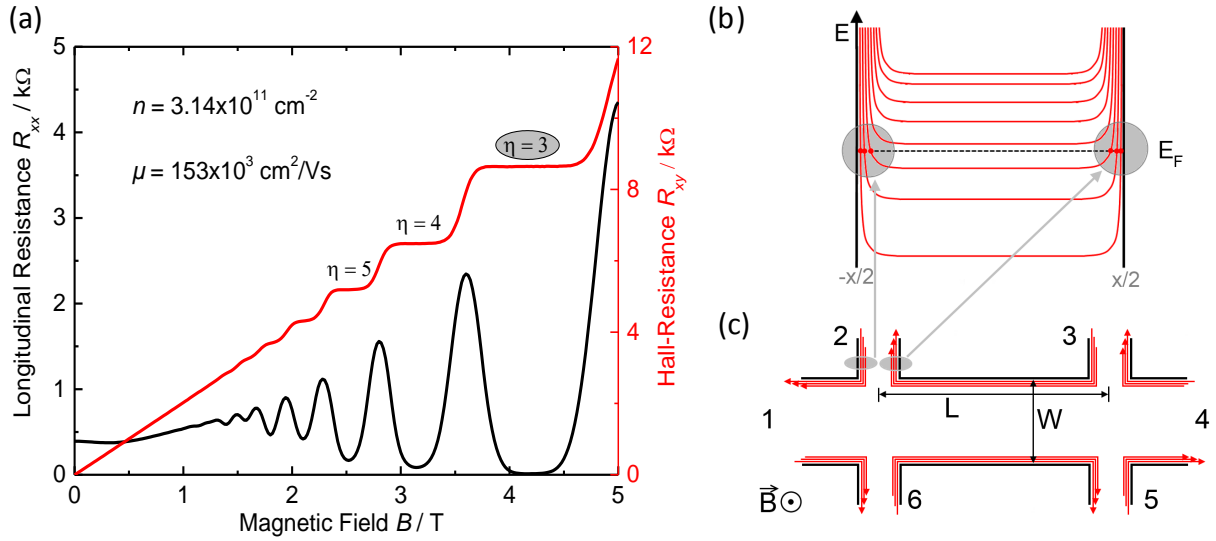


Figure 1.7: **(a)** Longitudinal and Hall resistance measurement of a $(200 \times 600) \mu\text{m}^2$ Hall bar plotted against the magnetic field. The carrier density n is extracted from the linear slope in the Hall regime, the mobility μ then calculated from the R_{xx} at zero Tesla. The filling factor $\nu = 3$ at the corresponding Hall plateau is highlighted in gray. Its occurrence is displayed in **(b)** the schematic of the Landau levels in the Hall bar and **(c)** the schematic of the Hall bar.

Electron density, mobility, and the longitudinal and Hall resistance measurement will be taken as a figure of merit on the sample quality throughout further process development. The density of a sample changes if processes, chemicals or residuals unintentionally dope the sample during lithography. The mobility is lowered if additional scatterers are introduced. Consequently, characteristic SdH oscillations as well as Hall resistance are disturbed when inhomogeneities deform the potential landscape.

Efficient Gate Control of the Charge Carrier Density

Even with the improved mesa quality of the novel Hall bar process, a certain risk remains that the PECVD grown $\text{SiO}_2\text{-Si}_3\text{N}_4$ insulator is under-etched during the HF-etching

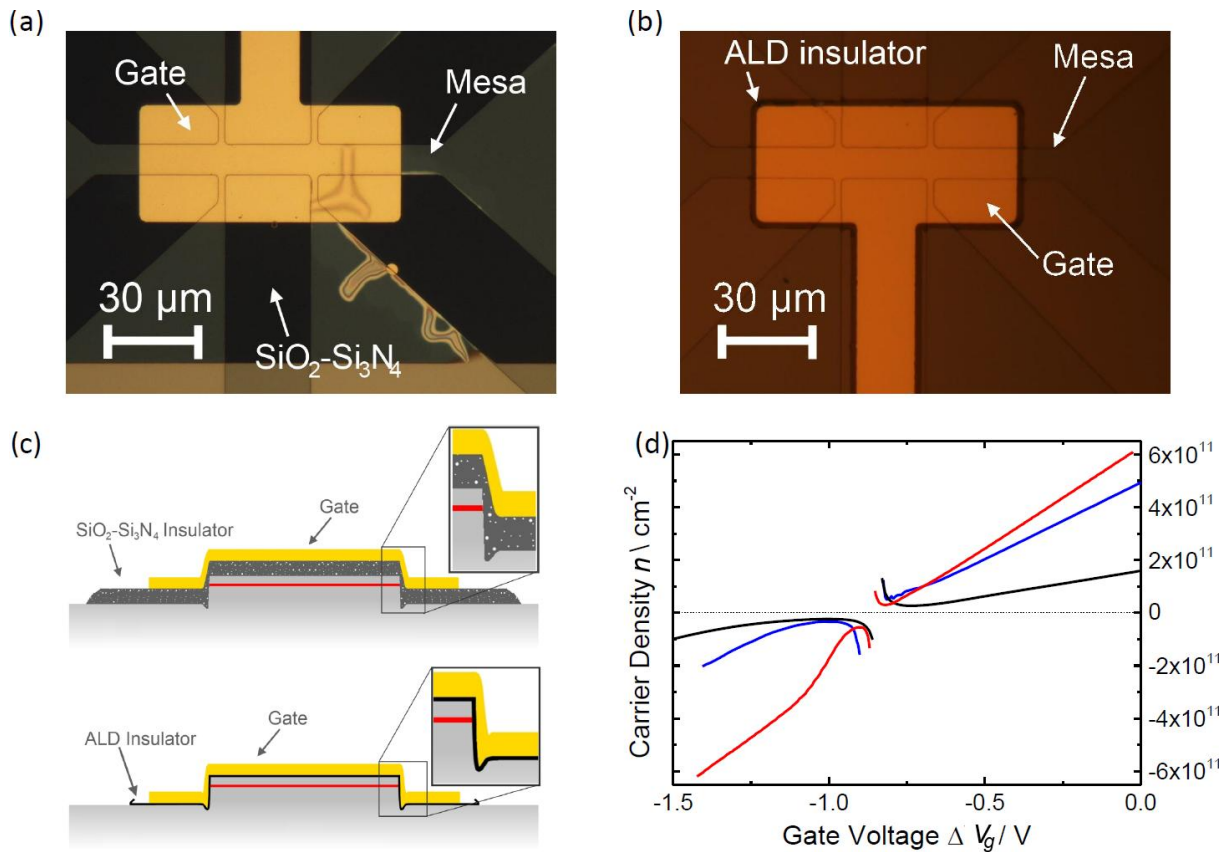


Figure 2.1: **(a)** Image of a Hall bar structure with a $\text{SiO}_2\text{-Si}_3\text{N}_4$ -insulator gate electrode. Resulting in the cracks along the mesa rim, the insulator is damaged during the HF-etching of the outer part. **(b)** Image of a similar Hall bar with an ALD insulator gate electrode. **(c)** Schematic of the two insulator techniques. The inlay shows the insulator at the mesa edge, where $\text{SiO}_2\text{-Si}_3\text{N}_4$ is the thinnest and the ALD insulator is homogeneous. **(d)** The carrier density plotted against the gate voltage for 110 nm $\text{SiO}_2\text{-Si}_3\text{N}_4$ (red), a ~ 30 nm (blue) and ~ 15 nm thick HfO_x insulator (black) on Hall bars of the same wafer.

and the development for the gate metalization. The Tetramethylammoniumhydroxid (TMAH)-based developer *AZ 726 MIF* is known to etch SiO₂ [37]. Despite its low etch rate, the developer can etch underneath the insulating layer if weak spots are present. As the Hf solution, the etchant is most likely to creep along the semiconductor-SiO₂ interface, starting at the mesa edge where the insulator is the thinnest [see inlay in Fig. 2.1 (c)]. Figure 2.1 (a) shows an image of a damaged insulator beneath a gate electrode on a Hall bar structure. This can result in an inhomogeneous gate influence in the best, and a complete malfunction of the device in the worst case. Detailed information on Si based PECVD-grown insulators can be obtained in [38, 39, 40].

An alternative gate insulator composition and application technique has been developed using atomic layer deposition (ALD). Figure 2.1 (b) displays an image of a similar Hall bar with an HfO_x insulator. Due to its layer by layer growth on all surfaces, the ALD insulator covers the mesa surfaces homogeneously [see schematic in Fig. 2.1 c] [41]. The high dielectric constant of $\epsilon_{r,HfO_x} = 25$ and an energy gap of 5.8 eV emphasize its wide used in semiconductor industry, as it enables the processing of thin insulating layers, resulting in high capacitance $C = \epsilon_r \epsilon_0 A/t$ [42]. Here ϵ_0 is the vacuum permittivity, A the planes of the capacitor and t their distance. Consequently, the gate action $G_a = \Delta n(\text{or } p)/\Delta V_g$ of thin HfO₂ insulators is larger than for thick insulators and a gate voltage variation ΔV_g changes the carrier density $n(\text{or } p)$ more efficiently.

Figure 2.1 (d) illustrates the carrier density of three Hall bars with different insulators plotted against the gate voltage difference. The values in the band gaps are omitted. At voltages below -0.8 V, the Hall bars are n , at more negative values p -conducting. For a better comparison, all Hall bars have been structured from the same wafer of a symmetrical (Cd,Hg)Te/HgTe/(Cd,Hg)Te QW (66 nm/8.2 nm/66 nm, QC0063). As expected, the 110 nm SiO₂-Si₃N₄ (black) insulator allows the lowest gate action, the 180 ALD cycles (≈ 30 nm) of HfO_x (blue) an increased and the even thinner 90 ALD cycles (≈ 15 nm) (red) the highest gate action.

However, the gate action itself is not the key to a good gate insulator. The homogeneity of the potential landscape and the hysteresis-free voltage and density range is improving the sample performance in experiments.

The 34 °C low temperature ALD process has two main advantages, processability and layer properties.

Optical photo and electron beam (e-beam) resists can be used for a lift-off process without further cross-linking and hardening. Instead of three separate lithography steps for the PECVD insulator: the SiO₂-Si₃N₄ application, the *ARN 4340* gate metalization and the HF insulator removal with an *ECI 3012* wet etch mask, the ALD gate electrode requires one single step. Therefore, the contamination of the insulator-metal interface with the photo resist *ARN 4340* and the developer *AR 300-47* is avoided and the risk of under-etching is excluded as neither further lift-off development nor Hf-dip is required.

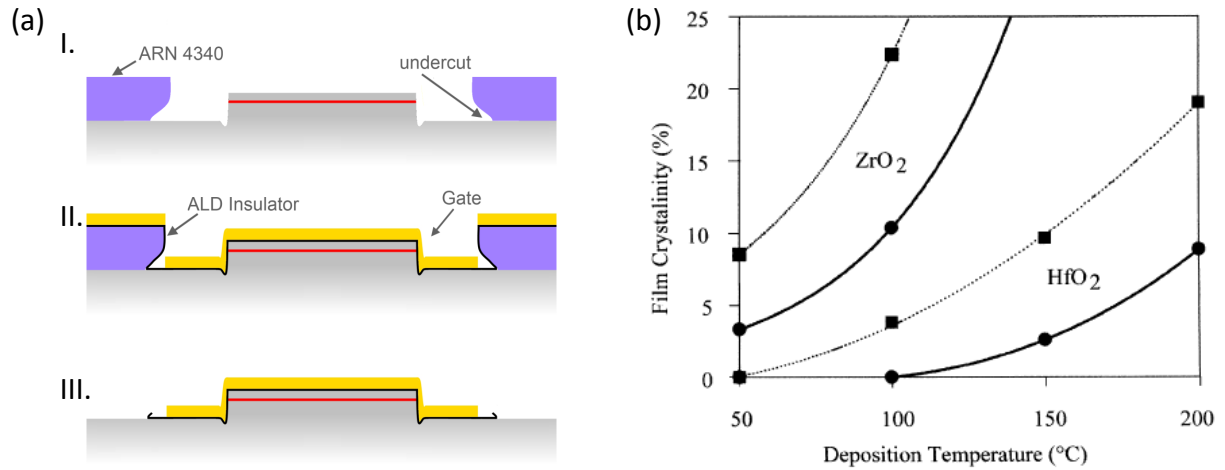


Figure 2.2: (a) Schematic of the self aligned ALD gate process. **I.** The negative resist *ARN 4340* after etching, **II.** after the ALD insulator deposition, and the metal evaporation and **III.** after the lift-off. The undercut determines the oversize of the insulator (b) Film crystallinity of ZrO₂ and HfO₂ plotted against the growth temperature [44].

Figure 2.2 (a) shows the schematics of a self aligned insulator gate application:

I. The negative resist *ARN 4340* is spin-coated, the gate structure exposed and developed after the post exposure bake [see. page 14]. With increasing development time, the resist structure exhibits an undercut.

II. During the ALD, the HfO_x grows layer by layer on all surfaces: the mesa, the resist and into the undercut. The gate electrode can then be metalized using the very same lift-off mask (self aligned).

III. After the lift-off in acetone, the gate remains insulating towards the mesa. Because of the undercut, the insulator turns out slightly bigger than the gate metal [see also 2.1 (b)].

The lower deposition temperature reduces the energy available for atoms to nucleate on the surface and produces films with lower crystallinity and smoother surfaces [44]. The

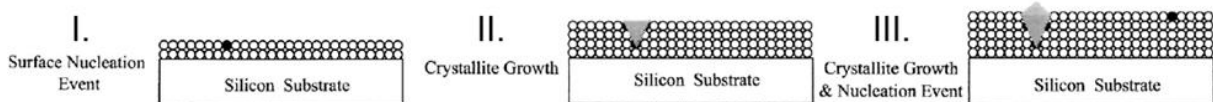


Figure 2.3: Schematic of the crystallite growth during the ALD insulator deposition. Start (**I.**), growth (**II.**) and result (**III.**). The higher the temperature and the thicker the layer, the higher the amount of nucleation events and thus the rougher the surface. Taken from [44].

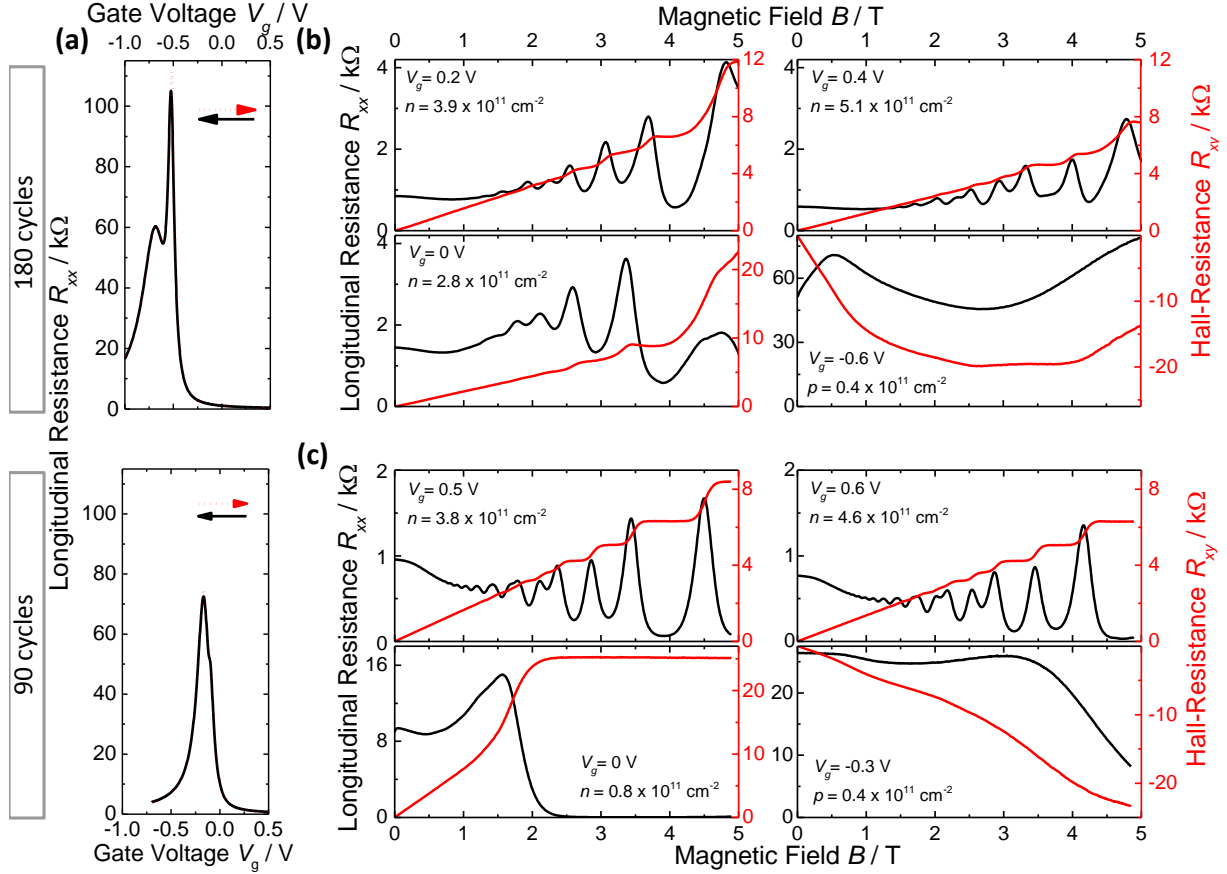


Figure 2.4: Longitudinal resistance R_{xx} plotted against the gate voltage with 180 (top) and 90 ALD cycles of HfO_x insulator (bottom) on a $(200 \times 600) \mu\text{m}^2$ sized Hall bars of QC0063 (a). Longitudinal and Hall resistance plotted against the magnetic field at different gate voltages and densities for the qualitative analysis of the QHE and SdH oscillation of the 180 (b) and 90 cycles (c)

performance of the insulator is reduced by leak current paths along the crystalline grains. Figure 2.2 (b) shows the temperature dependent crystallinity of ALD grown HfO_2 and ZrO_2 determined by atomic force microscope (AFM) (dashed lines) and x-ray diffraction (XRD) (solid lines). Whereas the ZrO_2 deposited at 50°C remains partly crystalline, the HfO_2 grows fully amorphous at lower temperatures and thin films.

However, grown as thick films, the crystallinity is enhanced [44]. Figure 2.3 shows a schematic of an ALD insulator growth. **I.** The nucleation event starts on the film surface. **II.** The crystallite defects grow in pyramidal shape with increasing layer thickness. **III.** With new nucleations on the surface, crystallinity and layer roughness increase the thicker the insulator.

Resistance measurements on HfO_x based Hall bars with ALD-grown insulators of different thickness are compared in Figure 2.4. Whereas the gate sweep on the thin

insulator sample (bottom) follows the expected curvature for low resistance in the n-conducting (positive V_g), maximum resistance in the energy gap ($V_g=0.2$ V) and elevated resistance in the p-conducting regime ($V_g=-0.3$ V), the gate sweep on the thick insulator sample (top) is strongly disturbed [see. Fig 2.4 (a)]. The shoulder in the p-conductive regime at $V_g=-0.7$ V refers to severe potential inhomogeneities within the sample with 180 cycles. The gate measurements cannot be compared in density. Before conducting the measurements, the 90 cycle HfO_x sample has changed after gating into the hysteresis. The intrinsic sample density - only about $n=0.5 \times 10^{11} \text{ cm}^{-2}$ smaller in the 180 cycle Hall bar - is determined directly after the cool-down (4.2 K) and presented in Table 2.1. The lower homogeneity of the thick insulator layer is also reflected in the magneto resistance measurements at different densities in Figure 2.4 (b). If compared to the thin 90 cycles insulator sample in Figure 2.4 (c), the evolution of n and p quantum Hall and SdH oscillation appears more distorted and irregular. Together with the lower gap resistance of the thin HfO_x and the slightly decreased intrinsic density [$n(V_g=0 \text{ V})$] of the thick HfO_x Hall bar, the qualitative comparison leads to the conclusion that the 180 cycles of insulator introduce potential disturbances into the system.

The calculation of the permittivity ϵ_r of the compared insulator systems supports this conclusion. The gate action $G_a = dn/dU$, the charge Q on a capacitor C of the area A and the voltage

$$U = \frac{Q}{C} = \frac{Q}{A\epsilon_0} \sum \frac{t_i}{\epsilon_{r,i}} = \frac{en}{\epsilon_0} \left(\frac{t_{Iso}}{\epsilon_{r,Iso}} + \frac{t_{(Cd,Hg)Te}}{\epsilon_{r,(Cd,Hg)Te}} \right)$$

help to determine

$$\epsilon_{r,Iso} = t_{Iso} \cdot \left(\frac{\epsilon_0}{eG_a} - \frac{t_{(Cd,Hg)Te}}{\epsilon_{r,(Cd,Hg)Te}} \right)^{-1},$$

the permittivity of the insulator. The model assumes two insulating layers of the thickness t and a homogeneous ϵ_r of the (Cd,Hg)Te cap ($t_{(Cd,Hg)Te} = 66$ nm) and the insulator (t_{Iso}) in between the conductive 2DEG and the gate electrode [43]. With an error of only ± 1 on the presumed $\epsilon_{(Cd,Hg)Te} = 12.7$ of the cap layer and the vacuum permittivity ϵ_0 , the resulting $\epsilon_{r,SiO_2-Si_3N_4}$, $\epsilon_{r,HfO_2,180}$ and $\epsilon_{r,HfO_2,90}$ in Table 2.1 do not allow for a quantitative interpretation. The thinner the layer, the less accurate the outcome and the bigger the error bars of ϵ_r . However, with the layer stack non-different except for the insulator systems, the values can be compared within each other. Once more, the lower permittivity of the 180 cycles HfO_x on both the $(200 \times 600) \mu\text{m}^2$ (macro) and the $(10 \times 30) \mu\text{m}^2$ Hall bar (meso) confirm the thickness-dependent crystallinity of the ALD insulator.

The hysteresis-free voltage and density range of the gate electrode determines the available density range for reproducible measurements. As the potential difference increases with higher gate voltages, trap states in between gate electrode and 2DEG can

	SiO ₂ -Si ₃ N ₄		HfO _x 180		HfO _x 90	
	bHB	sHB	bHB	sHB	bHB	sHB
G _a [$\cdot 10^{11} \text{ cm}^{-1} \text{ V}^{-1}$]	1.92	2.1	5.80	5.72	7.64	7.68
ϵ_r	4.7 ^{+0.1} _{-0.1}	5.2 ^{+0.1} _{-0.1}	6.9 ^{+0.8} _{-0.6}	6.7 ^{+0.7} _{-0.5}	7.5 ^{+2.1} _{-1.2}	7.7 ^{+2.1} _{-1.2}
n(0 V) [$\cdot 10^{11} \text{ cm}^{-2}$]	3.54	3.50	2.96	3.14	3.65	3.65
$\mu(0 \text{ V})$ [$\cdot 10^3 \text{ Vs/cm}^2$]	82	55	50	43	51	31
Hyster. free ΔV_g [V]	± 3.0	± 3.0	± 1.2	± 0.8	± 0.7	± 0.7
Hyster. free Δn [cm^{-2}]	13.8	11.8	14.5	8.6	12.4	11.5

Table 2.1: Sample parameters of Hall bars on wafer QC0063 with SiO₂-Si₃N₄, 180 HfO_x and 90 ALD cycles HfO_x as gate insulator extracted from the measurements.

be charged. As a third charge layer in the capacitor model, they screen the 2DEG from the gate potential. Only discharged if the potential, i.e. the gate voltage, is reversed, the density is shifted in respect to the applied gate voltage and the initial potential landscape is modified [43, 47].

The hysteresis-free voltage range in the HfO_x samples is much smaller, but thinner layers and a higher relative permittivity result in a higher gate action. However, with an average hysteresis free Δn of $12 \times 10^{11} \text{ cm}^{-2}$, one cannot determine a significantly higher density range in the ALD insulators. This indicates that the limiting trap states are most likely at the (Cd,Hg)Te insulator interface and less likely within the insulator system [43].

With the novel HfO_x ALD layer, an alternative insulator system is introduced. The layer-by-layer growth at 34°C creates a homogeneous layer thickness and allows the use

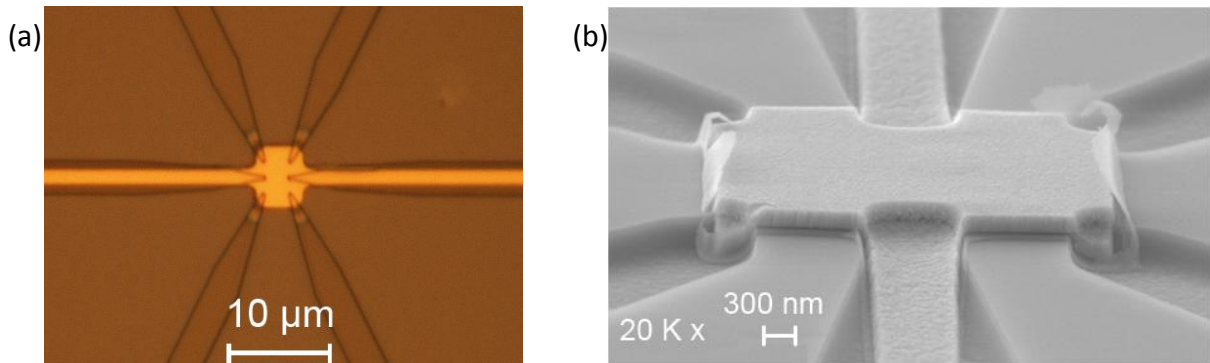


Figure 2.5: **a)** Micrograph of a wet etched micro Hall bar with an optically defined HfO_x gate. **b)** SEM image of a wet etched micro Hall bar with an EBL defined HfO_x gate.

of resist processes. The self-aligned lift-off method excludes the use of HF for the SiO_2 - Si_3N_4 removal and avoids the contamination of the insulator-metal interface by saving the additional gate lift-off process on its surface. Measurements on macro and mesoscopic Hall bars prove the insulator system to be suitable for device fabrication.

On structures with lower dimensions two possibilities are developed to apply a self-aligned gate electrodes. First, in optical resist lift-off processes with an accuracy of about $1\ \mu\text{m}$ [see Fig. 2.5 (a)]. Second, the very same self-aligned ALD insulator growth and gate metalization can be applied with double layer PMMA lift-off resist [described on page 72]. The e-beam exposure allows for a dimension control of 10 nm accuracy. The more sensitive bottom layer PMMA results in an undercut after development. Similar to the self-aligned process with the optical negative resist, the HfO_x grows into the undercut and is subsequently metalized. Figure 2.5 (b) shows the SEM image of a wet etched micro Hall bar with a self-aligned EBL gate electrode after the acetone lift-off. The insulator, only 50 nm larger than the electrode, also enables processing of several gates in proximity to each other and designs only limited by the EBL resolution.

The mesas of both Hall bars in Figure 2.5 are defined using a novel etch technique for micro structure fabrication. Together with the optimization of the optical lithography processes in chapter *Hall Bar Process* on page 16 and the novel low temperature ALD insulator in this chapter, the novel wet etch process is a major contribution to high quality micro structures.

Wet Etch Process

A novel wet etch fabrication for microscopic structures of superior quality is established within this work. Starting with a comparison to the previous ion milling process (dry), its particularities, advantages and results are presented along the chronology of the lithographic development and measurement feedback. Further optimization, such as the ALD insulator, the voltage probing contacts and interface cleanness, can be followed sample by sample through the constant adaptation of the fabrication design and technique. At the end, a tool box for micro structure preparation is given in form of the resulting processes for a micro Hall bar.

A comparison of the wet and dry etch process for the sample fabrication motivates the necessity of the novel etch technique. Whereas the quality of samples produced with ion milling decreases with the sample size, the qualitative performance of the wet etched structures is not dependent on the examined dimensions. In order to compare the device quality quantitatively, electrical transport measurements are carried out in macroscopic ($(200 \times 600) \mu\text{m}^2$), mesoscopic ($(10 \times 30) \mu\text{m}^2$) and microscopic Hall bars (sub $10 \mu\text{m}$), fabricated by the two methods and on one wafer of a (Cd,Hg)Te/HgTe/(Cd,Hg)Te QW with 7.5 nm HgTe. The advantages of the wet etch process are presented in Figure 3.1 along the standard Hall and magneto resistance measurements **(a)** and **(b)** and the electron mobility μ as a function of electron density and size **(c)** and **(d)**. All experiments are conducted at a temperature of 4.2 K.

Figure 3.1 shows the longitudinal and transverse (Hall) resistance for a wet **(a)** and dry etched micro Hall bar **(b)**. For comparable carrier density of $n = 6.5 \times 10^{11} \text{cm}^{-2}$ the mobility in the wet etched micro Hall bar (extracted from R_{xx} at $B=0 \text{T}$) reaches $\mu = 295 \times 10^3 \text{cm}^2/\text{Vs}$, a value about seven times higher than the one for the dry etched sample. As the magnetic field increases, Shubnikov-de Haas oscillations (SdH) become visible in R_{xx} (black) and quantum Hall plateaus form in R_{xy} (red). In the wet etched sample they are clearly distinguishable above 1 T [see Fig. 3.1 **(a)**]. Zero resistance states in R_{xx} are observed for magnetic fields higher than 2.7 T where the bulk becomes truly insulating.

Hall plateaus and SdH oscillations are also visible in the dry etched micro Hall bar [see Fig. 3.1 **(b)**]. However, they indicate strong disorder and appear above 2 T. At the plateau-to-plateau transitions in between 4 T and 7 T the Hall resistance (red) shows clear overshoots.

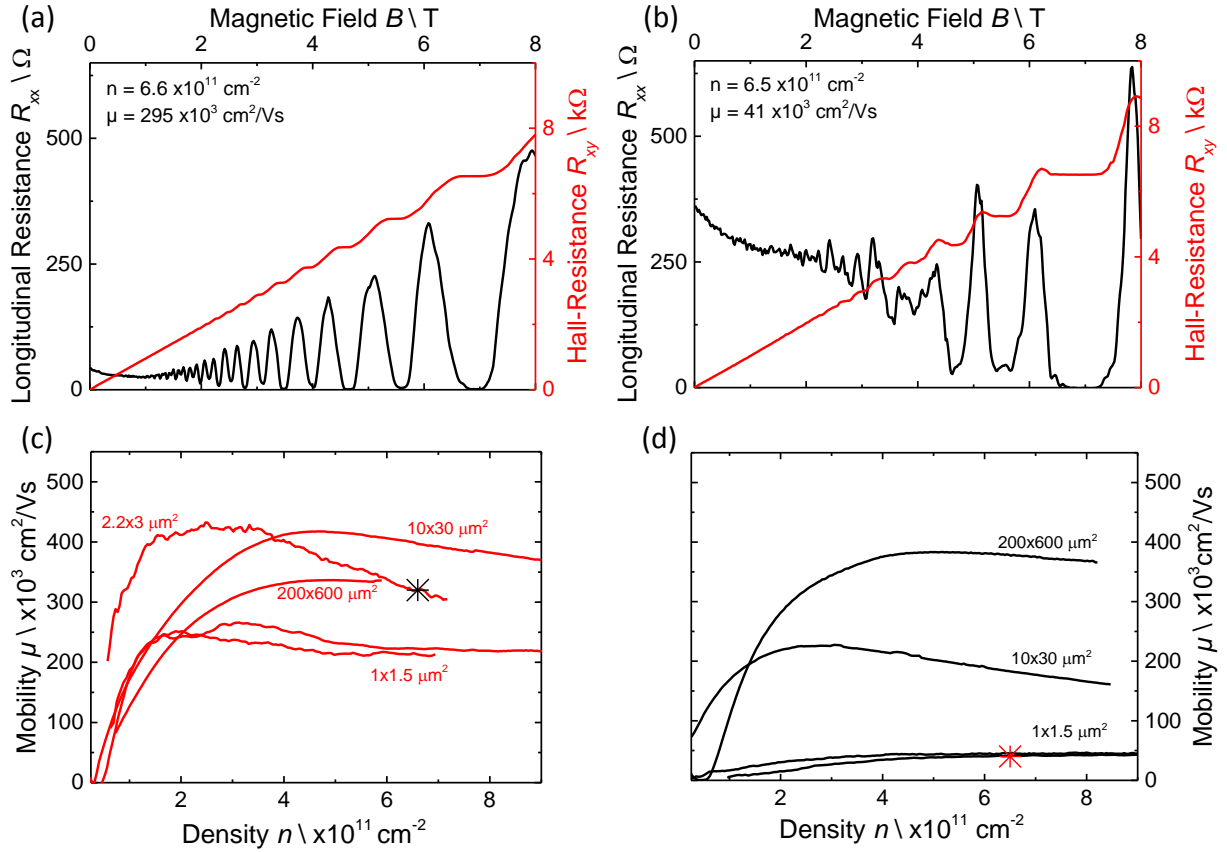


Figure 3.1: Longitudinal (black) and Hall resistance (red) plotted against magnetic field measured in **(a)** a $(2.2 \times 3) \mu\text{m}^2$ wet etched and **(b)** a $(1 \times 1.5) \mu\text{m}^2$ dry etched micro Hall bar. Mobility plotted versus the density of **(c)** wet (red) and **(d)** dry etched Hall bars of different sizes (black). For comparison all samples are build of the same wafer QC0258.

An increase of resistance above the expected quantization. Zero resistance states in R_{xx} are measured at much higher magnetic fields around 7 T. These observations indicate inhomogeneities resulting in an affected potential landscape, distorted Landau levels and back-scattering. Other than that, the wet etched sample shows SdH oscillations at lower magnetic field and has well pronounced Hall plateaus. The Landau levels appear less distorted, reflecting a lower amount of scatterers leading to a higher carrier mobility. From the Hall and longitudinal resistance the carrier mobility μ is determined as a function of gate voltage. Figures 3.1 **(c)** and **(d)** show the density dependent mobility of Hall bars of different sizes, due to wet and dry etching, respectively. For all devices the mobility increases as n increases, reaches a maximum and decreases again for higher carrier densities. The steam increase of mobility in low densities can be explained by the enhanced screening of scattering potentials (from Coulomb disorder) due to increased carrier concentration. The decrease in μ on further increasing n has been shown to occur due to band gap fluctuations in a Dirac system [49].

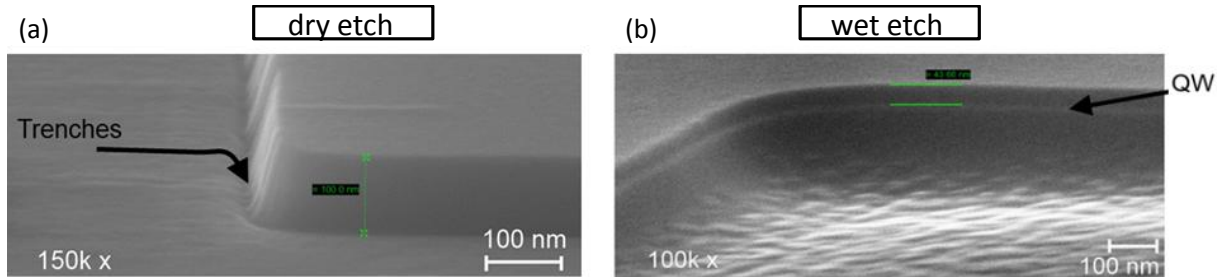


Figure 3.2: **(a)** SEM picture of a ion milled mesa after the hard mask removal. The mesa edge transitions show the common trenching, the etch depth is homogeneous. No material contrast is visible. **(b)** SEM picture of a wet etched mesa. The 7.5 nm HgTe QW is clearly visible as a bright layer. The rougher area of the sample has previously been PMMA-covered, exposed, developed and etched.

The most significant difference between the dry and wet etched samples is, that the mobility for the dry etched Hall bars scales inversely with the device size. The meso Hall bar shows a maximum mobility of only $228 \times 10^3 \text{ cm}^2/\text{Vs}$, a factor of about 1.6 lower than the macro Hall bar, while the mobilities in the two micro Hall bars are about eight times smaller (maximum at $\mu = 43 \times 10^3 \text{ cm}^2/\text{Vs}$ and $46 \times 10^3 \text{ cm}^2/\text{Vs}$)[see Fig. 3.1].

In the wet etched Hall bars, however, the mobility does not exhibit any systematic size dependence and ranges from 200 to $400 \times 10^3 \text{ cm}^2/\text{Vs}$. The $(1 \times 1.5) \mu\text{m}^2$ wet etched Hall bars, for example, host electron mobilities about six times higher than their dry etched counterparts of the same size. Even more striking, the $(2.2 \times 3) \mu\text{m}^2$ micro Hall bar reaches a maximum value of $432 \times 10^3 \text{ cm}^2/\text{Vs}$, higher than any of the other samples. This corresponds to a mean free path of the electrons of $\lambda_{mfp} = 5 \mu\text{m}$, larger than the actual sample dimensions.

Aware of the tremendous influence of size on the performance on dry but not on wet etched Hall bars, let us first search for obvious reasons in the SEM images of the etched mesas and then look into the details of the dry and wet etching process.

Figure 3.2 **(b)** shows a SEM picture of a wet etched micro Hall bar. The mesa edges are smooth, the material contrast is good and the QW is clearly visible as a white horizontal line. As the etching is limited by the diffusion of the etchant in the aqueous solution, the typical profile of the mesa shows wide trenches, visible in Figure 3.2 **(b)**. Their width ranges from a few hundred nanometers to a few microns depending on the mesa design and the etch depth [48]. The sharp mesa edges and the exposed QW are first indications for the non-destructive method. The roughness in the etched area is a result of the inhomogeneous etch start through the surface oxide.

Figure 3.2 **(a)** shows a SEM image of a dry etched mesa. Despite some advantages of the dry etching process, such as the reproducible and homogeneous etch depth, detrimental effects of this approach are clearly visible. First, redeposited material on the edges of the structure obscures the contrast of the QW and may disturb the potential landscape along

the edge. Second, a sharp trench profile is observed due to the ions reflected on the side of the mesa during ion milling.

The conventional dry etch method uses accelerated Ar^+ -ions to physically sputter material. Ion milling is carried out for about three minutes in a home-built vacuum chamber at a base pressure of 1×10^{-9} mbar. It is equipped with a GEN2 ion gun which is operated at 1 kV ion energy and a total ion current of 8 mA. A dry mask is fabricated in a four step process to protect the Hall bar structure. It consists of a 10 nm SiO_2 sacrificial layer and 15 nm Ti and its fabrication method is schematically displayed in Figure 3.3 (a):

I. Plasma-enhanced chemical vapour deposition (PECVD) covers the surface with 10 nm SiO_2 .

II. A Ti mask is patterned onto the SiO_2 film using lift-off technique. The smaller areas are patterned using a Polymethylacrylat (PMMA) EBL 2.5 kV lift-off process.

III. The contact leads are metalized in an additional lift-off process using optical lithography.

IV. A plasma of CHF_3 (RIE) etches the uncovered SiO_2 away.

V. The structure is subsequently ion milled and material is physically sputtered by the Ar^+ -ions accelerated onto the surface [50]. The protective hard mask can then be dissolved in hydrofluoric acid ($\text{HF}:\text{H}_2\text{O}$ 1:20) revealing the mesa [see Fig. 3.3 (b)].

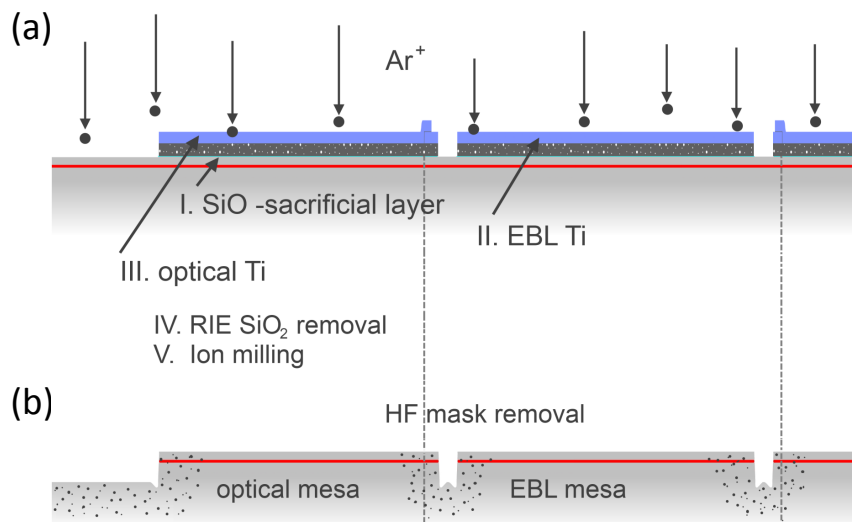


Figure 3.3: Schematic of the dry etch mask processes. (a) I. The PECVD grown SiO_2 sacrificial layer covers the sample. II. and III. 15 nm of Ti are deposited with an electron beam lithography (EBL) and optical lift-off process. IV. uncovered insulator is etched using RIE. V. Ar^+ -milling is used to etch the QW. VI. an HF dip solves the dry etch mask. (b) Ar^+ -milled mesa. The black dots indicate the damage introduced by the ion milling.

The quality in dry etched microstructures is damaged through the insulator on its surface, multiple lift-off processes – each requiring resist bake-out – and the SiO₂-Ti mask removal with HF. Numerous publications, furthermore, refer to the doping of (Cd,Hg)Te by ion milling [51, 52, 53, 54]. Etching p-type (Cd,Hg)Te with accelerated ions leads to a p to n-conversion [55]. From 1 μm within the first 10 s to over 100 μm deep within minutes, the (Cd,Hg)Te is reported to be doped due to Hg inter-diffusion.

Our (Cd,Hg)Te/HgTe/(Cd,Hg)Te QW structures are intensively exposed to ion milling. However, no effective increase in the electron density of the QW is measured. But, if pure (Cd,Hg)Te exposed to ion milling, a current flows at 4.2 K when voltages higher than about +1 V or -4 V are applied. No parallel conductance is expected with a small excitation voltage lower than 10 mV. However, the unintended doping of the (Cd,Hg)Te barrier layers comes along with impurities that disturb the potential landscape and can introduce backscattering of charges in the QW. With decreasing size, more and more of the Hall bar is damaged by the nearby etching with lateral influence. The mobility is lowered and the SdH oscillations as well as the quantum Hall signal differ from the ideal picture.

Figure 3.4 (a) shows SdH oscillations of a macroscopic (black) and microscopic Hall bar (red) and their Hall resistance in (b). Whereas SdH as well as Hall follow the expected dependence on the 200 μm wide macro structure, the 2 μm wide micro structure exhibits an uneven potential landscape as the Landau levels transitions can neither be distinguished

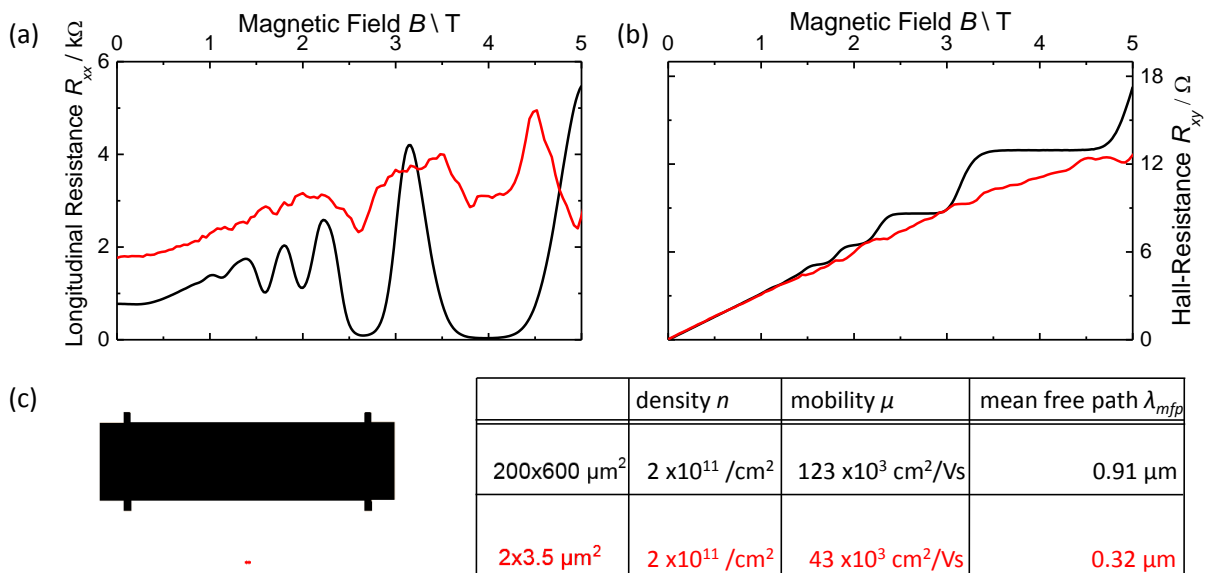


Figure 3.4: (a) Longitudinal and (b) Hall resistance of a (200 × 600) μm² macro (black) and (1 × 1.5) μm² micro Hall bar (red) fabricated via ion milling plotted against the magnetic field. (c) Schematic of the size difference opposed to a comparison of sample parameters withdrawn from the measurements.

in the SdH oscillations **(a)** nor in the quantum Hall **(b)**. Figure 3.4 **(c)** schematically displays the size difference of both samples. The damage along the side and the increased edge to volume ratio explains the, by a factor of 2.8, smaller mobility $\mu = 43 \times 10^3 \text{ cm}^2/\text{Vs}$ and mean free path $\lambda_{mfp} = 0.32 \mu\text{m}$ of the micro Hall bar [see tabular in Fig. 3.4 **(c)**].

The wet etch method relies on chemical and not physical etching. The used aqueous solution of $\text{KI} : \text{I}_2 : \text{HBr}$ has first been reported on $(\text{Cd,Hg})\text{Te}$ by [56, 57]. The etch rate is highly affected by variables such as the oxidation potential of the sample, activation energy of reaction, viscosity of the etching solution, composition of etchant and temperature. The underlying chemistry process involves the redox reaction and therefore the exchange of charges between the sample surface and the etch solution. Electrons are being released after the oxidation of telluride (Te^{2-}) by triiodide (I_3^-) and consumed in the reduction of the metal ions (Hg^{2+} and Cd^{2+}). The metal ions are then chemically dissolved in Hydrobromic acid (HBr). The etch rate increases as the concentration of Iodine in the solution is raised. Replacing HBr with Hydrochloric acid results in a similar etch depth. This confirms that the Iodine is involved in the rate-determining step, whereas the role of acid is to form halide ions for the dissolution of metal ions and to avoid the formation of insoluble products [58].

The uncovered mesa is etched under a flow of etchant in the concentration of:

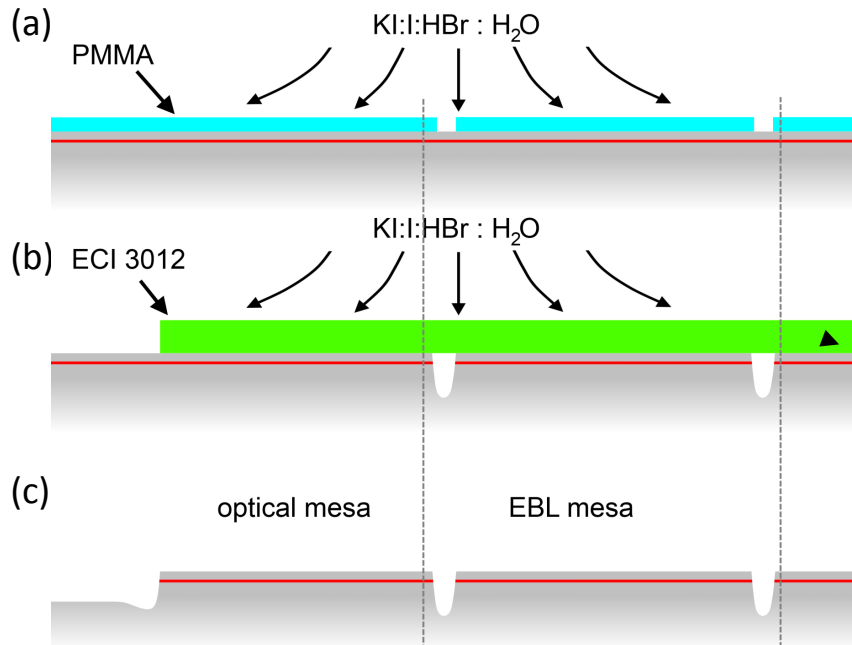
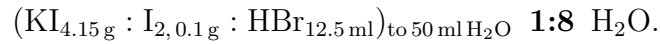


Figure 3.5: **(a)** EBL-PMMA wet etch mask and **(b)** optical wet etch mask both under a constant flow of etchant, acetone removal. **(c)** Wet etched mesa.

The mesa is thereby protected by a resist layer [see schematic in Fig. 3.5]. Commercially available resists are used as a soft etch mask. A UV sensitive photo resist can be used to define mesas in the resolution of optical lithography. For smaller mesa dimensions electron sensitive Polymethylmethacrylat (PMMA) and electron beam lithography (EBL) methods can be applied. Exposed and developed, only the uncovered areas of the wafer are etched during the process. Both resist masks are simply solved in acetone. Compared to the dry etch process, less lithography steps are required, the risk of surface contamination is reduced and the handling is simplified. A detailed list of parameters and a description of the lithographic processes can be found in *The Novel Micro Hall Bar Process* on page 69.

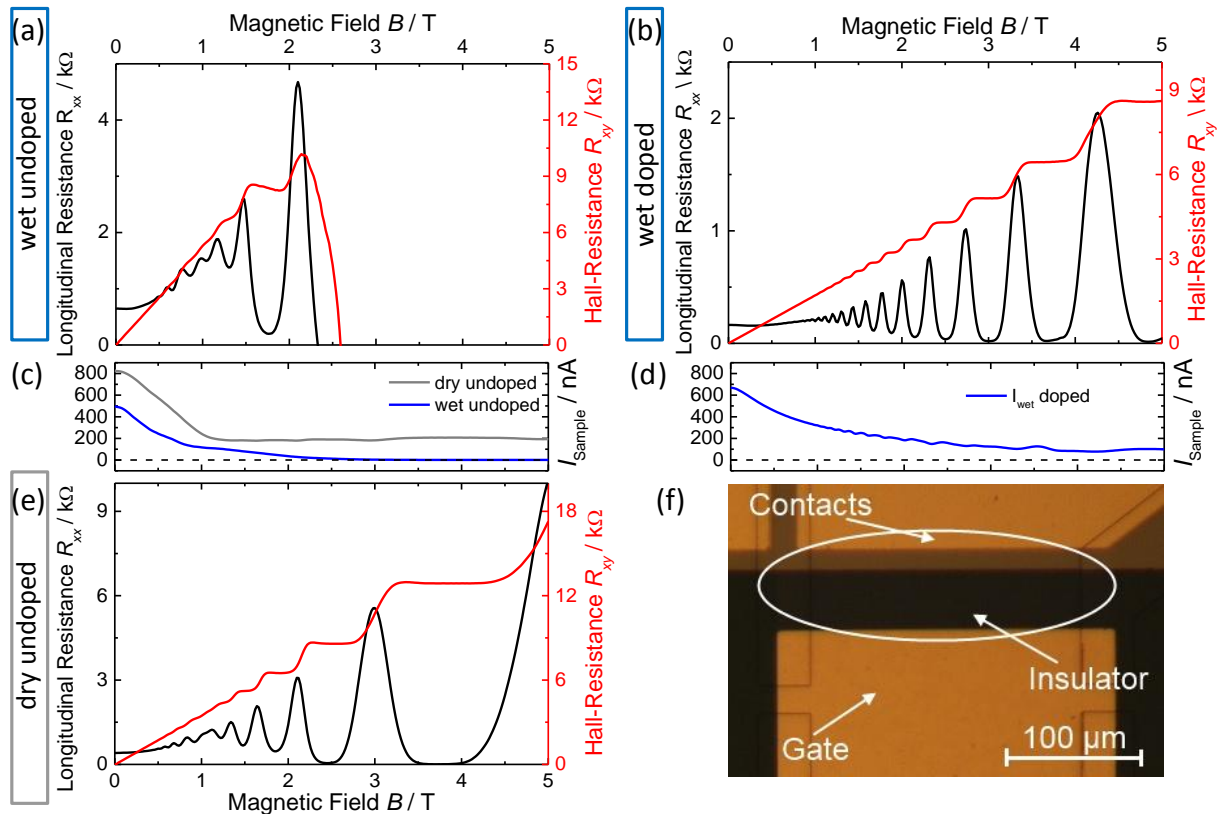


Figure 3.6: Longitudinal (black) and Hall resistance (red) of $(200 \times 600) \mu\text{m}^2$ macro Hall bars plotted against the magnetic field in (a) for a wet etched and undoped QW (Q2745), (b) a wet etched and doped QW (QC0287) and (e) a dry etched undoped QW (Q2745). (c) Sample current plotted against the magnetic field of the undoped dry (gray) and wet etched Hall bar (blue) (Q2745). (d) Sample current plotted against the magnetic field of the doped wet etched Hall bar (blue). (f) Micrograph of the area without gate in the contact leads to the Hall bar. Lower in density, it can lead to the current freeze-out in magnetic field if undoped and wet etched.

Macroscopic Hall bars fabricated with both dry and wet etch technique prove that the methods result in differing measurements. Let us first focus on wet etched structures for doped and undoped QWs.

Figure 3.6 (a) shows Hall (red) and longitudinal resistance measurements (black) of a undoped and (e) of a doped wet etched Hall bar. SdH and Hall break down above 2 T as the sample current freezes out in magnetic field [see current in Fig. 3.6 (c) (blue)]. The doped device shows no such behavior and a decreasing but finite sample current [see Fig. 3.6 (b) and (d)]. This behavior can be explained by considering the current leads to the Hall bar in Figure 3.6 (f). Encircled in white one finds an area which is neither covered by gate electrode between, nor ohmic contacts. From measurements on Hall bars with and without gate, it is known that the presence of the insulator gate system ($V_g=0$ V) increases the carrier density of the device underneath by about $\Delta n=1\times 10^{11}$ cm⁻². Thus, the intermediate area has in fact a lower carrier density than determined for the Hall bar with gate. In the undoped sample, this area reaches the insulating energy gap earlier than the actual Hall bar. No current is flowing above 2.5 T. The measured Hall and longitudinal voltages are normalized with a value close to zero and the resistances go towards infinity. In the Hall bar with a doped QW, the overall carrier density is increased. Even though lower in the intermediate area without gate, the carrier density is high enough not to reach the insulating regime of the energy gap up to 5 T.

If a Hall bar of the very same undoped wafer is fabricated using the conventional dry etch process, its magneto resistance measurements do not exhibit such a current freeze-out [see Fig. 3.6 (e)]. Above 1 T, the sample current (gray) plotted in Figure 3.6 (c) saturates at about 200 nA. Despite the lower density and the area without gate being in the gap, the contact leads to the dry etched Hall bar are never fully insulating at higher magnetic fields. Solely different in the mesa etch method, it can be concluded, that the ion milling introduces an unintended conductance. Hence, the current freeze-out of the wet etched Hall bar of the undoped QW is once more a signature of the superior novel etch process.

The microscopic Hall bar fabrication progress is depicted on the following pages. First, the particularities of the wet etch technique for mesa fabrication can be understood by perusing the process adjustments in concentration, application method and mask design in *The Wet Etch Evolution*. Then, measurements on samples are presented in the chronology of the process adaptations in *The Sample Story*. And at the resulting stage of development is presented along a detailed fabrication process description in *The Novel Micro Hall Bar Process*. Including a thorough description of the lithography steps subsequent to the mesa etching, it can be seen as a tool box for micro structure preparation.

3.1 The Wet Etch Evolution

There are three main objectives in the development of the wet etch process for micro structures on (Cd,Hg)Te/HgTe/(Cd,Hg)Te QWs: a clear and proper etching without re-deposition or damage to the mesa, a mesa height that allows the use of the subsequent lithography and therefore the comparison to dry etched samples as well as reproducible process parameters.

The longer the etch time, the lower the error susceptibility introduced due to time insecurity in the handling by the user. Using KI : I₂ : HBr solved in ethylene glycol instead of water would increase the viscosity and thereby decrease the etch rate [see Fig. 3.7 (a)] [57]. However, the resist mask solves itself whilst immersed in ethylene glycol, resulting in rounded edges along the mesa. The smooth edge potential can break the time-reversal symmetry and enhance back-scattering in the QSH edge channels [59]. With the QSHE being the center of interest, sharp edges are required. To achieve reasonable etch times despite the dilution in water, the ratio of KI to I₂ can be lowered [see Fig.3.7 (b)].

At first, it is ascertained that solely placing the sample in the etchant barely etches a few

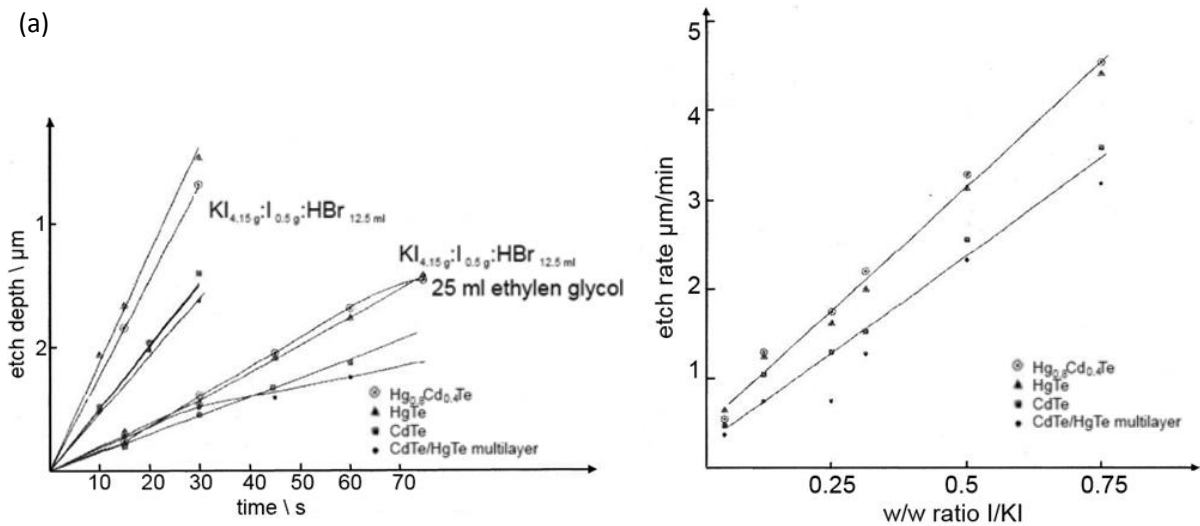


Figure 3.7: (a) KI : I₂ : HBr etch depth plotted against the etch time for (Cd,Hg)Te, CdTe and HgTe dissolved in water (higher etch rate) and ethylene glycol (lower etch rate). (b) etch rate for (Cd,Hg)Te, CdTe and HgTe plotted against the I/KI ratio. Lowering the iodine concentration lowers the etch rate. Taken from [57].

nm deep, regardless of the etch time. The etching saturates if not intermixed. A rotating sample holder is realized by fixing a magnetic stirring bar beneath a Teflon stamp on which the prepared sample is placed in the etchant and put on a magnetic stirrer [see inlay in Fig. 3.8]. The sample rotates in the liquid and its surface is constantly supplied with fresh solution.

Figure 3.8 shows the etch result of three etch tests with adopted etch time and iodine concentration. As for all processes the wafers have previously been spin-coated with PMMA, exposed with EBL and developed in isopropanol. The soft etch mask then only covers the subsequent Hall bar structure and its contact leads within the EBL write field. The formerly exposed and developed areas are then etched in the solvent. The SEM images are taken after stripping off the etch mask in Acetone. Figure 3.8 (a) shows the SEM image of an etched mesa after 60 s of etching with an iodine amount of 0.5 g in the solution diluted 1:4 in H₂O. A plateau-like structure can be distinguished in Hall bar shape that is under-etched by a profile, expected for an isotropic etch behavior. The surface, the 50 nm thick (Cd,Hg)Te capping layer, the HgTe QW and the (Cd,Hg)Te/CdTe buffer beneath the conductive QW in the bulk are etched differently. This results in an overhang of the least etched material around the QW. With about 700 nm mesa height, the subsequent lithography steps such as contacting the QW from above and the gate insulator application would require severe adaptations.

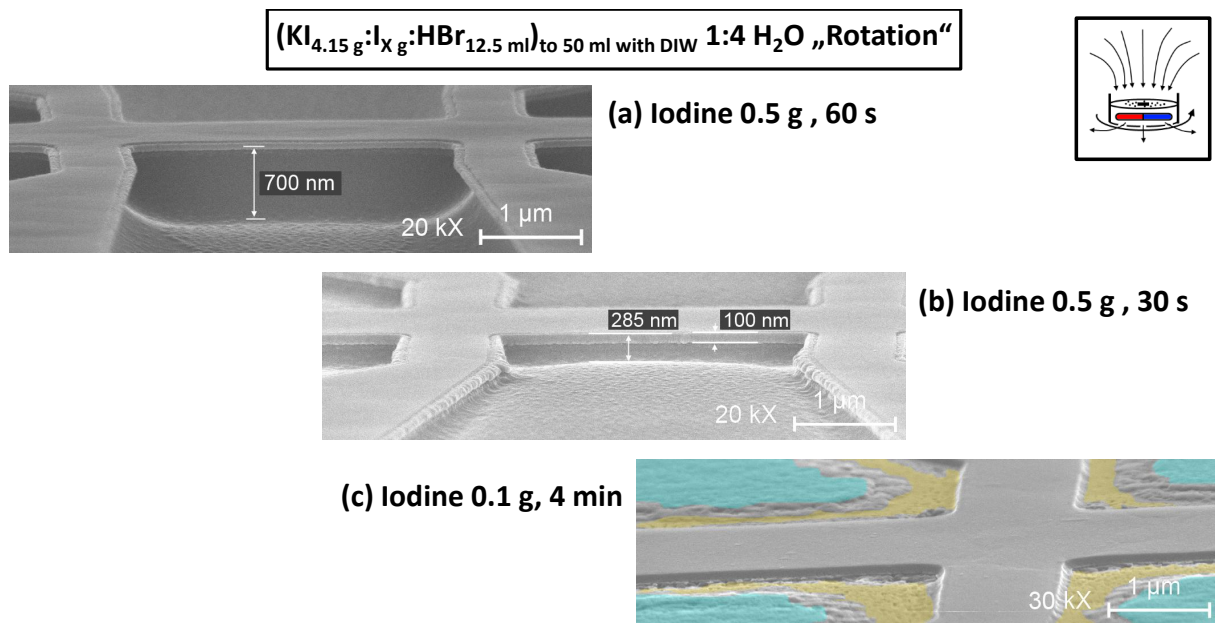


Figure 3.8: Mesas fabricated using the wet etch rotation method with varying etch time and iodine concentration. The elevated and flat part has been protected with a soft etch mask, the wafer etched and the mask removed in acetone. The method results in an overhang of the top layers. (a) 0.5 g iodine for 60 s. (b) 0.5 g iodine for 30 s. (c) 0.1 g for 4 min. The surface oxide interface (light blue) and the HgTe QW surface (yellow) are highlighted artificially.

A lower mesa height is achieved by reducing the etch time to 30 s at similar iodine concentration [see Fig. 3.8 (b)]. While the overhang shows the same characteristics, the etch depth is determined to about 285 nm.

Lowering the iodine amount to 0.1 g reduces the etch depth, even though the etch time is increased to 4 min. Figure 3.8 (c) exhibits some particularities. Two limiting interfaces can be determined. The initial (Cd,Hg)Te surface, flat but interspersed with etched irregularities as visible in the corners of the image (light blue), and the HgTe QW layer 50 nm below the surface (yellow), closer to the initial soft etch mask. Furthermore, the QW as well as the (Cd,Hg)Te cap are both etched deeper along the edge of the mask.

The (Cd,Hg)Te wafer surface as well as the HgTe QW interface are both less etched than the (Cd,Hg)Te/CdTe below the conductive HgTe QW. The nonlinearity in the etch rate proves that the top layers are etched slower than the bulk. As discussed on page 41 below, this is related to the conductivity of the QW, not the etch rate of the pure

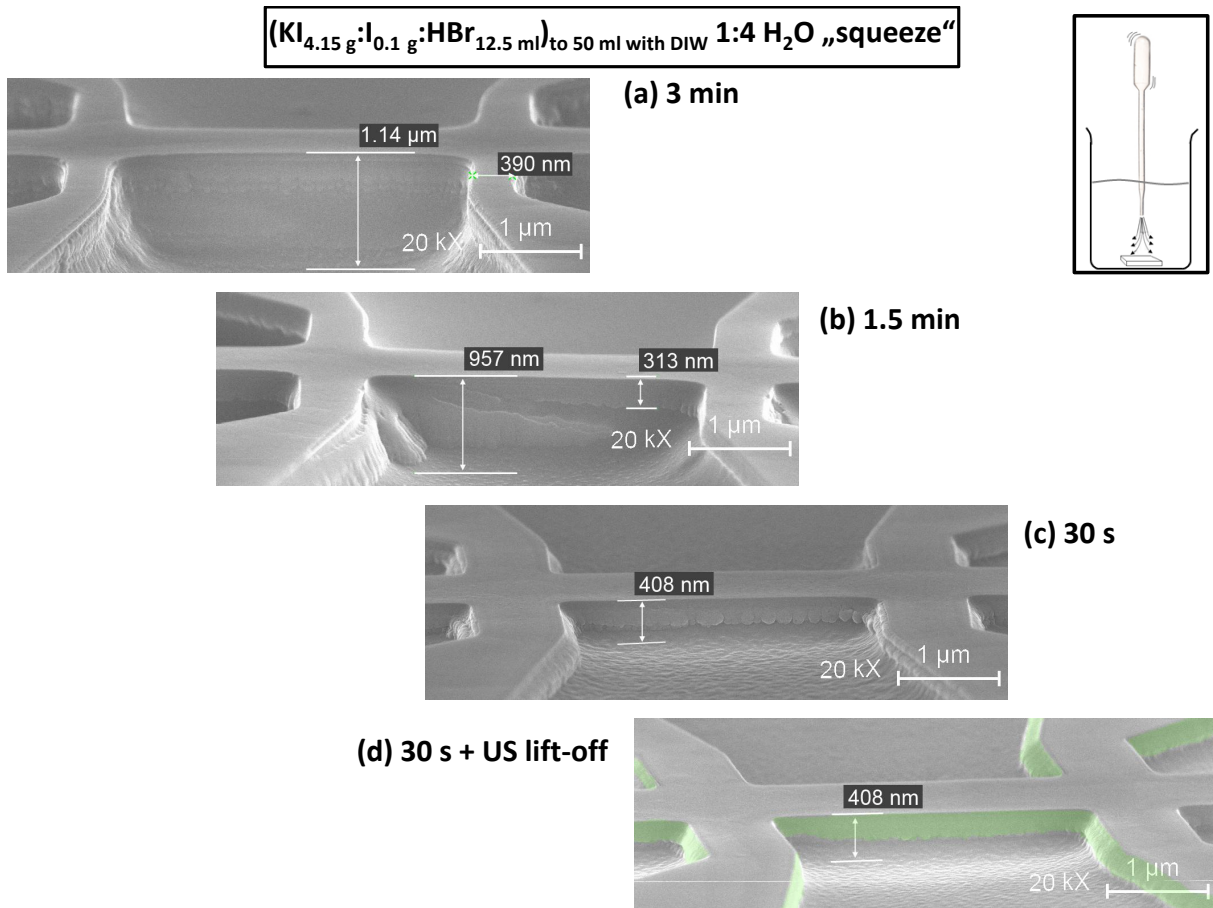


Figure 3.9: Mesas fabricated with the wet etch "squeeze" method with varying etch time. The elevated and flat part has been protected with a soft etch mask, the wafer etched and the mask removed in acetone. The previous overhang is now folded down. (a) 3 min (b) 1.5 min (c) 30 s and (d) 30 s, the soft mask removal in acetone has been supported with an ultrasonic bath.

material. Thus, in no contradiction to the results in [56], where a similar etch depth in time is reported for pure (Cd,Hg)Te and HgTe [see Fig. 3.7 (a)].

Three main conclusions can be withdrawn from this test. First, the QW and (Cd,Hg)Te cap layer are less etched than the (Cd,Hg)Te and CdTe buffer. Second, this results in an overhang of the least etched top layers. Third, the etching is most effective along the edges of the PMMA etch mask.

As the intermixing of the solution seems crucial to the resulting etch profile, a "squeeze" method is used to provide certain flow. The sample is thereby placed in etchant with a simple manual pipette directly above. Squeezing the pipette by hand then pushes and pulls fresh solution onto the wafer. Figure 3.9 shows the SEM images of the resulting mesa structures:

(a). Despite the same iodine concentration of 0.1 g and an etch time reduced to 3 min, the "squeezing" etches much more efficiently than the "rotation" method [see Fig.3.8 (a)]. Beside the higher mesa of about 1.4 μm , its shape is different with respect to the overhang in the results obtained using "rotation" in Figure 3.8. Redeeposited material can be found along the uneven rims of the mesa.

(b). With a reduced etch time of 1.5 min, the mesa height is determined to about 950 nm. It seems as if a previous overhang is folded down into the etched area, even ripped off and deposited in the trench at some rims.

(c) and (d). Further reducing the etch time to 30 s reinforces the conjecture of the bend down overhang, highlighted with light green in (d). Even if the mask removal in acetone is supported by ultrasonic bath (d), the unetched and folded top layer is not removed. The mesa height of approximately 400 nm however, is closer to the 300 nm limit, which would allow the application of the subsequent lithography steps without fundamental changes in the processes.

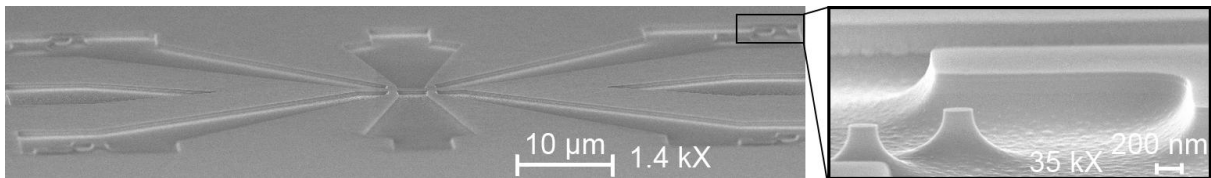


Figure 3.10: SEM image of a mesa fabricated with the "squeeze" method. The Hall bar mesa is connected to the QW and wafer outside of the write field, whereas the holes are etched (left). Zoom into the free standing alignment mark mesas. The folded overlap of the large interconnected mesa is visible in the background. Only the free standing mesas exhibit sharp transitions and smooth rims (right).

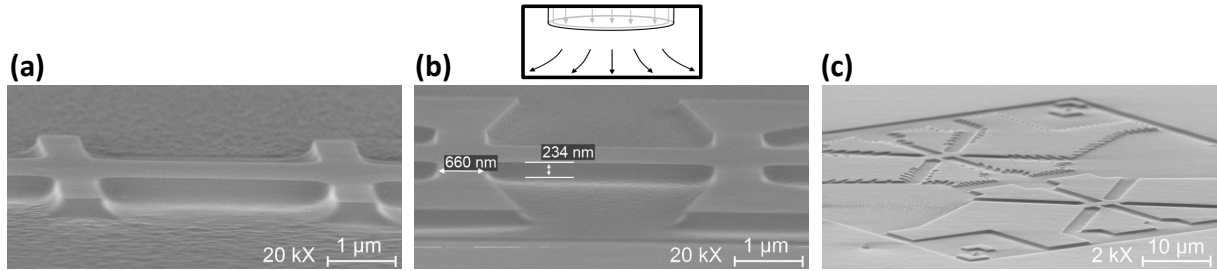


Figure 3.11: SEM image of Hall bar mesas, fabricated as free standing structures in small (a), intermediate (b) and write field size (c). The mesa height can be determined to slightly above 200 nm reproducibly achieved with the ‘pump’ technique.

Local alignment marks were added to some of the structures in the EBL design. They are used to align the write field of subsequent exposures accurately on top of the mesa. As free standing structures, they appear to be etched differently. Figure 3.10 shows the SEM image of a mesa in the whole 80 μm write field on the left and a zoomed image onto the free standing structures of an alignment mark on the right. Other than mesa, which is connected to the outside wafer, the free standing structures are properly etched. The HgTe QW, the top and bottom (Cd,Hg)Te material and the CdTe buffer are exposed and not covered with redeposition. A sharp transition from the mesa to the etched area can be noticed [see Fig. 3.10].

Figure 3.11 demonstrates that the concept of free standing mesa can be transferred to even bigger structures. Even if the mesa is increased from (a) small, to (b) medium and to (c) write field size, the transition is sharp and the mesa rims prove to be smooth. Because of the human factor in the “squeeze” technique with the manual pipette, the actual etch depth in earlier mesas varied from time to time and user to user. Therefore, a novel “pump” technique is already introduced into their fabrication. With the tube opening ending only 1 mm above the sample piece and a tube pump supplying a continuous flow of etchant, the flow speed is constant and reproducible. Thus, the mesa height can be adopted more accurately with process time.

Figure 3.12 shows three different stages of the etch result at increasing process time.

(a) At the start of the etching, after 10 to 20 s, the wafer in proximity to the PMMA soft etch mask is etched through first. Along weak spots in the (Cd,Hg)Te surface oxide, the solvent isotropically etches its way through the (Cd,Hg)Te cap layer and the conductive QW. Once the etching has reached the (Cd,Hg)Te bottom layer, it proceeds faster.

(b) Around 20 to 25 s. The accelerated etching of the (Cd,Hg)Te and the CdTe buffer leaves a mountain like morphology in the middle and a smooth trenching along the sides.

(c) Over 25 s. The selective etch start at the surface oxide translates to a spotty surface in the etched area. Deeper at the edges, the trenching clearly identifies the diffusive regime of the etchant [48].

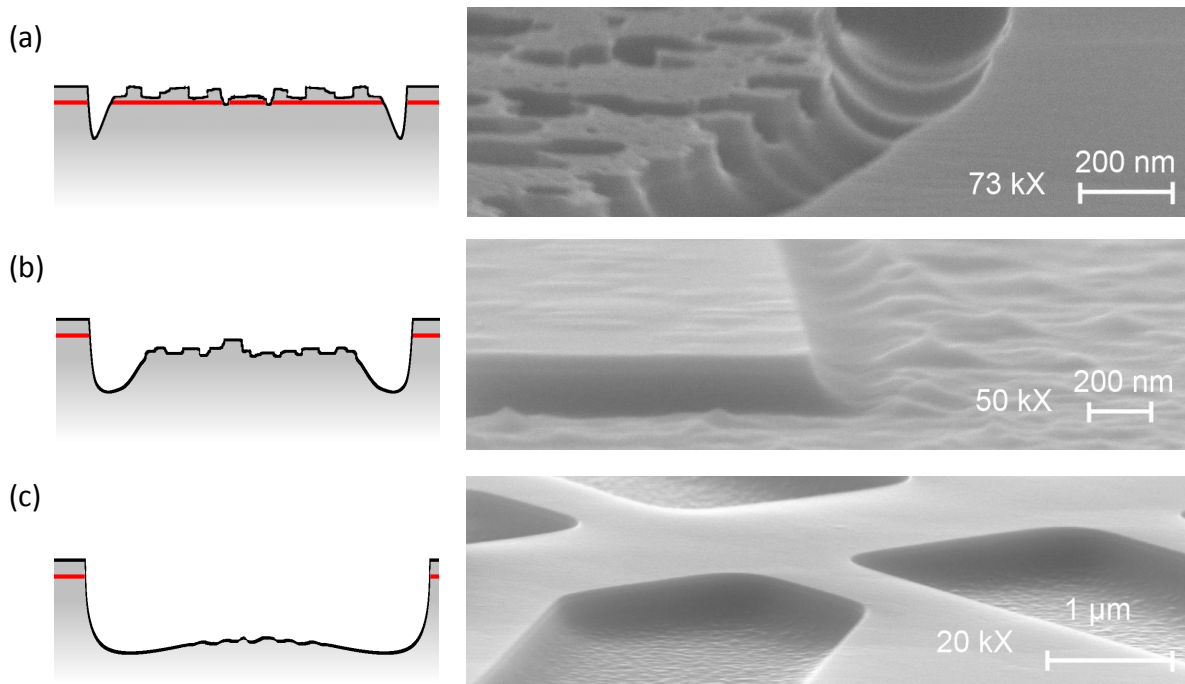


Figure 3.12: Three stages of etch result schematically displayed on the left and circumstantiated with SEM images on the right. **(a)** From 10 to 20s etch time. The flat and un-etched wafer surface on the right has been covered with the PMMA mask. The trenching effect of the diffusive regime results in the deepest etched trench along the mesa. The selectively penetrated surface oxide in the middle of the etched area is visible on the left side of the image. **(b)** Around 20 to 25s. The inhomogeneous etch start through the surface and QW translates to a mountain-like morphology in the etched part. **(c)** Over 25s. The etch profile shows a diffusive controlled regime. The Hall bar has a sharp mesa edge and smooth rims. The QW can be identified as a white line along the Hall bar (right).

Figure 3.13 **(a)** shows the calculated shape of an etched medium formed by the convection of a diffusion-controlled etch regime [48]. In full agreement to the profile achieved with the wet etch process, it explains why narrow structures are etched deeper. Figure 3.13 **(b)** schematically displays the consequence of narrow and wide mask designs, while the wide gap in the etch mask results in trenches along each side and an elevated part in the middle. The overlap of the trenches in the narrow gap of the etch mask yields a deeper etch profile.

The etch obstacle of the (Cd,Hg)Te surface oxide in the very first moments of the etching amplifies the trenching effect. The middle part of a to be etched surface is the least

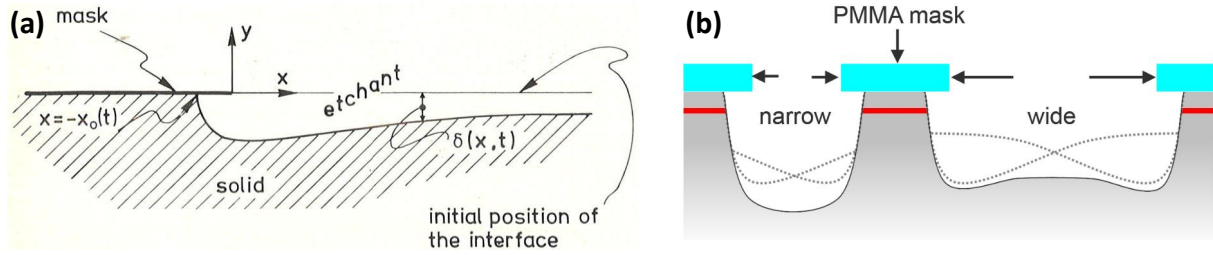


Figure 3.13: (a) Calculated etch profile in a diffusive controlled etch process [48]. (b) Schematic of the etch depth dependence of the width of the etched structure due to diffusive trenching.

penetrated and the bulk etching starts with a delay. A preliminary 50 s HF dip (HF:DIW 1:400) right before the wet etching removes the surface oxide and homogenizes the profile. Figure 3.14 (a) shows the etched part of a Hall bar mesa without oxide removal prior to the KI : I₂ : HBr. The mesa distance tapers from a wider to a narrower mesa distance. The mesa height in the narrow part is determined to about 195 nm, 40 nm deeper than in the wider mesa distance. Figure 3.14 (b) shows an etched mesa that has been pre-treated with HF. In the prior oxide removal the first etch obstacle in form of the surface oxide is removed. With about 200 nm the etch result is more homogeneous in wide and narrow structures. Uniform in the etched areas, it confirms the roughness in other samples to be translated from the inhomogeneous etch start trough the here removed surface insulator.

Throughout the development of the wet etch process the conductive QW has proven to be an etch barrier. This effect is distinct, if the mesa is connected to the QW outside of the write field and most noticeable in etch results interrupted in an early stage of the etching [see Fig. 3.8 (c) on page 37].

Even when the mesa is defined as a free standing structure, the lower etch rate of the conductive QW has consequences. Figure 3.15 (a) shows an SEM image of an alignment mark mesa. As in some but not all etch results, the QW is outstanding. With the same distance from mesa to mesa in the EBL design, the KI : I₂ : HBr solvent reaches the QW

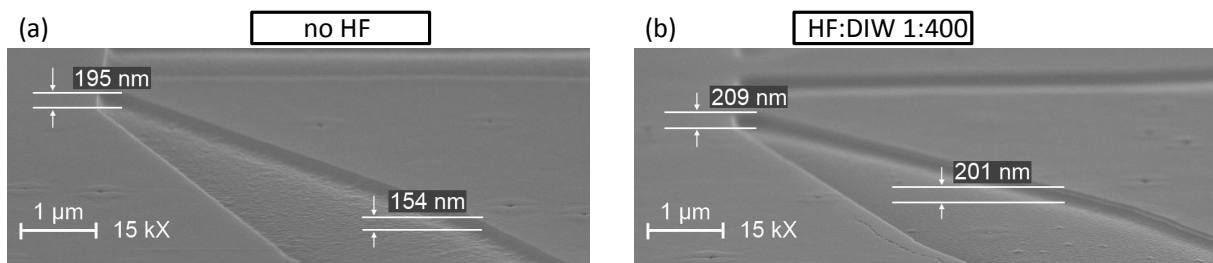


Figure 3.14: SEM images of the etch result with tapered mesa distance towards a Hall bar. Without (a) and with a HF surface oxide removal prior to the etching (b).

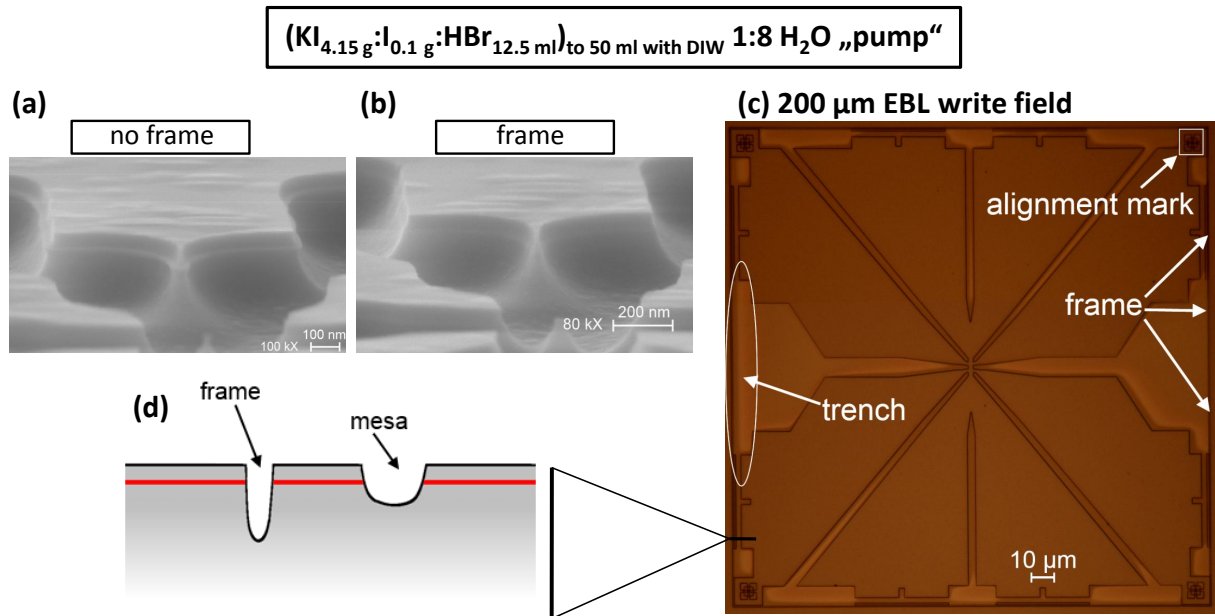


Figure 3.15: SEM image of the resulting alignment mark mesa and QW shape (a) without and (b) with a 300 nm wide frame around the write field. (c) Micrograph of an etched mesa in a 200 μm write field with all design adaptations. (d) Schematic cut through the deepest and first etched frame that electrically disconnects the inner write field.

everywhere in the write field at the same time. Selectively etched through the first layer in some spots, the underlying (Cd,Hg)Te etches faster and the overhang remains. The diffusive regime of the etchant helps to solve this problem with an only 300 nm wide frame defined around the write field. As the most narrow structure on the wafer, the frame is etched first and deepest. Therefore it electrically decouples the inner write field from the outer wafer [see Fig. 3.15 (d)]. In the redox reaction, the electrons available from the oxidation remain within the to be etched QW of the mesa, participate in the reduction and the (Cd,Hg)Te/HgTe QW is etched uniformly [see Fig. 3.15 (b)]. The QW is not outstanding, the rims are smooth and the mesa edges sharp.

Figure 3.15 (c) shows the micrograph of an etched Hall bar within a framed 200 μm EBL write field. The bright areas are etched, the contrast lines are mesa rims and the darker brown areas are mesa. The structure represents the actual stage of development and is used to summarize the wet etch evolution.

The EBL design is adopted to the specific requirements of the KI : I₂ : HBr wet etch process.

First, the mesa is disconnected from the outer wafer and QW. This avoids severe re-deposition along the mesa rims by the under-etched and folded down top (Cd,Hg)Te cap and HgTe QW layer.

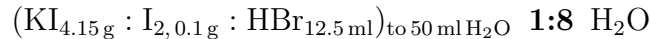
Second, due to the diffusive regime of the etchant, a 300 nm frame around the write field etches first and deepest. Small in its width, the frame electrically decouples the QW within the EBL write field, before the etching reaches the conductive layer in the wider etch mask designs surrounding the actual mesa. The possible appearance of an outstanding QW in the mesa can thus be excluded.

Third, two 200 μm write fields with one Hall bar each are processed instead of two Hall bars defined within the 80 μm EBL write field used in the conventional ion milling process. Consequently, the limited area for later contacting of the structure is increased, the contact leads can be defined symmetrically to each other and the optical lithography steps require smaller accuracy. Instead of 18 contacts on $(80 \times 80) \mu\text{m}^2$, 9 contacts can be placed generously on $(200 \times 200) \mu\text{m}^2$ [see Fig. 3.16 (a)].

Forth, the local alignment marks for the alignment of later EBL steps are adopted to the isotropic etch profile of the wet etch.

The pre-treatment in HF:DIW (50 s; 1:400) removes the natural oxide on the surface of the wafer, unprotected by the PMMA soft etch mask. This avoids the etch obstacle of the oxide and ensures a more homogeneous etch progression.

The "pump" method supplies the wafer with a constant flow of fresh KI : I₂ : HBr solution. Placed in etchant, with the ending of the tube 1 mm above the sample surface and an adjustable flow speed of the pump, a standardized etch environment is granted. 27 to 35 s in



reproducible result in a mesa height of 200 to 300 nm. As a consequence of the diffusive regime of the etchant, trenching is visible in Figure 3.15 (c). The slightly darker part along the mesa rims is etched deeper than the middle of the etched planes.

With this, all objectives are achieved. Clean wet etched micro mesas can reproducibly be fabricated with an etch depth below 300 nm. Only having focused on the mesa fabrication above, the measurement response of wet etched micro Hall bar devices throughout the development is shown on the following pages. Starting with the first free standing mesas, samples at different stages of development have been finalized with the subsequent lithography steps and measured. In *The Sample Story* they are presented along their chronology.

3.2 The Sample Story

Two type of measurements are used to judge on the quality of the micro Hall bar fabrication processes:

First, magnetic field dependence of the longitudinal and Hall resistance R_{xx} and R_{xy} in six terminal Hall configuration. The thereof calculated charge density and mobility can be compared to those obtained in macroscopic characterization Hall bars. Their SdH oscillations and Hall plateaus allow for a qualitative judgment on the homogeneity of the potential landscape.

Second, the gate sweep of the longitudinal resistance at zero magnetic field. R_{xx} is supposed to quantize at $h/2e^2 = 12.906 \text{ k}\Omega$ in the QSH regime due to the inverted band gap of HgTe QWs. Deviations from this value are related to backscattering of the QSH edge channels in the presence of density inhomogeneities and impurities. A detailed discussion about the QSHE is presented in *The Quantum Spin Hall Effect*.

On the following pages, characteristics of selected samples are presented along their lithography development and process adaptations. They are named after their substrate and numbered in order of their fabrication. All measurements have been conducted at 4.2 K. Samples in the early stage of progress might not provide the expected beautiful physics in all details. However, they motivate further investigations by QSH conductance close to quantization or non-affected mobility values. Furthermore, they allow to put the qualitative progress into context. Sample by sample, the disturbances are reduced and the physics is revealed. Changes in the individual sample layout are thereby displayed in micrographs of their EBL write field. Schematics of the sample design are given for a better overview and comparison. Single measurements are selected to accentuate the main statements on the sample performances.

Q2745 I. As the very first KI : I₂ : HBr-etched mesa measured, this sample is the proof of concept. The subsequent contact and gate lithography can be applied to the wet etched mesa. The contacts are working and measurements can be conducted.

Figure 3.16 (a) shows a micrograph and (b) a schematic of the first measured wet etched micro Hall bar. The two Hall bar mesas are disconnected from the outside wafer within the 80 μm EBL write field. Their ohmic contact area is indented to possibly improve the contact via the rims of the mesa. The metalized ohmic contacts reach 2 μm close to the initial Hall bar and beneath the integral SiO₂-Si₃N₄ insulator gate electrode.

Although the ohmic contact area in this design is two orders of magnitude smaller than

previously used in the ion milling fabrication, the sample exhibits comparable 3-point contact resistances of 1 to 5 k Ω . Contact size seems not to be the most dominant contact mechanism.

Figure 3.16 (c) shows the longitudinal (black) and Hall resistance (red) plotted against the magnetic field ($V_g = \text{gnd}$). The Hall plateaus are strongly disturbed and can only be anticipated. No SdH oscillations are visible. A factor of 2.4 smaller than in the characterization sample, the mobility of $\mu = 34 \times 10^3 \text{ cm}^2/\text{Vs}$ furthermore reflects the presence of scatterers.

However, the proof of concept and two measurement observations motivate further investigation:

With $n = 0.7 \times 10^{11} \text{ cm}^{-2}$, the carrier density at grounded gate is about the same as determined in the characterization measurement. Thus, the mesa is not doped while wet

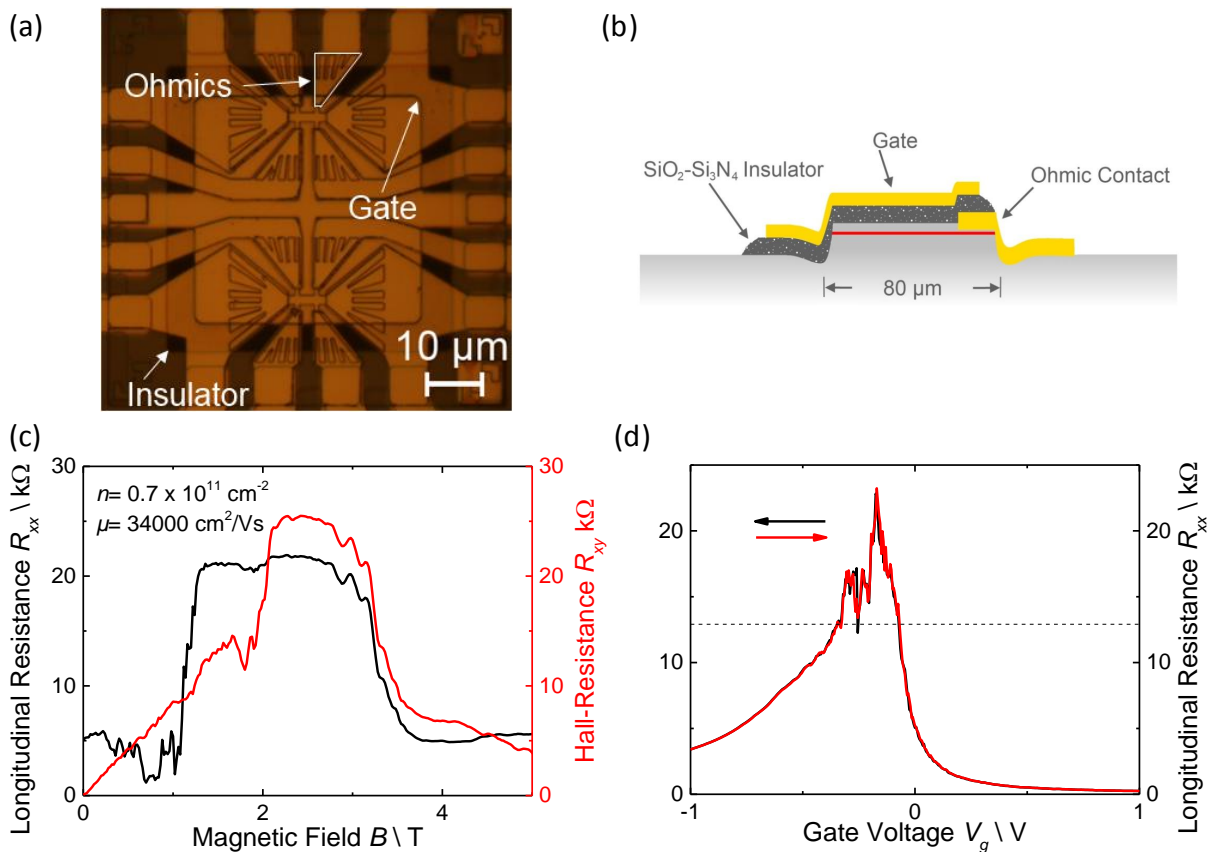


Figure 3.16: **Q2745 I.** (a) Micrograph and (b) schematic of the EBL write field. (c) Longitudinal (black) and Hall resistance (red) of the first measured wet etched micro Hall bar plotted against the magnetic field. (d) Longitudinal resistance R_{xx} plotted against the gate voltage. The dashed line marks the 12.9 k Ω expected for the resistance of two QSH edge channels in the gap.

etched.

The gate sweep in Figure 3.16 (d) shows strong fluctuations around $R_{xx} = 16 \text{ k}\Omega$ in the gap, between n and p -conducting regime below $V_g = -0.3 \text{ V}$ and above $V_g = 0 \text{ V}$. Other than insulating – as expected for a trivial semiconductor at 4.2 K – it is much closer to the conductance $2e^2/h$ of two QSH edge channels expected for a TI.

Q2745 III. The size of the mesas beneath the ohmic contacts is increased within the EBL write field of this sample. On one Hall bar, the mesa edges in the contact areas are straight, on the other they are indented. Other than that, nothing has been changed [see. Fig 3.17 (a)].

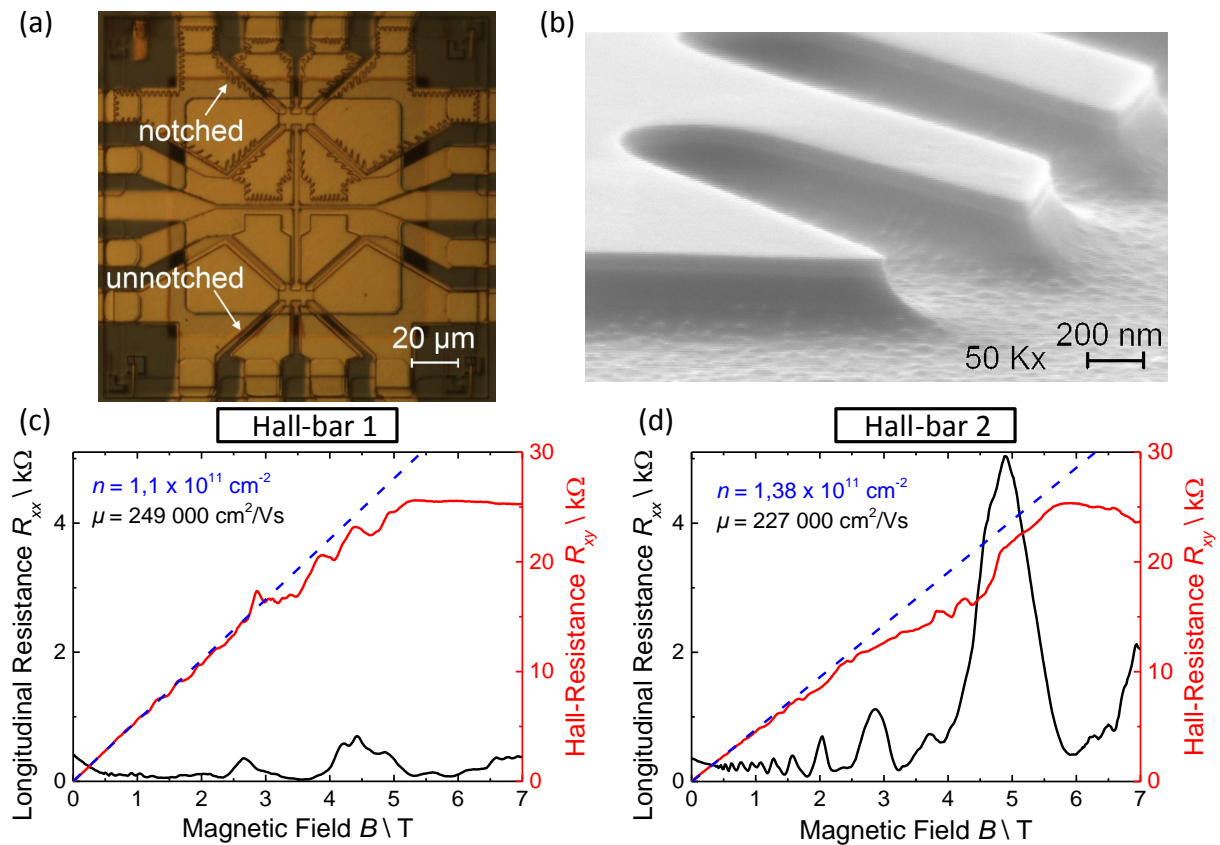


Figure 3.17: **Q2745 III.** (a) Micrograph of the EBL write field. The top has notched, the bottom Hall bar flat mesa edges. (b) SEM image of the notched mesa edge. The exposed HgTe QW can be distinguished in bright contrast along the mesa rims. (c) Longitudinal (black) and Hall resistance (red) plotted against the magnetic field for (c) the top and (d) the bottom Hall bar. The linear Hall is extrapolated in dashed blue.

The HgTe QW appears as a bright contrast line along the mesa rims in the SEM picture of the mesa in Figure 3.17 (b). The later applied AuGe contacts are in direct contact with the 2DEG. The interface is enlarged on the indented Hall bars and if the contact is provided along the mesa edge, there should be a difference. Yet, Hall bar 1 and 2 do exhibit the same 3-point contact resistances. Once more, they are found to stray from 1 to 5 k Ω . Thus, direct contact over the rim of the mesa is not the dominant mechanism.

No gate influence is measured if voltage is applied to the SiO₂-Si₃N₄ insulator gate electrode. Without electrical contact to the gate, the longitudinal (black) and Hall resistance measurements (red) plotted against the magnetic field in Figure 3.17 (c) and (d) are obtained with a floating gate. The Hall resistance in both Hall bars show indications of plateaus below magnetic fields of 2 T, but at the wrong resistance values. The higher field data bends down from the expected and extrapolated linear progression of the Hall voltage through the mid of the plateaus (dashed blue line). One sixth of the Hall bars around this early stage of the development show this peculiarity. No reason is found whatsoever. Other than in Q2745 I on the page 47, SdH oscillations are evolving in the R_{xx} (black) as the magnetic field increases. Although disturbed, this is a clear sign of the ballistic quantum Hall edge channel transport. Most convincing, the mobilities $\mu_{HB1} = 249 \times 10^3 \text{ cm}^2/\text{Vs}$ and $\mu_{HB2} = 227 \times 10^3 \text{ cm}^2/\text{Vs}$, determined from the low field data, can be compared to those of the macroscopic characterization Hall bar. Other than in Q2745 I and in ion milled samples, the miniaturization has no influence on the mobility in Q2745 III.

QC0167. As the indenting of contact mesa seems not to improve the sample performance, the design of QC0167 is kept straight and simple. No further changes have been made in the first sample to be fabricated on a different wafer. The $(2 \times 4) \mu\text{m}^2$ Hall bars are contacted close to the structure and covered with a SiO₂-Si₃N₄ insulator gate electrode [see Fig. 3.2 (a) and (b)].

The longitudinal (black) and Hall resistance (red) plotted against magnetic field in Figure 3.2 (c) allow to calculate a carrier mobility of $\mu = 108 \times 10^3 \text{ cm}^2/\text{Vs}$, two times smaller than obtained in the characterization of QC0167. Below 3.5 T, the quantum Hall plateaus in R_{xy} can be distinguished up to $\nu = 2$. In higher magnetic field, the curve strongly deviates and remains beneath $\nu = 1$. The implied SdH oscillations in the R_{xx} appear rather vestigial. The robust QH effect occurs to be disturbed particularly in higher magnetic fields.

The Hall resistance in the p-conductive regime of the Hall bar in Figure 3.18 (d) exhibits a long plateau. With increasing magnetic field the R_{xy} at a gate voltage $V_g = -0.7 \text{ V}$ (red) linearly decreases, betokens plateau $\nu = -2$ and quantizes at $\nu = -1$. The resistance remains in the conductance of one single edge channel up to a magnetic field of 4.5 T. However, for slightly different gate voltages the plateau in R_{xy} is less pronounced and

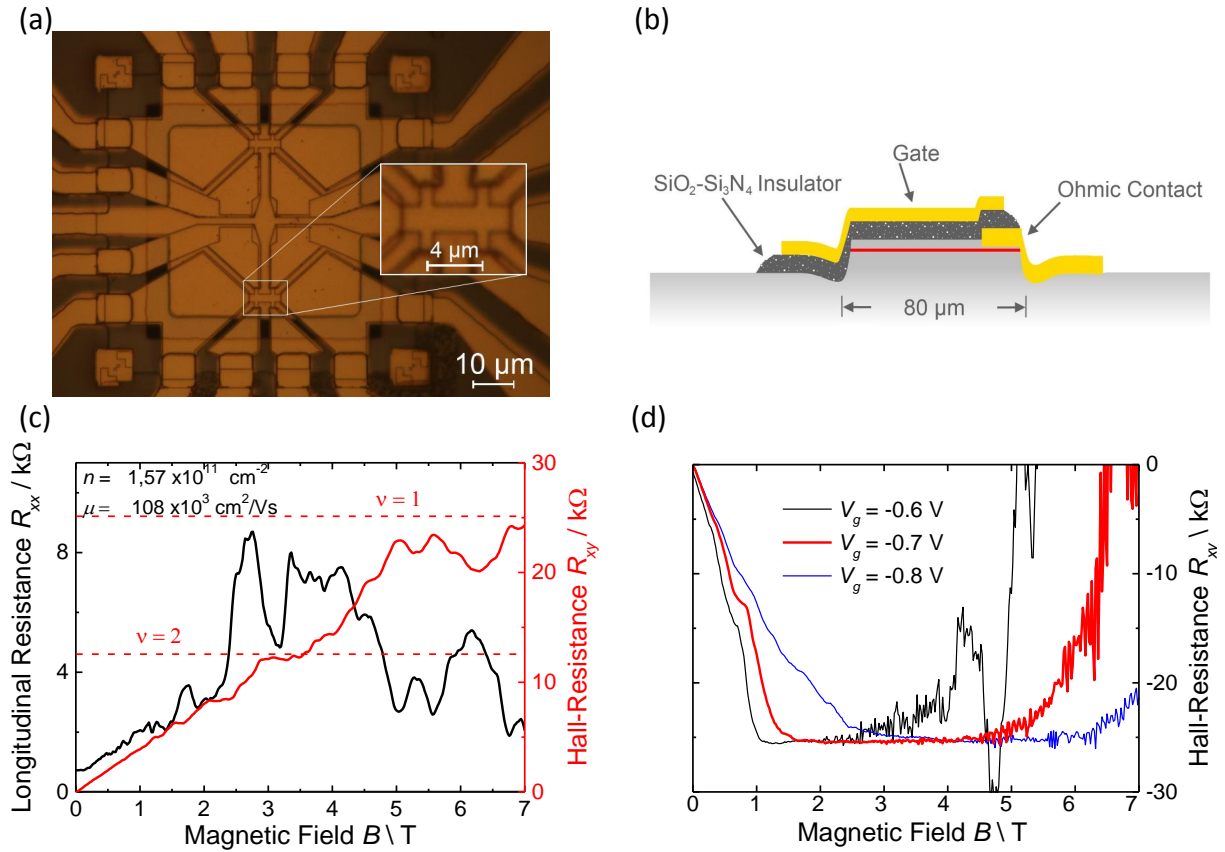


Figure 3.18: **QC0167**. (a) Micrograph of the 80 μm write field with two similar Hall bar structures. The outline shows a zoom onto the Hall bar schematically depicted in (b). The ohmic contacts are in 2 μm distance to the Hall contacts and covered by the Si₂O-Si₃N₄ insulator gate electrode. (c) Longitudinal (black) and Hall resistance (red) plotted against the magnetic field. (d) p-QH resistance at different gate voltages plotted against the magnetic field with the unusual long $\nu = -1$ quantization.

remains disturbed (d, blue and black). Density inhomogeneities and the thereby evolving potential puddles within the Hall bar might not only explain the lowered sample mobility and the disturbances on the n-conducting QH (c), but also effect the p quantization in (d). Mostly disturbed at high magnetic fields, an influence of the field on the ohmic contacts cannot be excluded.

Gate sweeps are conducted at zero magnetic field. In Figure 3.19 the longitudinal resistances of the two Hall bars on the device are plotted against the gate voltage (left and right) in top and bottom measurement configurations along the current path (black and red). In the energy gap from $V_g = -0.3 \text{ V}$ to $V_g = -0.6 \text{ V}$ the R_{xx} fluctuate around 12.9 KΩ, expected for the QSHE. However, different in the progression of the gap resistance ($V_g = -0.3$ to -0.7 V) from Hall bar to Hall bar (left and right), the divergences

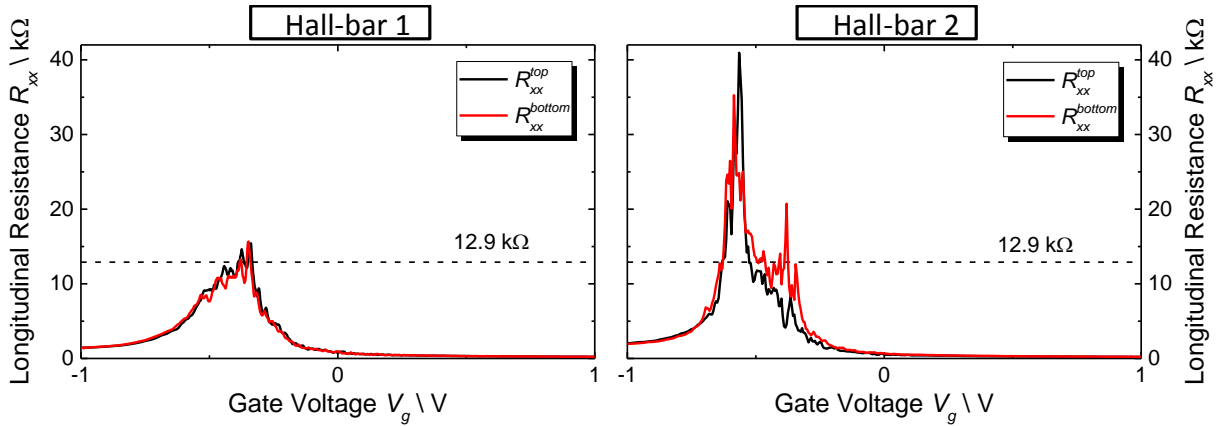


Figure 3.19: **QC0167**. Longitudinal resistance R_{xx} plotted against the gate voltage. In both Hall bars, the resistance of the back (red) and forth sweep of the gate voltage (black) are around the expected $12.9 \text{ k}\Omega$ in the gap area from $V_g = -0.3 \text{ V}$ to $V_g = -0.6 \text{ V}$, but do not exactly reproduce.

in measurements along top (red) and bottom edge of the Hall bar (black) are minimal. Thus, the deviations from the QSH signals seem to be of the same or similar origin in both measurement configurations. Possible mechanisms for backscattering are discussed in *The Quantum Spin Hall Effect* on page 76.

Even though, the low field magneto resistance in the n -conducting regime, the pronounced p quantization and the QSH resistance close to e^2/h are of novel quality. The high field magneto resistances and gate sweeps also indicate perturbations, influencing the sample performance. Further effort is required, to distinguish possible damage of the wet etch process from those possibly induced by the subsequent lithography for contacting and gating. After their measurements the samples are therefore examined in an SEM microscope in the search of potential and ‘visible’ reasons.

Figure 3.20 (a) shows the SEM image of one of the Hall bars on QC0167. The sidewalls from the metalization of the ohmic contacts are covered by the insulator gate electrode. They originate from an improper metalization process for the ohmic contact application. Their occurrence is schematically explained in Figure 3.20 (b) and (c). The 130 nm thin PMMA lift of mask is damaged and reduced by the ion milling in the (Cd,Hg)Te cap layer removal. AuGe/Au contacts are deposited in the etched contact and on the PMMA. Due to the reduced height and damage from the previous dry etch step, the shape of the lift-off mask enables deposition along the edges. In the lift-off, the PMMA is removed with the covering metal layer. The elevations along the contact edges, however, can remain as sidewalls. (d), once covered with the insulator and the gate electrode,

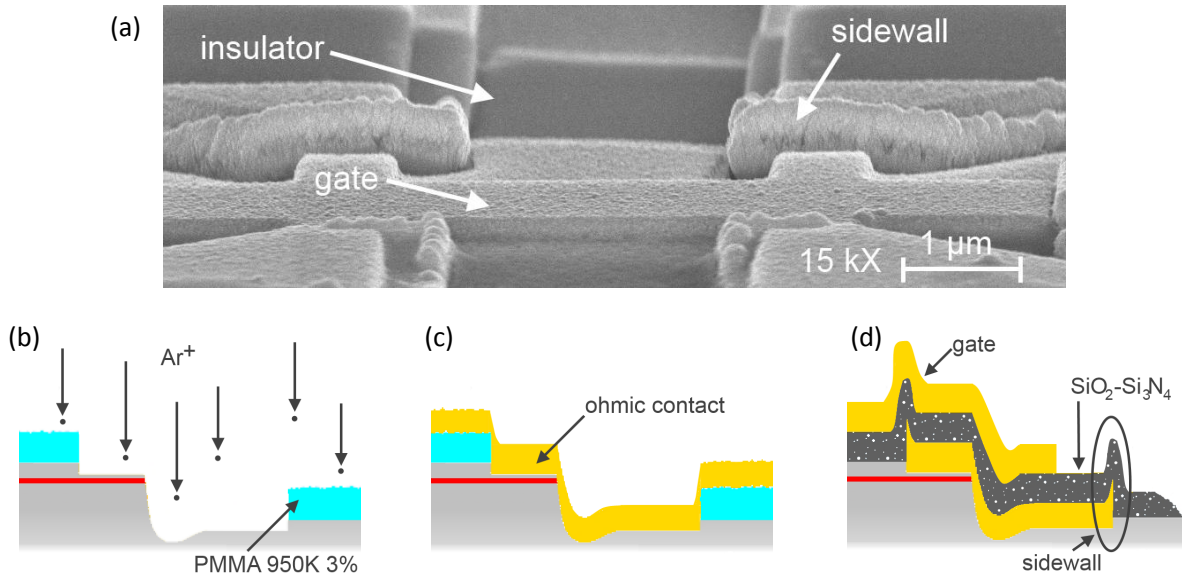


Figure 3.20: **(a)** SEM image of the wet etched micro Hall bar QC0167. The sidewalls from the ohmic contact metalization covered beneath the insulator gate electrode result in the inhomogeneous elevations along the ohmic contact transition. Their occurrence is schematically depicted in **(b)**-**(d)**. **(b)** The single PMMA layer is used to etch the (Cd,Hg)Te cap. The mask gets damaged and worn up. **(c)** In situ, the ohmic contacts are deposited. Due to the resist edge profile and the reduced height the metal deposits along the edges. **(d)** After the lift-off the deposition along the edge remains as sidewalls. Once covered beneath the insulator gate electrode they account for an inhomogeneous gating along the ohmic contacts.

the sidewalls can result in an inhomogeneous gate influence along the contacts to the QW.

Novel Contact Metalization

PMMA EBL resists are commercially available in different compositions and solutions as PMMA xxK x%. The xxK in the notation refers to the chain length of the polymethylmethacrylat molecules. The smaller the number, the shorter the chains and the more sensitive the resist to electron exposure and development. The x% refers to the solid percentage of the PMMA solved in ethylactat. The higher the percentage, the thicker the resist layer after spin-coating. Two goals are achieved using a PMMA 600K 6% and PMMA 950K 4% double layer resist¹. First, a double layer thickness of about 750 nm and second, a 600K bottom resist that is more sensitive to the electron exposure and subsequent development. If exposed and developed, the profile of the PMMA mask exhibits an

¹Each, spin-coat: 40 s 6000 rpm; resist bake: 10 min at 80 °C

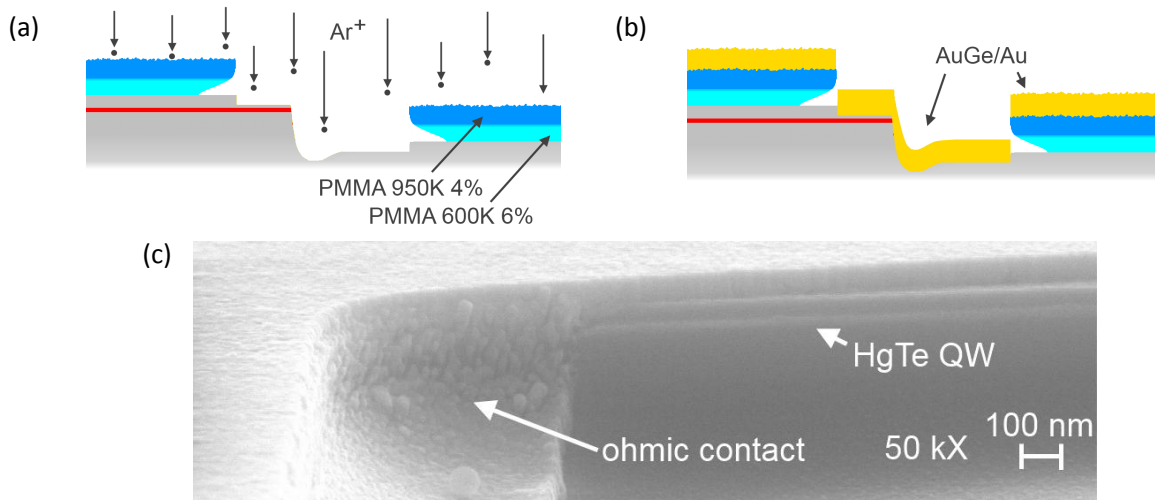


Figure 3.21: **(a)** Schematic of the (Cd,Hg)Te cap layer ion milling with the double layer resist. Although worn out, the thick PMMA mask allows the use as lift-off mask. **(b)** In-situ ohmic contact metalization. Due to the undercut no metal deposits along the mask and exactly aligns with the previously etched trench. **(c)** SEM image of an ohmic contact processed with the in-situ double layer technique.

undercut².

The novel contact metalization is schematically depicted in Figure 3.21:

(a) The PMMA is used as an etch mask. During the ion milling the (Cd,Hg)Te cap gets removed, but the PMMA is damaged and gets worn out. Due to its thickness the resist is still usable as a lift-off mask.

(b) Up to 300 nm AuGe/Au can be deposited and the lift-off results in a sharp metalization edge in the previously etched ohmic contacts. The undercut in the resist profile prevents the deposition along the mask edges and thereby the creation of sidewalls. The combined and self-aligned etch and metalization steps are executed in situ.

(c) shows a SEM image of an ohmic contact onto a wet etched mesa structure and after the lift-off process in acetone. The contact metalization aligns exactly with the contact etch, down to 25 nm above the QW. No sidewalls are present. Even though only 150 nm metal are deposited, the ohmic contact is one connected layer along the much higher wet etch mesa rims. Unlike the abrupt mesa rims from the dry etched process, the diffusive wet etch profile enables deposition on the diffusive etch profile.

Q2745 IV. Beside the application of the novel contact metalization, other pro-

²Area dose: 300 $\mu\text{C}/\text{cm}^2$; Acceleration voltage: 30 kV Aperture: 20 μm ; Magnification: 890 X; Working Distance: 10 mm; 12.5 nm = 4 pixel. Development: 1 min 20 s in 1:1 IPA : AR 600-56 (IPA:MIBK)

cesses have been adopted in the fabrication of Q2745 IV. Figure 3.22 (a) shows a micrograph and (b) a schematic of the Hall bars. The write field size is increased to 200 μm , enlarging the ohmic contact area. The insulator gate electrode is fabricated with the novel low temperature ALD HfO_x in the self-aligned process using optical negative resist [see Page 22]. The current and voltage probes are given a triangular shape, avoiding channel effects in the leads [see inlay in Fig. 3.22 (a)].

Longitudinal (black) and Hall resistance (red) are plotted against the magnetic field in Figure 3.22 (c). Other than in previous samples, the Hall plateaus in R_{xy} and SdH oscillations in R_{xx} are distinct up to high magnetic fields. Apparently, larger ohmic contacts improve their magnetic field performance. The overshoots, most pronounced on the $\nu = 2$ plateau from 4.5 to 6.5 T, can be attributed to density inhomogeneities within

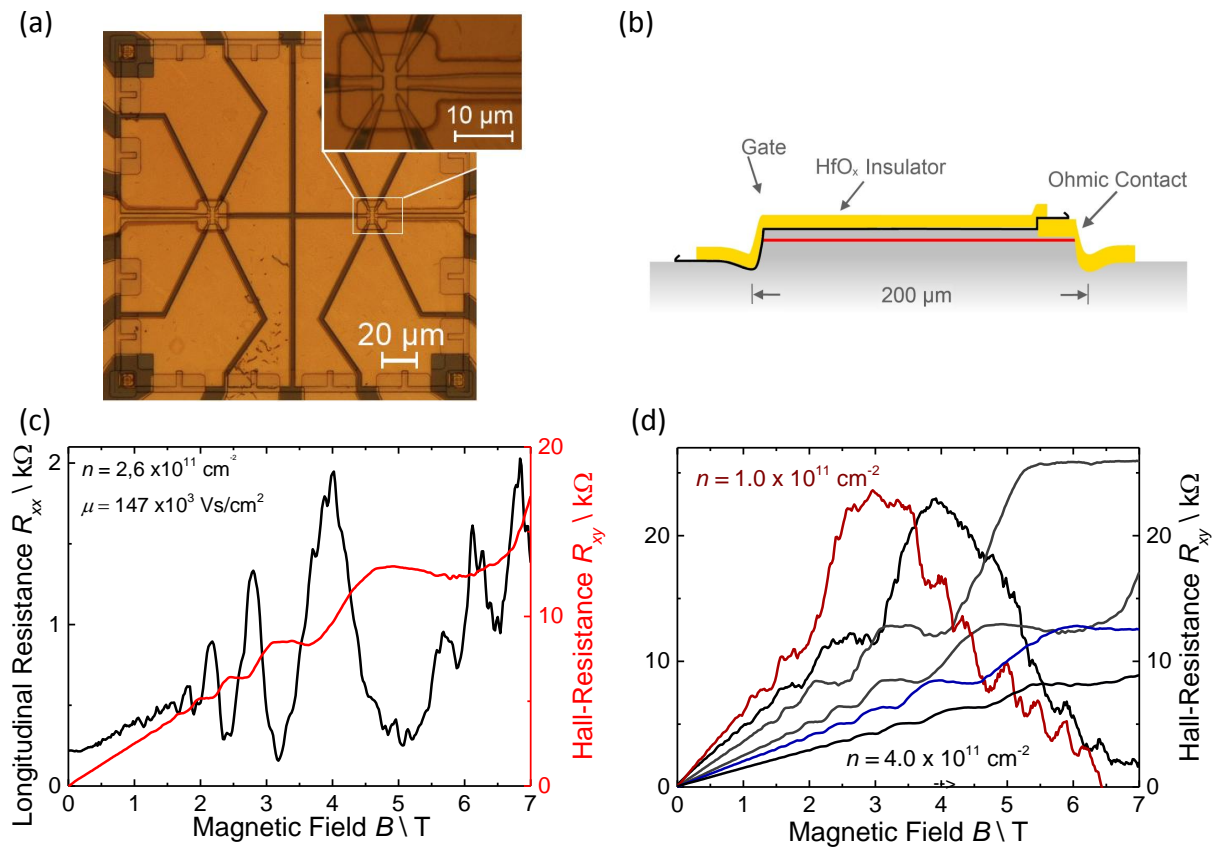


Figure 3.22: **Q2745 IV**. (a) micrograph and (b) schematic of the 200 μm wide write field. The ohmic contacts are applied with the novel double layer, reaching 2 μm close to the Hall bars and beneath the optically defined HfO_x gate. (c) Longitudinal (black) and Hall resistance (red) of one Hall bar plotted against the magnetic field. (d) Hall resistance as a function of magnetic field for various gate voltages and electron densities in the n-conducting regime.

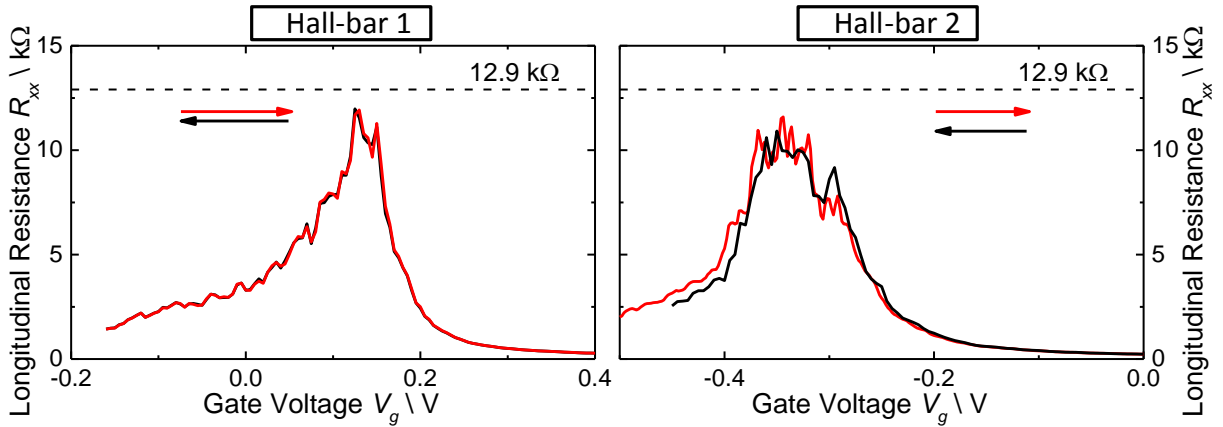


Figure 3.23: **Q2745 IV**. Longitudinal resistance R_{xx} as a function of gate voltage for both Hall bars. The resistance of the back (red) and forth sweep of the gate voltage (black) remain below the expected $12.9 \text{ k}\Omega$ in the energy gap and Hall bar 2 does not exactly reproduce.

the Hall bar [60]. The Hall resistances, plotted against magnetic field for densities from $n=4.0 \times 10^{11} \text{ cm}^{-2}$ (black) to $n=1.0 \times 10^{11} \text{ cm}^{-2}$ (purple) in Figure 3.22 (d), confirm density variations within the sample: Due to the steep Hall slope at low carrier concentration, a variation in n results in a higher change in resistance. Thus, the top left measurements at lower densities are disturbed stronger (d).

Figure 3.23 shows the longitudinal resistance of both Hall bars on the device, plotted against the gate voltage. Their resistance in the energy gap does not quantize but remains below the expected value of e^2/h . The non-matching conductance can be explained by parallel conductance along the R_{xx} or a distinct backscatterer, effectively changing the 6 terminal configuration and thereby the expected value. Although the reason for the lowered gap resistance cannot be ruled out, it is possible that the ion milling of the (Cd,Hg)Te cap in the ohmic contact step might introduce further dry etch doping and thereby parallel conductance similar to that found in Hall bars with purely dry etched mesas [see *The Conventional Dry Etch Method* on page 31].

QC0285. To minimize possible influence of the ion milling and metalization step for the ohmic contacts within the EBL write field, this step has been omitted. To further avoid a freeze-out of the uncovered voltage and current leads, such as reported for macroscopic samples on page 34, the bottom doped QW layer QC0285 is chosen. With a 70 nm thick (Cd,Hg)Te spacer and 10 nm layer of iodine doped I:(Cd,Hg)Te below the QW, the intrinsic density in macroscopic samples is determined to about $n=1.3 \times 10^{11} \text{ cm}^{-2}$. Thus, the leads are conductive. As to see in the micrography and schematic of the EBL write field in Figure 3.24, the mesa is only contacted via the optical metalization overlap into

the write field. The gated sample area is thereby not determined by the ohmic contacts, but the dimensions of the self aligned ARN process HfO_x insulator gate electrode **(b)**. Due to an alignment shift, the gate is not fully symmetric [see inlay in **(a)**].

Figure 3.25 shows an overview of measurements obtained in this sample. **(In the center)**, the gate sweep of the longitudinal resistance is shown for the two configurations in both Hall bars (left and right). They are surrounded by magneto resistance measurements of R_{xx} and R_{xy} as a function of magnetic field for various gate voltages: **(At the top)** with decreasing V_g and electron density n from right to left and **(at the bottom)** with low n density on the left and increasing p density to the right. Three main observations can be stated:

First, the Hall plateaus and Hall resistance follow the predicted curvature at all densities. As shown in Figure 3.25 (top right), the SdH oscillations decrease to zero in the insulating regime of pure edge channel transport above 3 T. No backscattering is enabled in the spatially separated QH edge channels through the $2\ \mu\text{m}$ wide Hall bar. The Landau levels are energetically separated and distinguishable. Solely the bottom left magneto resistance at very low density shows an overshoot in the R_{xy} plateau transition to $\nu = 1$ at 1.5 T, pointing to a minor inhomogeneity within the structure.

Second, the HfO_x gate insulator system allows hysteresis free gating from 0 to -0.7 V.

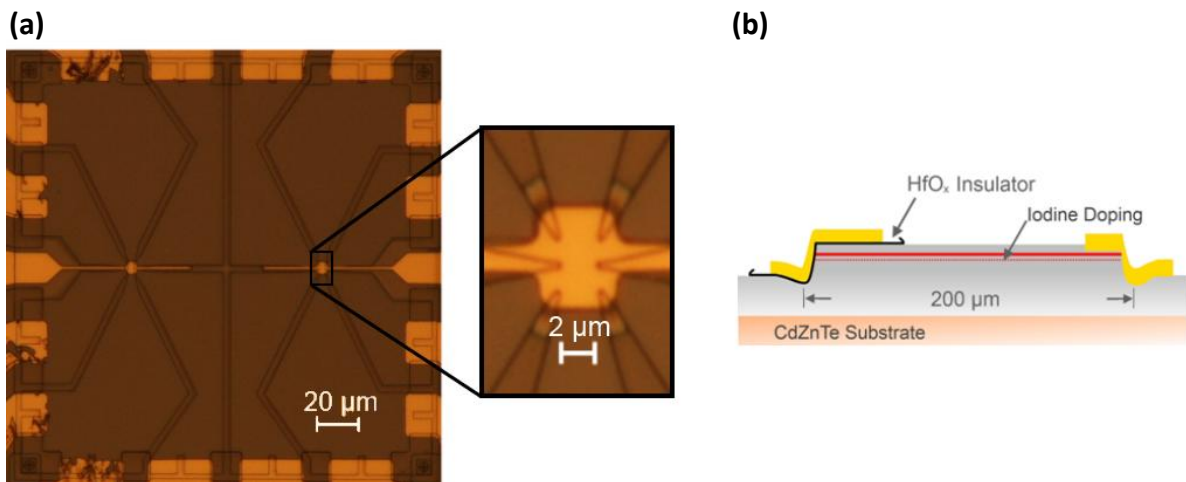


Figure 3.24: **QC0285**. Micrograph of the EBL write field **(left)**. The ohmic contact application via EBL is left out and the QW is solely contacted using the optical dry etch and metalization step overlapping into the EBL write field. The zoom onto the Hall bar **(right)** shows the HfO_x insulator gate electrode fabricated using the self-aligned ARN process. The structure in the trenches of the mesa is the ALD insulator which grew into the here more pronounced undercut. The less accurate optical alignment results in a slight asymmetry of the gate electrode.

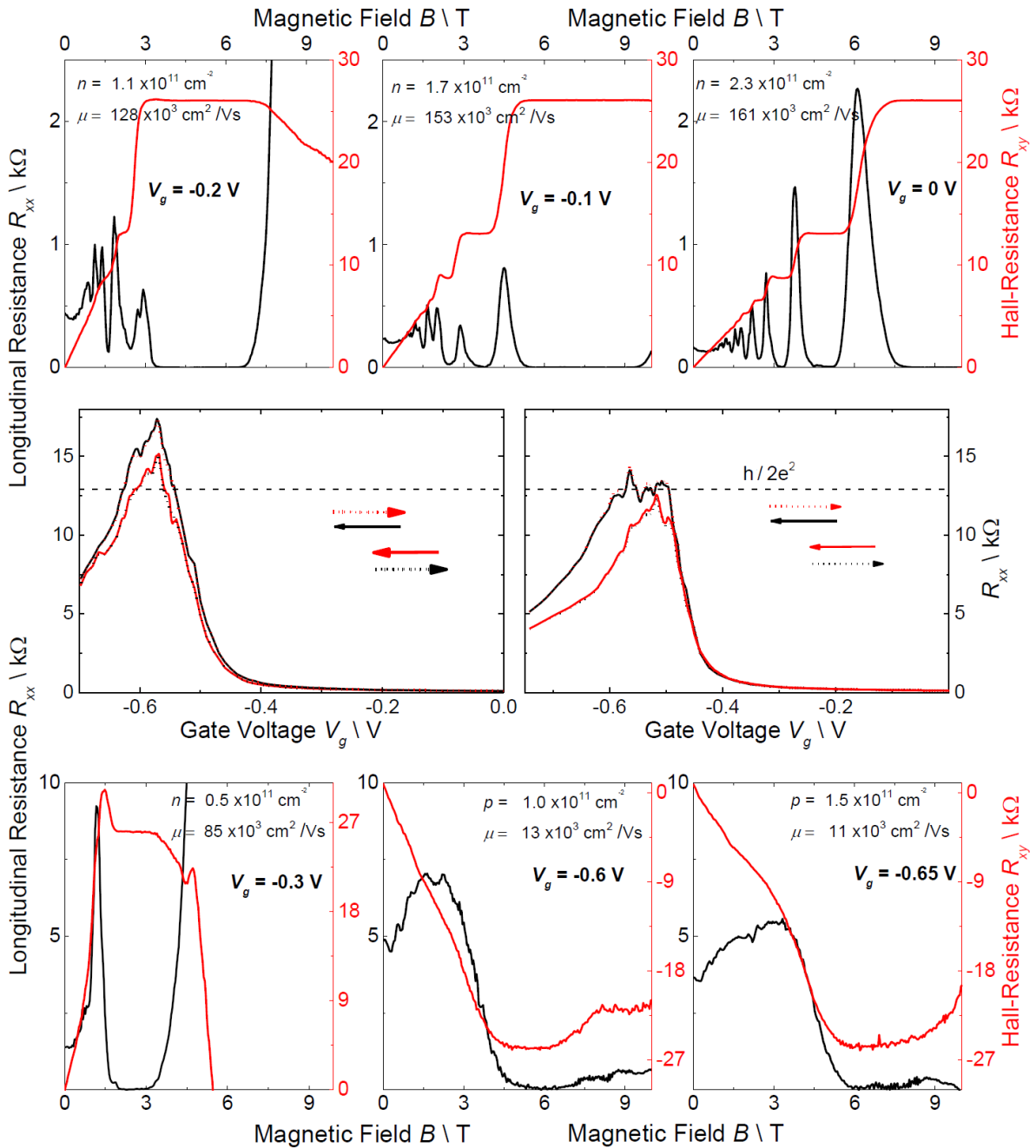


Figure 3.25: **QC0285**. Longitudinal (black) and Hall resistance (red) plotted against the magnetic field for various gate voltages: **(At the top)** with decreasing V_g and electron density n from right to left and **(at the bottom)** with a low n density on the left and increasing p density to the right. **(In the center:)** Longitudinal resistance R_{xx} plotted against the gate voltage. In both two Hall bars (left and right), the resistance of both configurations (red and black) are in perfect alignment with their back (dotted) and forth sweep (straight) and the gap resistances varies around the $12.9 \text{ k}\Omega$ (dashed black line).

From the n-conducting - over the energy gap - to the p-conducting regime. In the gate sweep of both Hall bars, plotted left and right in the middle, back (red) and forth sweep (black) result in the exact same longitudinal resistance values. All measurements within this gate range are reproducible.

Third, the longitudinal resistance in the inverted energy gap between the n and p-conducting regime for all configurations and in both Hall bars is close to the expected value of $12.9\text{ k}\Omega$. However deviating by a few $\text{k}\Omega$, one of the configurations in the right gate sweep shows a broad and pronounced plateau accurately quantized at $h/2e^2$. Since its first measurement and experimental proof in 2007 by Koenig et al., the quantum spin Hall effect has never been measured in such quality [10]. With the relatively large gate electrode the quantized signal requires a stable and undisturbed QSHE along more than $10\text{ }\mu\text{m}$ of the mesa edge. It thereby is the longest QSHE path ever observed. The oscillations on the QSH plateau, its temperature and magnetic field dependence as well as the peaks within the plateau are discussed in detail in *The Quantum Spin Hall Effect* on page 76.

The measurements on QC0285 prove the process adaptations to increase the quality. Despite the smaller ohmic contact area, the 3-point contact resistances still range from 1 to $5\text{ k}\Omega$. The determined mobilities are as high as in the macroscopic characterization sample. Neither the wet etching, nor the HfO_x insulator gate electrode introduce further inhomogeneities enhancing backscattering of the bulk carriers in the system. With a large hysteresis free range of the gate, the doped QW can be tuned from the n, to the p-conducting regime via the QSHE in the energy gap. Further than ever before on doped samples.

QC0348. Once more, this sample is fabricated on a bottom doped wafer and the ohmic contact is only provided by the metalization overlap from the optical metalization. As to see in the micrograph and schematic of one of the write field in Figure 3.2 (a) and (b), the two Hall bars on the sample are individually processed in two $200\text{ }\mu\text{m}$ write fields with nine contacts each. This allows to increase the ohmic contact size, requires less accuracy in the mask alignment and enables to design the contact leads symmetric around the structure. This is the first sample that is wet etched with a small frame around the write field to ensure a proper HgTe QW etching and etch start [see page 41]. Other than QC0285, the HfO_x gate electrode is applied using the EBL PMMA double layer process [see page 25]. This ensures an accurate alignment of the gate on the Hall bar and, as a smaller gate, reduces the length of undisturbed edge channels, required to measure proper QSH signals [see inlay in Fig. 3.26 (a)].

The leads to the Hall bar are neither gated, nor metalized. The regions of different densities along a lead are indicated in the schematics of Figure 3.26 (b): increased and variable underneath the gate (n^+), intrinsic and lower in the leads (n^-) and metallic in

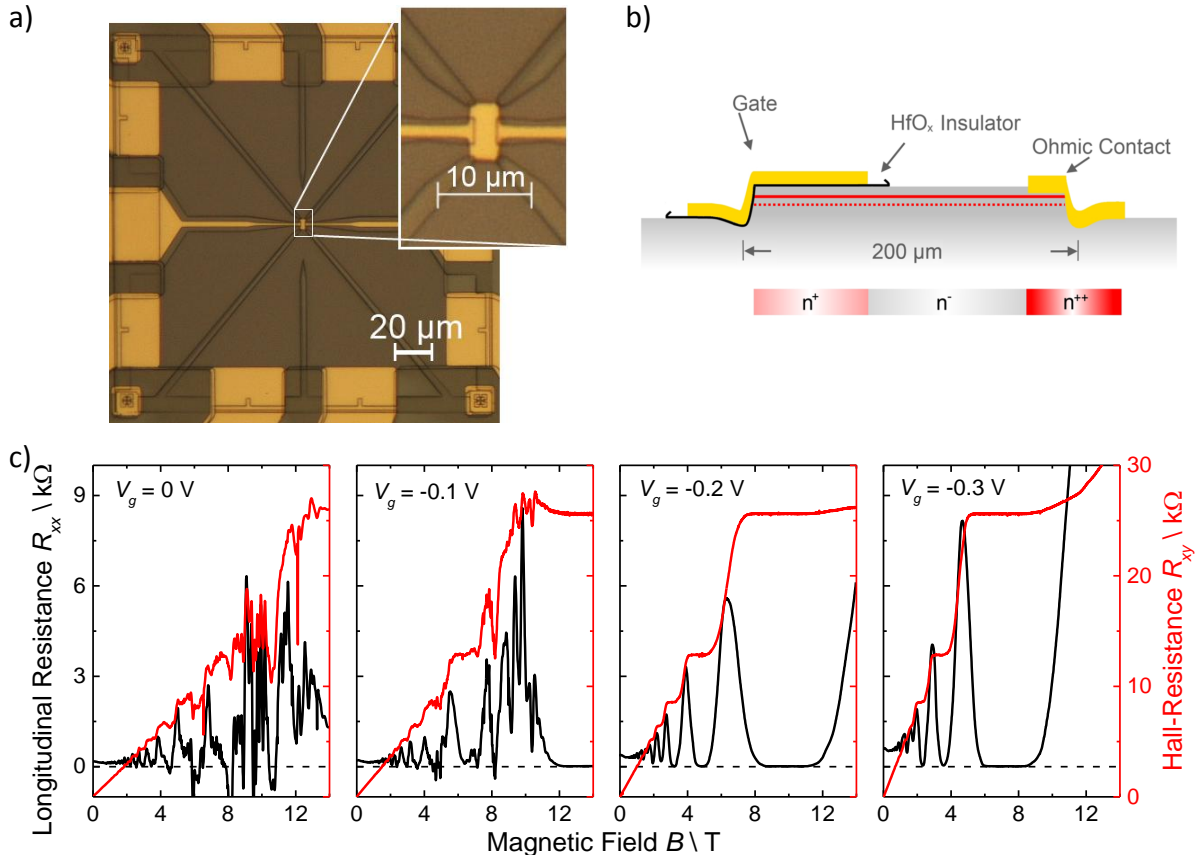


Figure 3.26: **QC0348**. (a) Micrograph and (b) schematic picturing one of two EBL write fields on the sample. The nine contacts (n^{++}) are overlapping from the optical into the EBL write field. The mesa leads (n^-) are symmetric around one centered Hall bar. As shown in the zoom, the EBL gate (n^+) is accurately placed on the structure. (c) Longitudinal (black) and Hall resistance (red) plotted for different gate voltages. The electron density is thereby decreased with V_g from the left to the right. $R_{xx}=0$ is indicated as the dashed black line.

the ohmic contacts (n^{++}). Their mismatch is responsible for an effect that is very distinct in this, but has also been observed in other samples.

Figure 3.26 (c) shows the Hall (red) and longitudinal resistance (black) for different gate voltages plotted against the magnetic field. At a gate voltage of $V_g = 0$ V and an elevated density in the structure, both the R_{xx} and R_{xy} reproducibly fluctuate. The fluctuation amplitude increases towards higher magnetic fields. With a partly negative longitudinal resistance, there is no physical explanation given within the theory of the QHE. Lowering the density by reducing the gate voltage (from left to right in Figure 3.26) reveals nicely quantized Hall plateaus and an undisturbed SdH signal with well separated Landau levels and no negative resistance. The disturbance is related to the density beneath the gate.

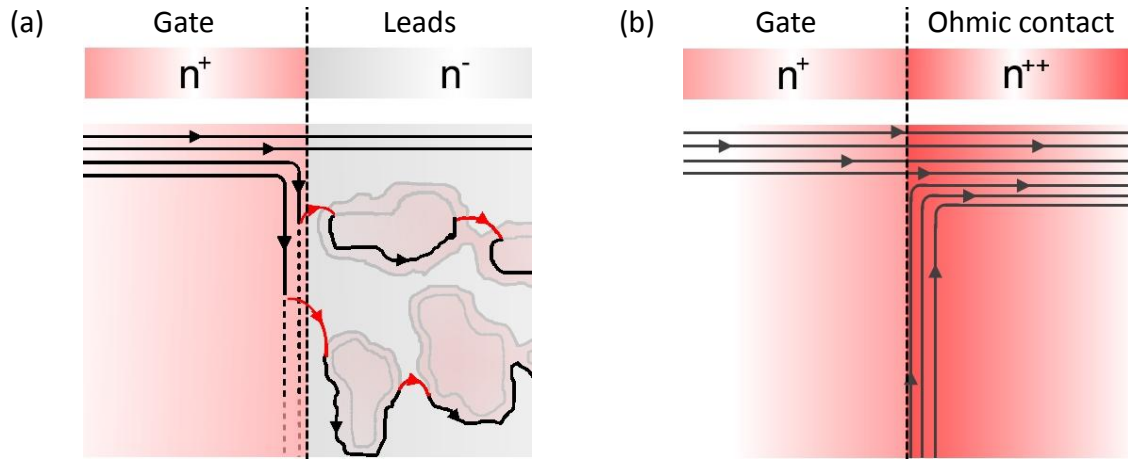


Figure 3.27: Schematic along the mesa edge of the transition from (a) gated (n^+) to non-gated mesa and (b) gated to metalized mesa. The QH edge channels are pictured in black, the charge puddles in gray and the hopping transport is depicted with red arrows.

Figure 3.27 (a) shows a schematic of the mesa edge along the transition of the area with and without gate on the lead to the contact. In magnetic field and with a higher electron density beneath the gate (n^+), more QH edge channels (black) are present than available in the contact leads (n^-). In the lack of a counterpart, the remaining edge channels propagate following the potential barrier. Density inhomogeneities along the contact leads, however, allow conduction through the insulating phase, dominated by nearest neighbor hopping between localized conducting puddles [62]. The conduction through their QH channels depend on the details of the various narrow junctions separating the

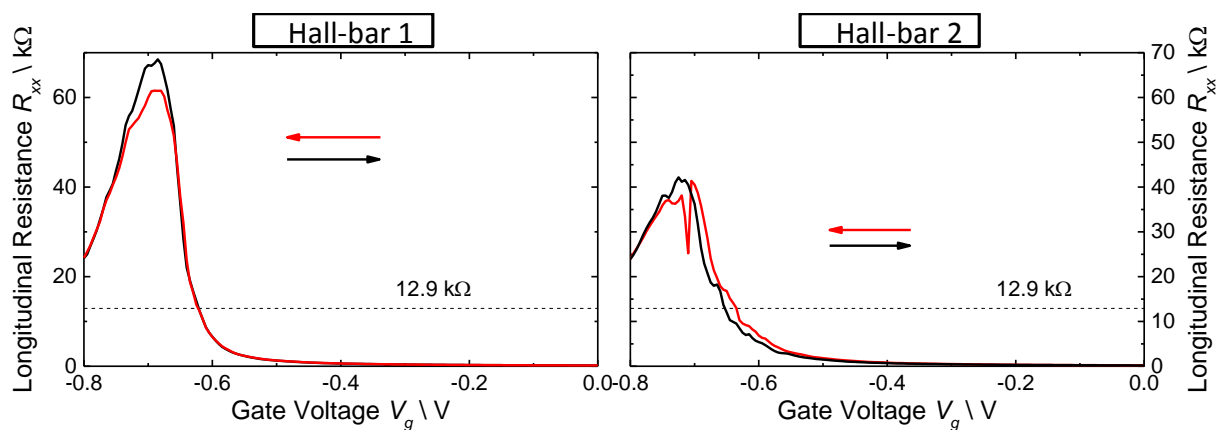


Figure 3.28: **QC0348**. Longitudinal resistance R_{xx} plotted against the gate voltage. In both Hall bars, the resistance of the back (red) and forth sweep of the gate voltage (black) remain above the expected $12.9 \text{ k}\Omega$ (dashed black line) in the energy gap and do not exactly reproduce.

puddles. Hopping parameters and puddle configuration are dependent on the applied magnetic field [63, 64]. Thus, the voltage probes along the Hall bar measure fluctuating potentials. The fluctuation amplitudes in higher magnetic field increase, as fewer edge channels are present. A break-down of the transparency of one single edge channel thereby creates a larger peak in resistance. The increase of fluctuations with density in Figure 3.26 (c) can be explained by the rising QH edge channel mismatch. The reproducible fluctuations thereby represent a fingerprint of field dependent puddle configuration and hopping parameter in the contact leads.

A direct transition from the gated to the metallic regime is schematically pictured in Figure 3.2 (b). With more edge modes present in the metallic contact the QH channels in the gated regime are more likely to couple to the contact.

Conducted at zero magnetic field, the gate sweep measurements are not disturbed by this artifact. Figure 3.28 show the longitudinal resistance of the two Hall bars on the sample plotted against the gate voltage. Both exceed the QSHE value and back (black) as well as forth sweep (red) do not reproduce properly. Other than the optical gate on QC0285, QC0348 is equipped with a self aligned PMMA ALD insulator gate electrode. Trap states arising from possible PMMA residuals may cause deviations, if charged and discharged.

In the following, the contact issue at high densities and magnetic fields is ruled out by a comparisons of contacts in varying distances to the Hall bar. The influence of possible PMMA residuals onto the sample performance is tested in *QC0167 II*, *QC0348 I and II* - *MIBK-Cleaning* on page 66.

QC0347 I, II and III - Contact Configuration. Three comparison samples are build on the doped wafer QC0347 with ohmic contacts (a) far, (b) close and (c) in proximity to the Hall bar. The role of the lower density contact leads is examined by a large (a), a small (b) and no n^- transition through non-gated contact leads (c) [see Fig. 3.29]. All gate insulator electrodes are applied with the optical self aligned ARN process and the low temperature ALD HfO_x [see page 25].

The consequence of the contact lead types onto the quality of the longitudinal (black) and Hall resistance (red) at elevated densities around $n=5.5 \times 10^{11} \text{ cm}^{-2}$ are compared in Figure 3.29:

(d), large (n^-). The R_{xx} (black) and R_{xy} (red) are strongly disturbed, reproducibly fluctuate in magnetic field and R_{xx} exhibits a partly negative longitudinal resistance.

(e), small (n^-). The magneto resistances appear to be less disturbed, at least for positive magnetic fields.

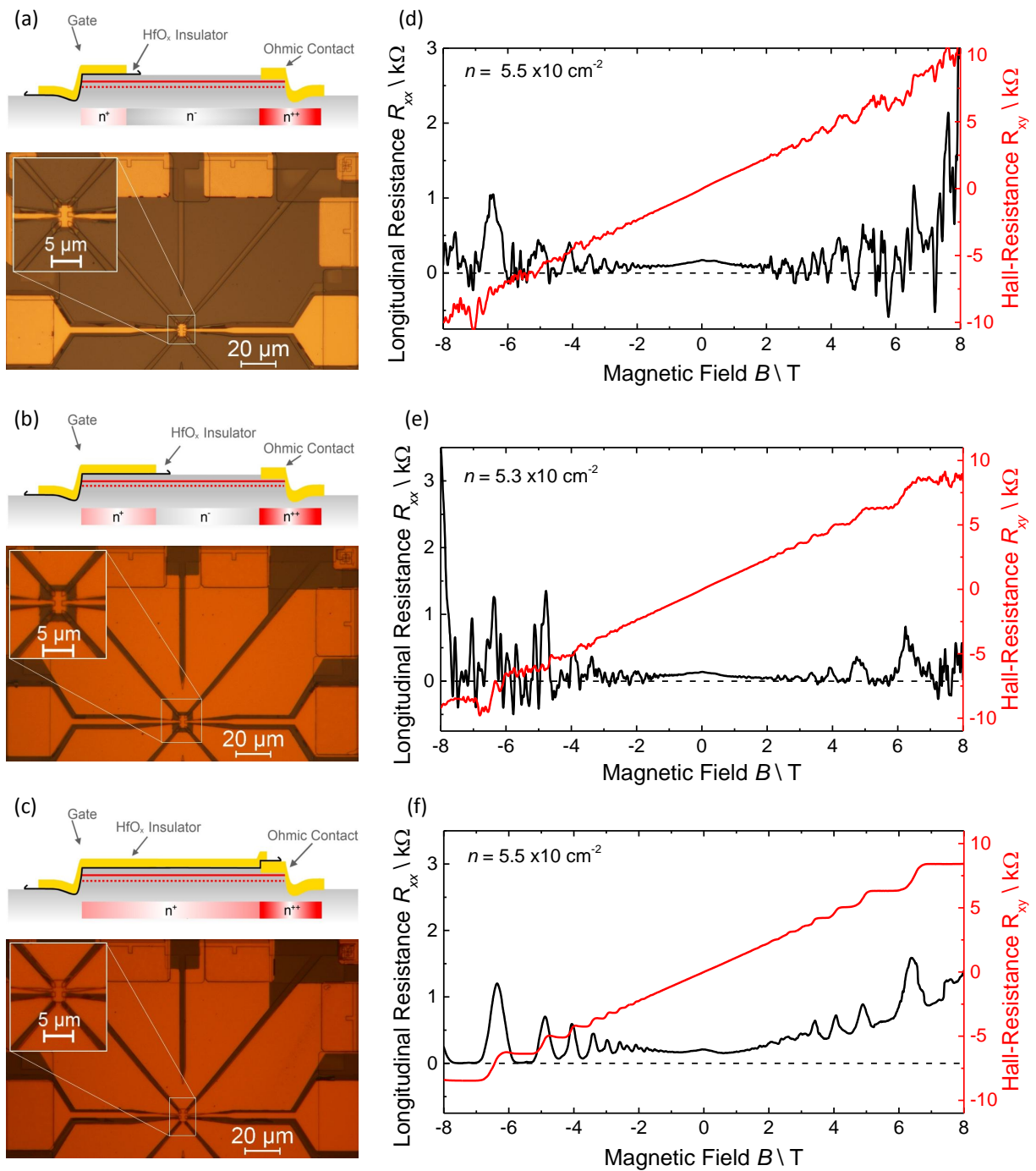


Figure 3.29: **QC0347**. Schematic and micrograph of the EBL write field of the Hall bars with the ohmic contacts (a) far, (b) close and (c) in proximity to the Hall bar. Longitudinal (black) and Hall resistance (red) of Hall bars plotted against magnetic field with the resulting large (d), small (e) and no n⁻ transition (f) through non-gated contact leads.

(f), no (n^-). The Hall bar shows no fluctuations in the magneto resistance measurement. The influence of the density and conductivity transitions from the contacts (n^{++}) through the non-gated leads (n^-) to the gated Hall bar (n^+) becomes most appealing if the low density leads are avoided by ohmic contacts ending beneath the gate in proximity to the Hall bar. The Hall resistance (red) evolves properly from the linear Hall at low magnetic fields to the QH plateaus at higher magnetic fields. The longitudinal resistance (black) exhibits SdH oscillations whenever a Landau level is lifted above the Fermi level, goes to zero in the presence of pure edge channel conductance for negative magnetic fields and exhibits no negative resistance whatsoever. Its asymmetry in positive and negative magnetic field is a consequence of density inhomogeneities.

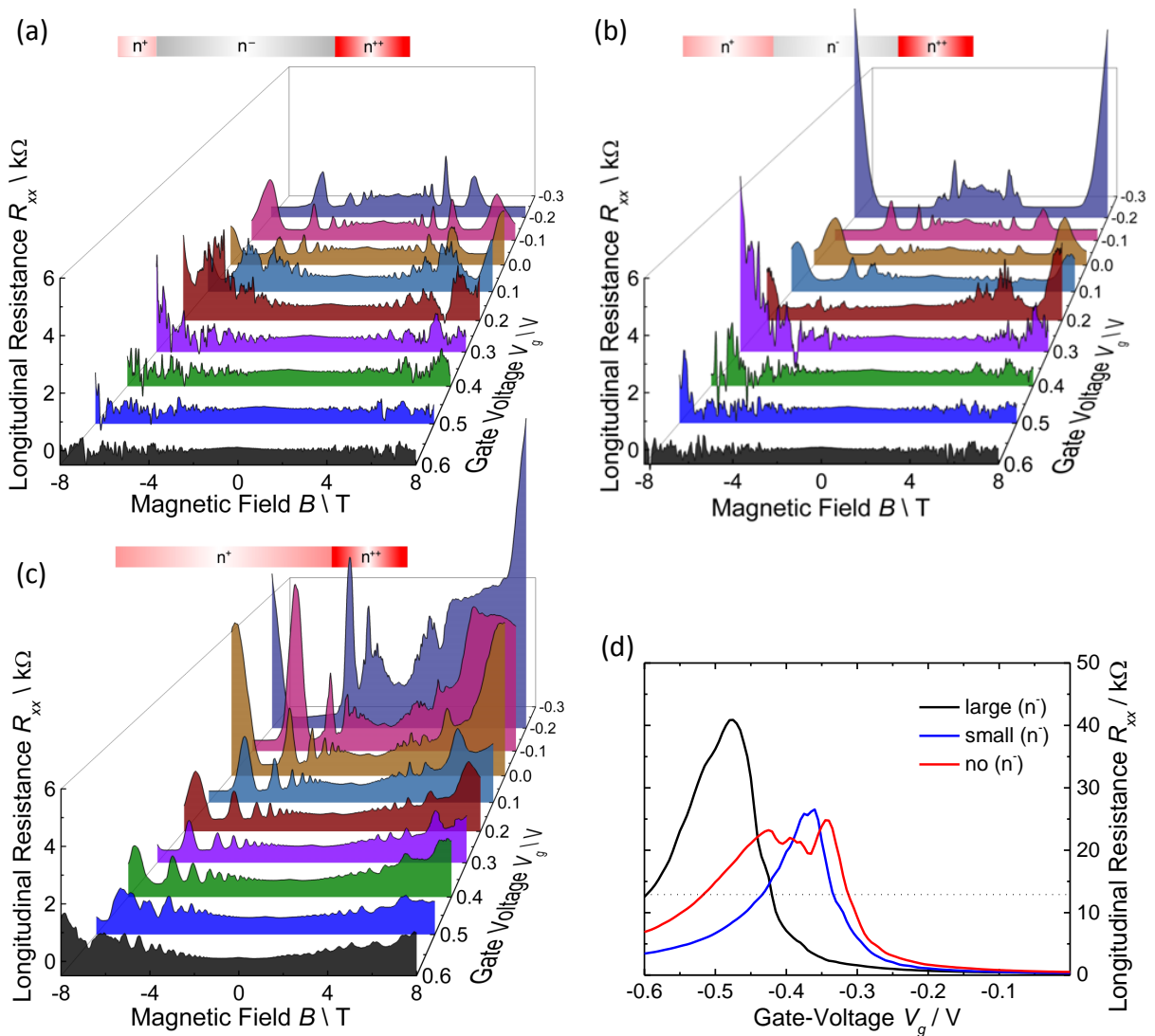


Figure 3.30: **QC0347**. Longitudinal resistance plotted against the magnetic field for various gate voltages of Hall bars with a large (**d**), small (**e**) and no n^- transition (**c**) in the contact leads and their gate sweeps at magnetic field $B = 0$ T in (**d**).

The evolution of the SdH-oscillations for different densities beneath the gate and the samples of different contact configurations are shown in Figure 3.30. Both Hall bars with non-gated contact leads (n^-) in **(a)** and **(b)** are non-disturbed at low gate voltages. As the density and edge channel mismatch is increased by gate voltage, the measurement of the R_{xx} is increasingly disturbed. Solely the Hall bar with a direct transition in the contact leads from the metalized to the gated leads in **(c)** shows no fluctuation in the longitudinal resistance at all gate voltages. Contacts close to the structure and overlapped by the gate electrode prove to result in a more stable magneto resistance.

With the n^- in the leads, leading to the fluctuations in the measurement only at elevated magnetic fields and high densities beneath the gate, no influence of contact distance can be determined onto gate sweep measurements at zero field. First, because no contact problem is ruled out for low densities close to the energy gap and in low magnetic fields. Second, other than the QH, the QSH edge channels are present at all densities and should fully transmit in the absence of scatterers. A non-quantized conductance must therefore be related to backscattering of the QSH edge channels. Figure 3.30 **(d)** shows the longitudinal resistance of the structure in all three contact configurations plotted against the gate voltage. The structures with a large (black) and small area of low density n^- in the contact leads (blue) have a peak in resistance. The Hall bar with no low density area in the contact leads, exhibits a plateau-like gap resistance. All gap resistances are above the expected value for pure QSH edge channel transport (dotted black line).

The increasing quality of the magneto resistance measurements reveals an asymmetry of SdH signals in positive and negative magnetic fields [see Fig. 3.2 **(c)** and Fig. 3.30 **(c)**]. Hereafter, it is shown, that those asymmetries can be related to density inhomogeneities within the Hall bar. Thus, the symmetry of SdH oscillations allows to judge on successful residual removal prior to the gate application.

Density Inhomogeneities in QH

The QHE edge channels propagate along the equipotential of the mesa edge. A non-uniform potential landscape in the structure can result in puddles such as described for the contact leads on page 60 [65]. Conductance along these puddles can lead to carriers reaching from one edge channel to the counter-propagating QH channel on the other edge of the structure. Backscattering through the insulating phase of the QHE is enabled, the resistance changes. The discrepancy from the ideal Hall and SdH resistance can be related to an interplay of an inhomogeneous potential landscape (density variations) and the applied magnetic field [66, 67, 68]. Symmetry arguments in the measured configurations allow to draw conclusions on the potential landscape.

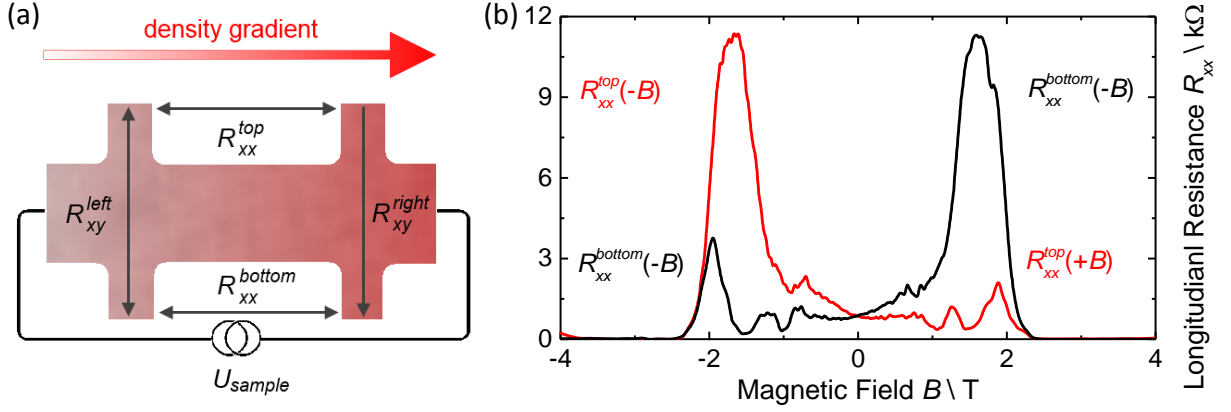


Figure 3.31: **(a)** Schematic of the measurement configurations of an Hall bar with a density gradient (red). **(b)** Top (red) and bottom longitudinal resistance (black) plotted against the magnetic field.

The counter-propagating QSH edge channels reverse their propagation direction if the magnetic field is inverted. This leads to symmetric measurement configurations of the resistances in undisturbed systems:

$$R_{xx}^{top}(\pm B) = R_{xx}^{bottom}(\mp B) \quad \text{and} \quad R_{xy}^{left}(\pm B) = R_{xy}^{right}(\mp B).$$

Inhomogeneities in density distribution and thereby potential landscape break the symmetry [69, 70]. A density gradient along the current path, as schematically displayed in Figure 3.31 **(a)**, for instance, reduces the symmetry in the longitudinal resistance R_{xx} to

$$R_{xx}^{top}(-B) = R_{xx}^{bottom}(+B) \neq R_{xx}^{top}(+B) = R_{xx}^{bottom}(-B).$$

Figure 3.31 **(b)** shows the longitudinal resistance plotted against the magnetic field in both configurations of a micro Hall bar on QC0167. The exchanged asymmetry of R_{xx}^{top} (red) and R_{xx}^{bottom} (black) in magnetic field can be related to a density gradient along the current path. Gradients perpendicular to the current path or smaller regions of density inhomogeneities (puddles) further break the symmetry.

The origin of an irregular potential landscape can be of intrinsic or extrinsic nature. With intrinsic reasons such as growth or doping defects, a thickness gradient in the QW or a rough wafer surface cannot be influenced in the lithography process. Extrinsic reasons, such as inhomogeneous gate influence through rough insulators or dirty interfaces, however, can be avoided and optimized with and during the process.

QC0167 II, QC0348 I and II - MIBK-Cleaning. PMMA residuals from the previous use as PMMA wet etch mask and PMMA lift-off resist in the double layer metalization of the ohmic contacts, are not fully removed in with acetone. Thus, the later applied gate electrode varies in distance to the QW and thereby results in an inhomogeneous gate influence and disturbed potential landscape, as schematically pictured in Figure 3.32 (a). A 12-hour bath in 50°C methyl isobutyl ketone (MIBK) removes PMMA residuals prior to the gate application [see schematic in (e)].

Four samples are fabricated in pairs of two from doped (QC0348) as well as undoped (QC0167) HgTe QW material. As a consequence of the previous results, the two Hall bars on each sample are equipped with EBL contacts close to the structure and an overlapping gate electrode [comp. Fig. 3.2 (a)]. All the lithography steps are carried out in parallel, but only one of a pair is treated with the MIBK cleaning prior to the ALD HfO₂ growth.

In Figure 3.2, the micro Hall bars without (left) and with an MIBK-cleaning step (right) are compared in their gate influence on the symmetry of the longitudinal resistance in magnetic field. The R_{xx} in the non-treated micro Hall bars in (b), (c) and (d) are asymmetric in magnetic field and distorted in the evolution of SdH oscillations. The higher the applied gate voltage, the stronger the influence of the interface contamination and the more distorted the signal due to enhanced backscattering [71].

The measurements on the MIBK-cleaned Hall bars in (f), (g) and (h), in contrast, are characterized by well distinct SdH oscillations symmetric in magnetic field and higher in resistance. With less density inhomogeneities, the insulating regime of the QHE is preserved, the Landau-levels are more discrete throughout the Hall bar and the SdH oscillation are higher in resistance.

The MIBK-cleaning is the last of many lithography adaptations within the frame of this work. In order to improve the sample performance, increase the processability and decrease the error rate, every lithography step has been optimized. In constant consideration of easy handling and with a primary focus on reproducibility, novel fabrication methods for macroscopic (optical) and microscopic (Ebeam) samples haven been developed and step by step approved in measurements:

- **The optical positive resist ECI 3027** can be used as wet and as dry etch mask for structure sizes larger than 2 μm. While the wet etch mask is properly stripped in acetone, it requires Technistrip P1316 to fully solve the sidewalls from redeposition of etched material and hardened resist in the ion milling process.
- **The optical negative resist ARN 4340** exhibits an undercut when developed. Usable as dry etch mask and lift-off resist, it enables an in-situ application of ohmic

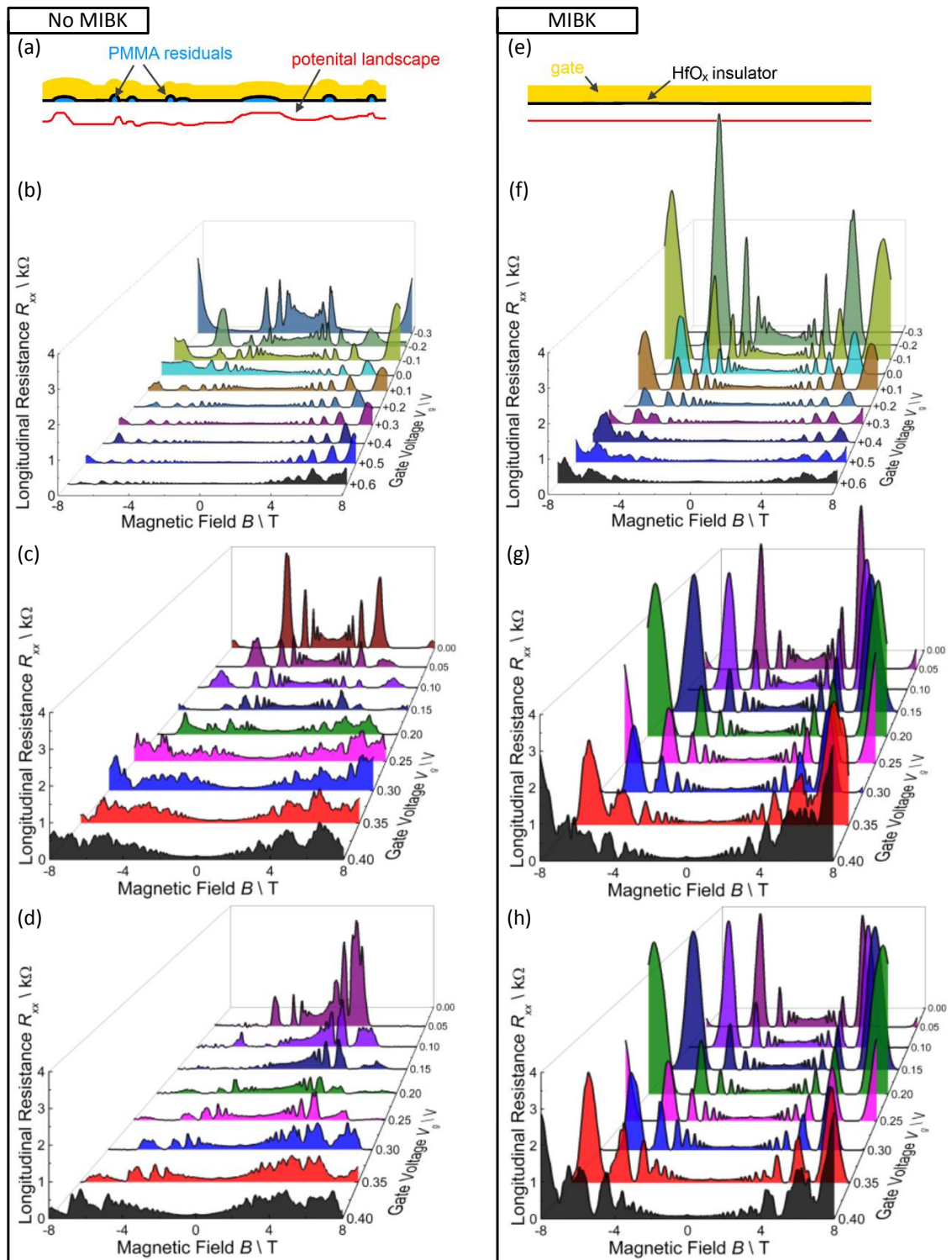


Figure 3.32: (a) and (e) Schematic of the potential landscape and longitudinal resistance plotted against the magnetic field for various gate voltages of non-treated (left) and MIBK-cleaned (right) micro Hall bars on the wafers QC0167 (b) and (f) and QC0348 (c), (d), (g) and (h).

contacts. First etching close to the QW, then metallizing AuGe. The undercut guarantees a clean lift-off with no sidewalls.

- **The HfO₂ ALD process at 34 °C** grows thin and homogeneous insulator layers that reproducibly withstand gate voltages from ± 10 V. Because of the low growth temperature, the HfO₂ can first be applied into lift-off masks, then be metalized with the gate electrode. The ARN 4340 and a double layer PMMA EBL resist enable growth into their undercut and a variable gate fabrication down to sizes of 50 nm.
- **The KI:I₂:HBr wet etch process** for micro and macro-mesa fabrication. Other than ion milling, it is harmless to the crystalline structure of the mesa and allows for samples in micrometer dimensions with no loss in electron mobility. In consideration of the diffusive etch character, any design can be realized within a 200 μ m write field.
- **The ohmic contact metalization** with the double layer PMMA enables self-aligned ion milling and metalization of narrow designed contacts close to the structure.
- **The MIBK-cleaning** of PMMA residuals on the mesa surface prior to the gate application minimize the influence of density inhomogeneities within the Hall bar.

On the following pages, process parameters, details and characteristics are summarized along an exemplary micro Hall bar process. Exchangeable in sequence and adoptable in design, the lithography steps can be seen as a tool box for (micro) structure fabrication.

3.3 The Novel Micro Hall Bar Process

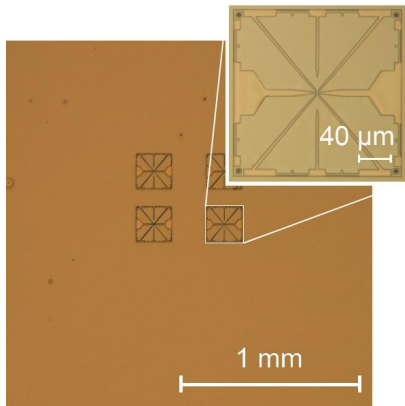


Figure 3.33: Micrograph of the EBL mesa in the $2 \times 2 \text{ mm}^2$ section of the later structure and zoom onto one write field. The sample is coated in PMMA, the bright part around the Hall bar and leads are EBL exposed, developed and etched via $\text{KI} : \text{I}_2 : \text{HBr}$ wet etching. The inner mesa is framed and decoupled from the outer wafer (zoom). The image is taken after the mask stripping in acetone.

The EBL mesa. A piece of the wafer is cleaned in acetone and isopropanol, spin-coated with *PMMA 950K 3%* for 40 s at 7000 rpm and baked at 50°C for 5 min. The later to etch areas of the write fields are exposed using an EBL system with an electron dose of $70 \mu\text{mC}/\text{cm}^2$, with an extraction voltage of 2.5 kV, a working distance of 7 mm, a write field size of $204.8 \mu\text{m}$, a magnification of 388 times and an SEM aperture of $30 \mu\text{m}$. The exposed PMMA is then developed in pure isopropanol for 1 min and cleaned in H_2O . The natural oxide of the exposed wafer is removed in an 50 s HF dip in a 1:200 solution of $\text{HF}:\text{H}_2\text{O}$ and directly etched with a solution of $(\text{KI}_{4.15\text{g}}:\text{I}_{0.1\text{g}}:\text{HBr}_{12.5\text{ml}})_{\text{to } 50\text{mlH}_2\text{O}}$ mixed 1:4 with H_2O flowing vertically on the sample surface for 25-30 s through a tube pump. The etching is stopped by a bath in H_2O .

Figure 3.33 shows a micrograph of the sample after the PMMA stripping in acetone and a cleaning step in H_2O .

- The Design of the later leads and contact pads require the EBL write fields to be placed in the middle of the piece of wafer.
- The process allows for the writing of several fields and later choosing the ones that are most homogeneously etched and show the least wafer defects.
- The mesa design within the write field can freely be adopted to the purpose of the sample.
- The isotropic etching has to be attributed in the design of the EBL write field [see page 41]. Due to the diffusive character of the wet etchant, the widest structure in the exposure design is etched the least.
- It is crucial to frame the EBL design with a line smaller than any dimension within the write field. This ensures that the frame is etched deepest and first. The conductive QW within the write field is thereby electrically disconnected from the outer wafer and the etch result is more homogeneous. With a non-framed design, the etching delays at the conductive HgTe and the QW layer may stand out from the rest of the mesa [see page 41].

- The HF dip prior to the actual etching removes the surface oxide, ensures a more homogeneous etch start and reduces the etch depth variation in areas of different width [see page 42].
- The etch time needs to be adopted to the design of the EBL mesa and the minimal etch depth given by the widest etched area. Severe changes in the design require additional etch tests.

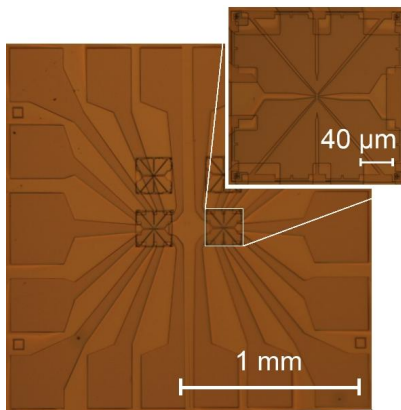


Figure 3.34: Micrograph of the optical mesa. Two write fields are chosen to be contacted, the sample is coated in optical resist, exposed using a mask aligner and developed. The write fields, the darker brown leads and contact pads are protected by the etch mask, the bright areas are etched via $\text{KI} : \text{I}_2 : \text{HBr}$ wet etching. The image is taken after the mask stripping in acetone.

The optical mesa. The sample is spin-coated with *ECI 3012* for 20s at 6000rpm and baked at 80°C for 2min. The optical mask is brought into contact with the resist surface in the mask aligner. The overlap to the EBL write field is aligned to the EBL mesa. The resist is then exposed with the Hg vapor discharge lamp for 5.6s at 8W and developed in *AZ 726 MIF* for 22s and rinsed in H_2O [see page 12]. The resist etch mask now covers the contact pads, the leads and most of the EBL write field. The uncovered wafer is etched for 40-60s using $(\text{KI}_{4.15\text{g}}:\text{I}_{0.1\text{g}}:\text{HBr}_{12.5\text{ml}})$ to 50ml H_2O mixed 1:4 with H_2O and the tube pump. The etching is interrupted in a bath of H_2O . Figure 3.34 shows a micrograph of the sample after the PMMA stripping in acetone and a cleaning step in H_2O .

- The optical mask design gives the option to independently choose the write fields.
- Other than the previous optical mask versions, all nine contacts per write field can either be used as gate or ohmic contacts [74].
- No HF dip is required prior to the etching. As the EBL mesa is already disconnected from the outer wafer, the optical mesa is solely etched to electrically separate the pads and leads from one another and does not contribute to the sample performance.
- No further mesa step is created from the bond pads through the leads to the write field. The only mesa step that needs to be overcome in the later metalization is the initial etch trench in the EBL mesa. Therefore, there is no upper limit in etch time.

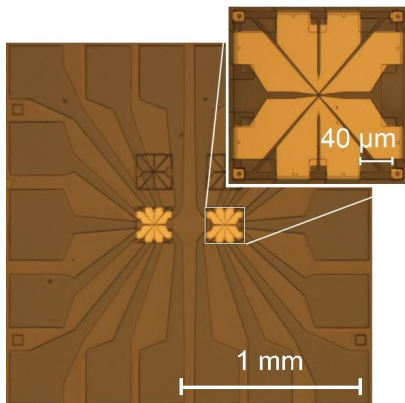


Figure 3.35: Micrograph of the EBL contact metalization. The sample is coated with double layer PMMA and the ohmic contacts on the two contacted EBL mesas are exposed and developed. The (Cd,Hg)Te cap layer is removed with ion milling prior to the contact metalization. The image is taken after the lift-off in acetone, the golden contacts reach $2\ \mu\text{m}$ close to the Hall bars.

The EBL contacts. The sample is spin-coated with the double layer PMMA resist. First *PMMA 600K 6 %*, then *PMMA 950K 4 %*, each applied at 7000 rpm for 40 s and baked out at 80°C for 10 min. A system of global and local alignment marks along the sides of the piece of wafer and the corners of the EBL write field, written in the EBL mesa step, ensures an accurate alignment [see zoom in Fig. 3.35]. The areas of the later ohmic contacts are exposed with an electron dose of $300\ \mu\text{mC}/\text{cm}^2$, at an extraction voltage of 30 kV, a working distance of 10 mm, a write field size of $204.8\ \mu\text{m}$, a magnification of 390 times and an SEM aperture of $20\ \mu\text{m}$. The exposed PMMA is then developed for 1 min 20 s in a solution of 1:1 *AR-656:IPA* and cleaned in H_2O . Around 750 nm thick, the lift-off mask is first used as an etch mask for the ion milling of the (Cd,Hg)Te cap layer of the wafer. With an etch rate of about 40 nm/min at 1 kV ion energy, 1 kV extraction voltage and 8 mA beam current the cap layer is reduced to 25 nm above the QW. Transferred in situ to the e-gun metalization chamber, 50 nm AuGe and 50 nm Au are deposited. A 30 min lift-off in 50°C hot acetone properly removes the metalization on the PMMA lift-off mask and reveals the ohmic contacts [see Fig. 3.35].

- This step is optional for samples on doped wafers with intrinsically conductive mesa leads to the Hall bar. However, potential fluctuations can occur in the later measurement at higher magnetic fields and elevated electron densities beneath the gate electrode of the Hall bar [see page 58].
- Proximity effects have to be considered in the design and dose distribution of the EBL exposure. With contacts close to the micro Hall bar, the single leads are close to each other and their dose distributions are influenced by neighboring exposure [75].
- PMMA is etched and cross-linked during the ion milling step of the (Cd,Hg)Te cap layer removal. Due to the thickness of the double layer PMMA, the mask can nevertheless be used as a lift-off mask in the subsequent metalization.
- The highly solvable bottom PMMA layer results in an undercut of the double layer lift-off mask. A parasitic metal deposition along the rims of the mask is thereby

avoided and, despite the previous ion milling, up to 300 nm metal can be deposited without any occurrence of sidewalls.

- The in-situ transfer from the ion milling to the metalization chamber avoids interface contamination and oxidation.
- The self aligned character of the consecutive ion milling and metalization ensures a perfect alignment of the metal contacts and the etched trenches [see and page 53].

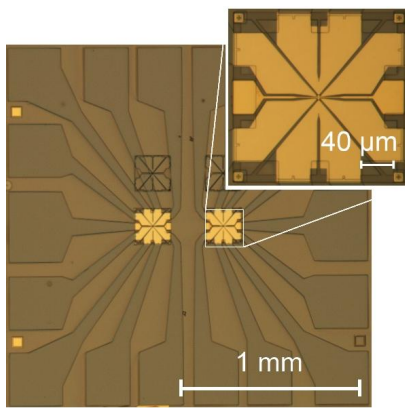


Figure 3.36: Micrograph of the structure with the gate electrodes. The golden squares on the left side arise from the optical alignment. The gate structure can be seen within the write field (zoom). After the MIBK PMMA residual removal the sample is coated in optical negative resist, the mask is aligned with the mesa, exposed and developed. ALD HfO_x is deposited prior to the metalization. The image is taken after the lift-off in Acetone.

The gate electrode. Prior to the insulator gate application, the sample is cleaned in 50 °C MIBK for several hours (over night). This removes the PMMA residuals remaining from the use as wet etch mask in the *EBL mesa* and the double layer PMMA lift-off mask in the *EBL contact* step.

Figure 3.36 shows the micrograph of the Hall bar after the gate application. Here, the gate is defined within the EBL write field using an optical process, but can alternatively be defined in an EBL process. Figure 3.37 shows a micrograph of the gates deposited by the two methods on a micro Hall bar. For better visibility, structures without the *EBL contact* step are shown. Both use one resist layer system to first deposit the novel low temperature ALD HfO_x and then self-align the Ti/Au gate metal:

(a) The EBL gate. A PMMA double layer is spin-coated, baked and exposed using the same parameters as in *EBL contacts* above. The development time of more than 1 min

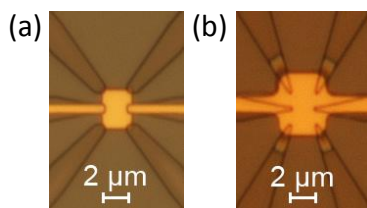


Figure 3.37: **(a)** EBL defined gate electrode on a Hall bar. The EBL alignment allows an accurate placement of almost any design. **(b)** Optically defined gate electrode. Its shape and alignment is limited by the application method.

20 s needs to be adopted to the full development of the small leads to the gate. The highly sensitive bottom PMMA is developed stronger, thus results in an undercut. 90 cycles of ALD grown HfO_x are deposited onto the sample at about 34°C and into the undercut. After each pulse of 20 ms for Hf and 50 ms for H_2O , the precursors are saturating for 10 s and the chamber is purged with Ar gas for 200 s. The 20 nm Ti and 100 nm Au are then e-gun evaporated on the sample and the lift-off is concluded in 50°C acetone.

- The EBL exposure allows to freely design any gate structure within the write field, accurately aligned down to a few nanometers.
- With only 50 nm undercut, thus 50 nm HfO_x overlap, gates of any kind can be realized within the EBL write field (compare to Fig. 2.5).

(b) The optical gate. *ARN 4340* is spin-coated at 6000 rpm for 20 s and baked at 80°C . In the mask aligner the optical gate mask is brought into contact with the resist surface and the gate structure is first aligned, then exposed for 20 s at 8 W. After a 6 min post exposure bake at 80°C the resist is developed for more than 45 s, adopted to development of the smallest leads. As for the EBL gates above, 90 cycles of ALD grown HfO_x are deposited at about 34°C onto the sample and into the undercut [see page 22]. 20 nm Ti and 100 nm Au are then e-gun evaporated on the sample and the lift-off is concluded in 50°C acetone.

- Easy to process.
- The alignment is less accurate as for EBL gates.
- The shape and size of the gate electrode is limited by the optical mask and exposure. Thus, the gate is bigger and rounded.
- In combination with EBL contacts below the gate, the symmetry is determined by the contacts.

The optical contacts. The sample is spin-coated with *ARN 4340* for 20 s at 6000 rpm and baked out 2 min at 80°C . In the mask aligner, the sample is brought in contact with the mask, aligned and exposed for 20 s at 8 W. The exposed resist cross-links in the 6 min and 80°C post exposure bake, the unexposed resist is then solved in a 45 s development in *AR 300-47* [see page 14]. A 10 s ion milling step at 1 kV acceleration voltage, 1 kV ion energy and 8 mA beam current removes possible residuals and increases the adhesion of metal layers. The sample is transferred in situ to the e-gun evaporation chamber, 50 nm AuGe and 100 nm Au are deposited. Figure 3.38 shows a micrograph of the sample after an acetone lift-off process of about 5 min in 50°C acetone. Cleaned in isopropanol and H_2O , the lithography process is finalized.

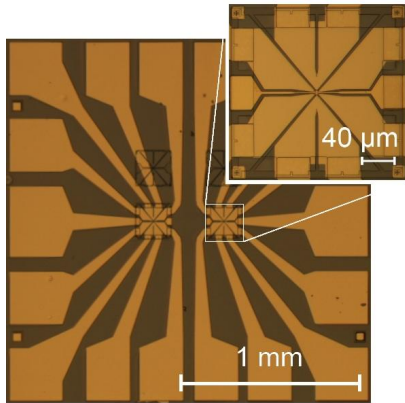


Figure 3.38: Micrograph of the optical contact metalization completing the sample lithography. Coated with optical negative resist, exposed and developed, the contact pads and leads are cleaned using ion milling and are subsequently metalized. The overlap into the EBL write field electrically connects the bond pads to the structure in the EBL write field (zoom).

- If the EBL contacts have previously not been defined in *The EBL contacts*, the ion milling step in *The optical contacts* is to be extended. The (Cd,Hg)Te cap layer is then etched to 20 nm above the HgTe QW prior to the metalization. The ohmic contacts to the QW are then only defined in the overlap to the EBL mesa within the write field.
- From the pads to the EBL mesa, solely the EBL defined etch trench needs to be overcome in the metalization to create contact to the mesa. Adopted to the mesa height, up to 500 nm of metal can be deposited with the *ARN 4340* process without the occurrence of sidewalls.

Part III

Quantum Spin Hall

Quantum Spin Hall Effect

More than 20 QSH samples have been measured for the development of *The Novel Micro Hall Bar Process*. A general increase in sample quality, mobility and cleanliness can be observed throughout the process development. Clear and undisturbed magneto transport measurements with no mobility loss are obtained in samples of few micro meter dimensions. However, only a few Hall bars exhibit a longitudinal resistance quantized to the resistance of two QSH edge channels $h/2e^2 = 12.906 \text{ k}\Omega$. Some Hall bars have obvious reasons, originating from lithography inhomogeneities and defects. Others are at the current state of lithography development and furthermore show no disturbances in the magneto transport data. Their determined maximum electron carrier mobilities μ_{max} can result in a mean free path λ_{mfp} exceeding the sample dimensions. Yet, not all samples show an accurate quantization in the QSH regime.

In the presence of fully ballistic edge channel transport, the resistances between contact pairs can be determined, counting the in and outgoing edge channels of all contacts [72]. The Landauer-Büttiker formalism allows to calculate the resistance between two contacts, using a system of linear equations connecting the currents into each contact to the potential in each contact via an $M \times M$ transmission matrix. M thereby represents the number of contacts and the matrix elements T_{ij} account for the edge channels leading from contact i to contact j with a quantized conductance of e^2/h each [92].

The schematic of a Hall bar in the presence of pure QSH edge channels and the corresponding Landau-Büttiker terminal configurations are pictured in Figure 1.1 (a) and (b). The standard Hall bar can be modelled with 6 terminals. When a small voltage is applied between contacts 1 and 4, the longitudinal resistance $R_{2,3}$ determines to $12.9 \text{ k}\Omega$. If, however, a backscattering center is introduced at any edge of the structure, the resistance changes.

Assuming full spin relaxation, the scattering center can be seen as an additional contact, effectively modifying the Hall bar into a 7 terminal configuration. Dependent on the location of the backscatterer – now a terminal – the quantization then calculates to 14.7 , 11.1 or $22.1 \text{ k}\Omega$ [see Fig. 1.1 (b)].

In a more realistic system without full spin relaxation, the backscattering event has a certain possibility. If the transmission matrix elements T_{ij} include the transmission probability of every channel, a modified 6-terminal configuration can describe an effective 7-terminal configuration. From no backscattering at all (6 terminals) to full contact properties in the scattering center (effectively 7 terminals). With only one backscatterer in

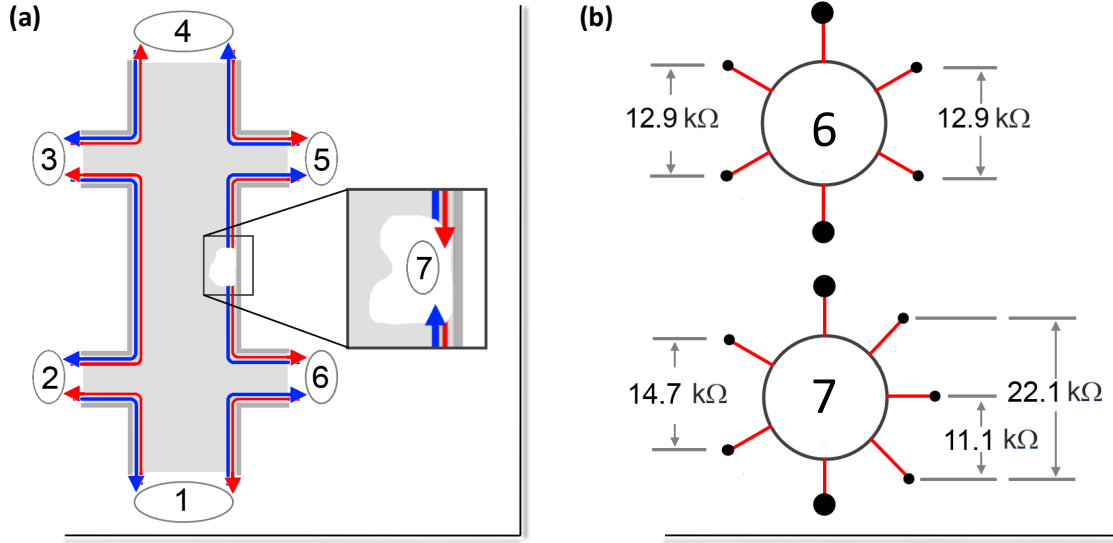


Figure 1.1: **(a)** 6-terminal configuration of a Hall Bar in the QSH phase. A puddle with full spin relaxation can be treated as a 7th contact in the Landauer-Büttiker formalism. **(b)** Resistance values for 6- and 7-terminal measurement in the Landauer-Büttiker formalism. The excitation voltage is applied on contacts with big dots, the voltages are probed on contacts with small black dots.

various locations, any value between 11.1 and 22.1 kΩ can be modelled for the longitudinal resistance.

In stronger disturbed systems with several backscatterers, the longitudinal resistance can therefore reach values below and far above the expected quantization. Only those with the least disturbances exhibit a QSH resistance close to 12.9 kΩ.

Figure 1.2 shows an overview of QSH samples fabricated and measured in the frame of this work. Their gap resistance does not accurately quantize to, but fluctuates around the expected value. Similar to universal conductance fluctuations (UCF) [73], their features within the QSH phase are fingerprints of the characteristic backscattering environment. Charge density and thereby the Fermi level in the systems are changed with gate voltage. In the gate sweep, the unique potential landscape is scanned and its backscattering results in characteristic features on the QSH signal. They are reproducible in sweep direction and distinct from sample to sample. Resembling in their R_{xx}^{top} and R_{xx}^{bottom} and comparable in both Hall bars on one sample, the features speak of wafer and fabrication related potential inhomogeneities:

Q2745 I, the very first measured wet etched micro Hall bar. Manufactured on a GaAs substrate and provided with a SiO₂-Si₃N₄ gate insulator, the features on the QSH signal shows abrupt jumps of a few kΩ. [comp. Fig. 1.2 **(a)**].

QC0167, fabricated in an early stage of development from an undoped QW on a

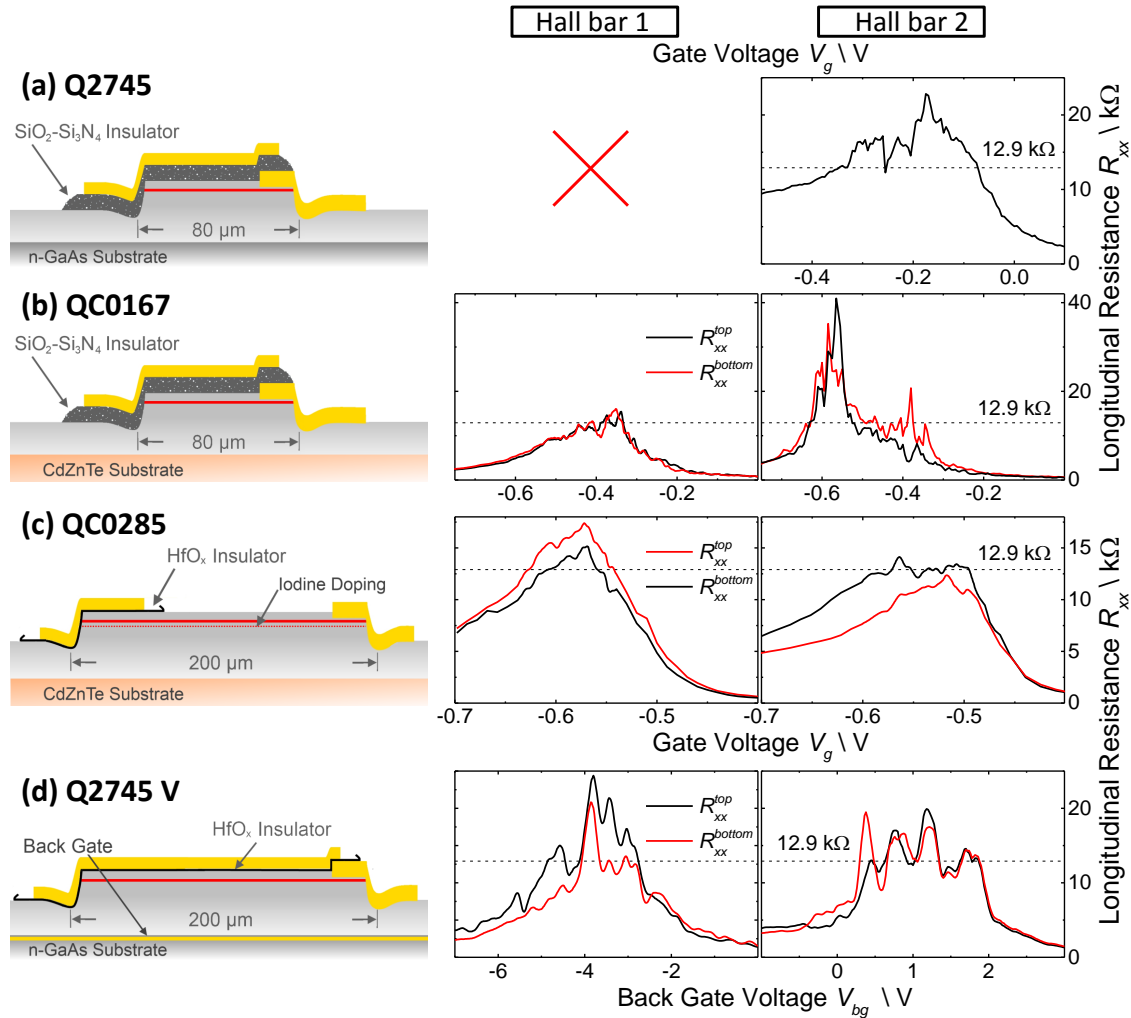


Figure 1.2: Schematics (left) and all QSHE measurements on both Hall bars in top and bottom configuration of R_{xx} as a function of gate voltage (right) on samples of different insulator systems, growth substrates, doping, write field sizes and contact distances, all measured at 4.2 K. (a) **Q2745 I**, QSH micro Hall bars fabricated on GaAs substrate, in a 80 μm write field, with close contacts, overlapping gate and $\text{SiO}_2\text{-Si}_3\text{N}_4$ insulator. Due to contact issues, only one R_{xx} is measured on Hall bar 2. (b) **QC0167**, QSH micro Hall bars of comparable design but on (Cd,Zn)Te substrate. (c) **QC0285**, QSH micro Hall bars on (Cd,Zn)Te substrate, in a 200 μm write field, with contacts far away, a iodine doping layer and HfO_x insulator. (d) **Q2745 V**, QSH micro Hall bars fabricated following the novel micro Hall bar process on conducting GaAs substrate additionally used as a back gate, with a HfO_x gate electrode overlapping the contacts close to the structure. The R_{xx} data is shown as a function of back gate voltage. On Hall bar 2, the top gate is floating, on Hall bar 1, a top gate voltage of $V_{tg} = 0 \text{ V}$ is applied.

(Cd,Zn)Te wafer also with an SiO₂-Si₃N₄ insulator, exhibits rather spiky features up to tens of kΩ [see Fig. 1.2 (b)].

QC0285, processed on a (Cd,Zn)Te substrate but with a doped QW, a HfO₂ ALD insulator and contacts far away from the gated structure. The features on the QSH signals are much smaller and smoother [see Fig. 1.2 (c)].

Q2745 V, built following *The Novel Hall Bar Process* on page 69 on a n-GaAs wafer with an undoped QW. Equipped with an HfO₂ top gate insulator, but measured with a substrate back gate and contacts close to the structure. The QSH signals show features with large oscillations of similar frequency and partly deviant amplitudes [see Fig. 1.2 (c)].

These are the first measured QSH signals of that quality. Since their discovery in 2007, the ion milling process related damages have made the observation of QSH signals a rare and non-reproducible event. The first to exhibit such rich and stable features, the QSH signals provide experimental results for the theoretical discussion on possible reasons for QSH backscattering.

In the QSH phase electrons of opposite spin counter-propagate along the mesa edge [see Fig 1.3 (a)]. Elastic backscattering induced by a single (nonmagnetic) impurity is suppressed by time-reversal symmetry [25, 24]. The QSH states require a spin flip or rotation, in order to scatter into the counter-propagating edge channel. Three main contributions are discussed to enhance backscattering. They all are a consequence from potential inhomogeneities in vicinity to the edge. Other than in bulk transport, the local potentials are not shielded by a large amount of charges in their surrounding. In absence of Debye-screening, the QSH states are left with a nearly unscreened potential landscape. Mobility and mean free path, obtained from magneto transport measurements in the bulk bands, do not account for the ballistic QSH states. A high carrier mobility can be related to a low amount of bulk scatterers and therefore indirectly reflect a homogeneous potential. Yet, the QSH effect is not necessarily measured in samples with the highest mobilities. Possible mechanisms for backscattering of the QSH edge channels and the origin of potential inhomogeneities are discussed, before temperature and magnetic field dependence of the QSH signals in QC0285 and Q2745 V are presented.

Kondo impurities. Despite their, on first sight nonmagnetic character, density inhomogeneities can have magnetic properties. As in a quantum dot, electrons can be trapped in small local potential pockets. If an odd number of electrons stabilizes through coulomb blockade, a magnetic impurity is formed. In vicinity to the edge, this can cause Kondo backscattering [see schematic in Fig. 1.3 (b)]. Electron and impurity spin are thereby both flipped and time reversal symmetry is preserved, even though the electron propagation direction is reversed [28, 79]. The distance to the edge, charging and discharging effects of the quantum dot as well as their coulomb blockade are relevant parameters.

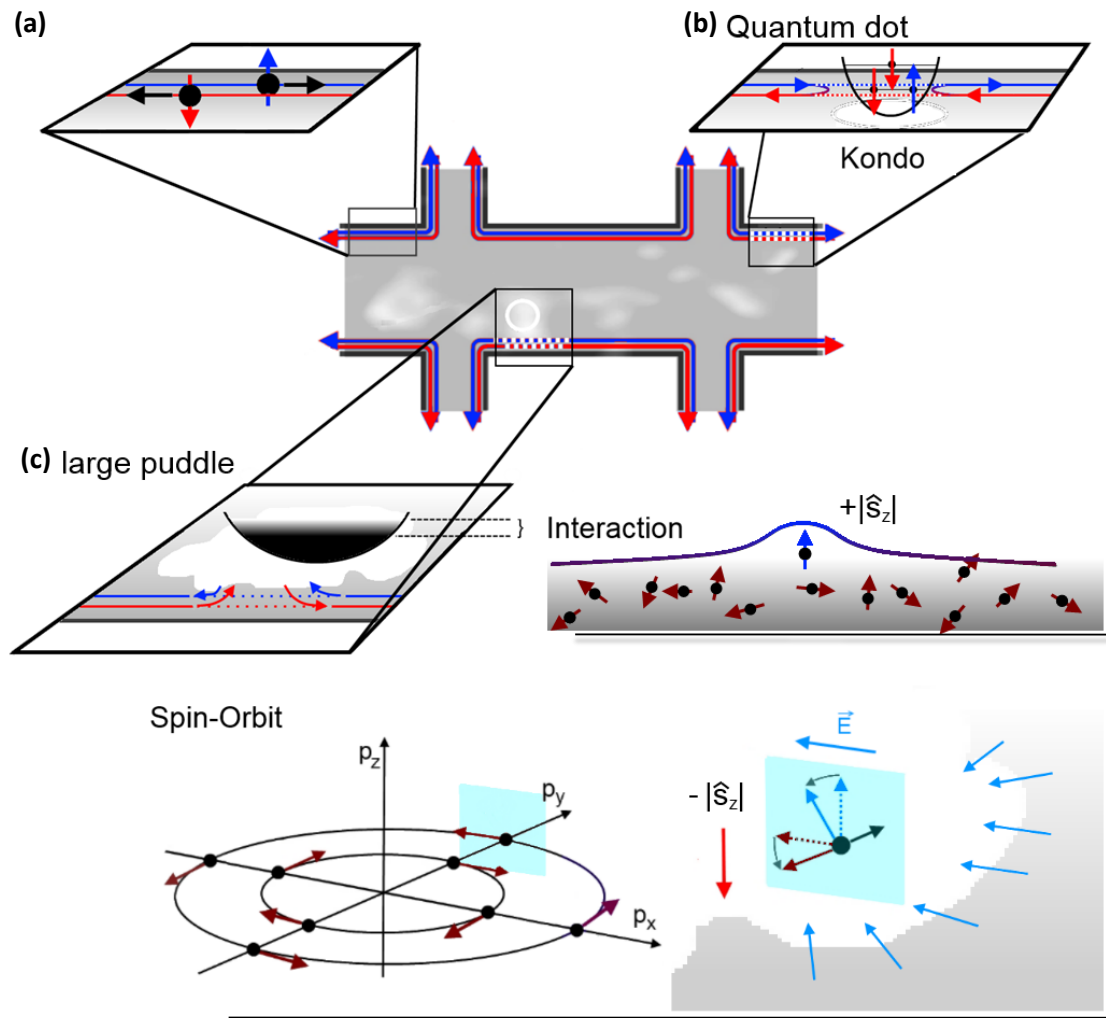


Figure 1.3: Schematic of the 6-terminal Hall bar in the QSH phase. Potential puddles are pictured as white spots. (a) The non-disturbed QSH channels counter-propagate along the edge of the mesa, carrying electrons of opposite spin. (b) Quantum dot-like puddle with an odd number of electrons have a magnetic moment. In vicinity to the edge this might lead to Kondo backscattering. (c) Electrons moving in a large puddle have two possibilities to change their spin: Interaction within the temperature broadened Fermi level randomize the electron spin. Rashba fields lead to a in plane spin polarization. An electron moving along the potential barrier of the puddle are forced to increase their out of plane spin magnetization due to Spin-momentum coupling. In both cases electrons can tunnel from the QSH state into the puddle (blue arrow), change their spin and tunnel into the counter-propagating QSH channel (red arrow).

Interactions. In large potential inhomogeneities, bulk carriers can create charge puddles. Close to the edge, a spin polarized QSH state can tunnel into the metallic bulk states of a puddle. At finite temperature, the Boltzmann broadening of the Fermi level enables inelastic interactions, spin is not conserved. The larger the dwelling time of the electron, the more likely electrons interact with each other. Their spin randomizes and electrons can tunnel into the counter-propagating QSH states [27] [see schematic in Fig. 1.3 (c)]. The interaction is thereby strongly related to the density of states within the puddle. The more populated, the stronger interaction and backscattering.

Rashba spin-orbit coupling. Bulk charges moving through an asymmetric perpendicular potential experience an effective magnetic field perpendicular to their momentum and the electric field [80]. This also accounts for electrons within charge puddles. The potential asymmetry is given by the asymmetric boundary conditions of the QW and can be reinforced by the insulator-gate electrode on the Hall-bar. The band inversion of the HgTe QW leads to $|p\rangle$ -symmetric electrons in the conduction band and therefore to a large Rashba-split energy:

$$E_{|p\rangle\text{-type}}^{SO} \propto \pm \langle \beta E_z \rangle k_{\parallel}^3.$$

The energy shift of opposed in-plane spin directions in the energy dispersion is directly proportional to the Rashba-coefficient β but in cubic ($|p\rangle$ -type) and not linear dependency ($|s\rangle$ -type) to the in-plane momentum k_{\parallel} [84, 85, 43]. The spin-orbit interaction results in an in-plane spin-momentum coupling.

Electrons moving along the potential edge of the puddle increase their out of plane spin component [see Spin-Orbit in Fig. 1.3]. To a certain probability, electrons can tunnel from a QSH state into a charge puddle close to the edge. Moving within the puddle, their spin is rotated according to their spin-momentum coupling and can tunnel back into the counter-propagating edge channel [81, 27, 82, 83]. Dependent on the strength of spin momentum coupling, the Rashba backscattering in thin QWs should be different for conduction and valence band puddles. The cubic proportionality does account for the $|p\rangle$ symmetric conduction band (H1). But the E1 valence band, below about 8 nm QW thickness, is $|s\rangle$ symmetric and therefore only exhibits a linear Rashba splitting.

The backscattering is strongly related to location and density of inhomogeneities as well as strength of interactions. Puddle distribution and density thereby change with gate voltage as much as their size, density of states and occupation. In the complex interplay with effective field and temperature dependent Coulomb blockade, tunneling probability and spin dephasing, the theories mostly assume a constant gate voltage. Many propose the temperature dependency of the conductance as an experimental approach; predicting a decrease in $G = G_0 - \Delta G$, a temperature power law dependence of $\Delta G \propto T^\alpha$ and a broad variation of α . Only [28], considering Kondo impurities, predicts an increase in conductance towards higher T and a recovery of the ideal $2e^2/h$ for $T \rightarrow 0$ K (regime of

strong coulomb interaction). The temperature dependence of the QSH signals in QC0285 and Q2745 V are presented on page 85 and 91.

With the potential inhomogeneities as the common origin of backscattering, the process optimizations in *Development* appear crucial for a stable QSH. An overview on possible reasons for irregularities in the potential landscape is given:

Figure 1.4 (a) schematically pictures a number of reasons for potential inhomogeneities within the QSH structure and (b) their consequence on the band gap of the inverted QW. H_1 and E_1 are the ground states of the conduction (blue) and the valence band (red). At the edge of the mesa they adopt to the trivial band ordering leading to the QSH edge channels. Inhomogeneities cause a disturbed potential landscape and, if close to the edge, cause backscattering within the QSH phase. Above the Fermi level E_F all states are empty, below E_F all states are occupied. Charge puddles occur in the presence of disturbances such as:

- **I. Trap states.** Dangling bonds in the insulator system, at the mesa insulator-interface and within the crystal structure lead to trap states. At sufficient gate voltages they are charged and discharged during the gate scan. Shielding the gate influence onto the QW structure, the local potential is influenced. The puddle size

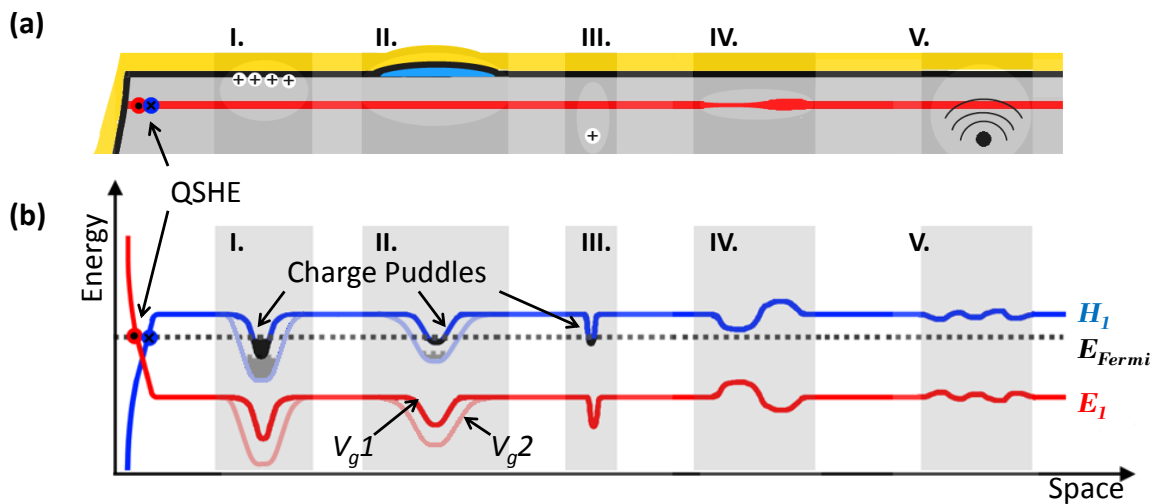


Figure 1.4: Schematic of I. trap states, II. residuals, III. donors, IV. thickness fluctuations and V. growth defects in the gated QW structure in (a) and their influence onto the potential landscape at two different gate voltages in (b). Potentials from trap states and residuals between QW and gate electrode are both populated and modified by the gate voltage. In vicinity to the edge, puddles can cause QSH backscattering.

thereby strongly depends on the applied gate voltage. In the presence of trap states, gate hysteresis is likely to occur.

- **II. Residuals.** Process residuals on the mesa surface cannot only be a source of trap states, but also result in a varying distance from gate electrode to QW. As the gate influence differs locally, the potential landscape does likewise. Once more, the size of the inhomogeneity is gate voltage dependent.
- **III. Charge impurities.** In doped QW structures, the dopant releases one electron and the charged donors remain in the doping layer. Separated from the QW by a 70 nm (Cd,Hg)Te spacer, the resulting potential in the QW is smooth. If, however, unintentional, isolated and close to the QW, doping can lead to a localized potential inhomogeneity. Growth defects such as Hg vacancies (p-doping) can additionally contribute to (negative) charged potentials.
- **V. Thickness fluctuations.** The energy gap in the QW is given by E_1 and H_1 and changes with the QW confinement. A variation of 1-2 atomic mono layers in the QW thickness (3-6 Å) results in a gap fluctuation of ΔE_{Gap} up to 5 meV [86]. With a maximum inverted band gap of around $E_G \approx 22$ meV, this is a major contribution to an effectively reduced band gap and a possible source for density puddles.
- **IV. Growth defects.** During the MBE growth of the material, a variety of defects can be built into the lattice. Reasons for this are: a non-perfect substrate morphology, lattice mismatch induced strain in the layer growth and contamination. They lead to structural imperfections, dangling bonds, local growth ratio variations, dislocations and vacancies and influence the potential accordingly. Various potential deformations can occur in the periphery of large growth irregularities. As intrinsic defects they are independent from lithography. When visible in the optical microscope, they can be avoided in the placement of the write fields.

Some MBE grown wafers exhibit a high visible defect density. The quality of the magneto resistance measurements and the obtained carrier mobilities from the macroscopic characterization Hall bars help to select suitable material with the least inhomogeneities. The morphology of the (Cd,Hg)Te surface can be judged with a microscope. Figure 1.5 shows the images of the HgTe QW wafers QC0285 and Q2745 grown on (Cd,Zn)Te **(a)** and n-GaAs substrates **(b)**. Whereas the (Cd,Zn)Te wafer is littered with roundish defects of a few hundred nm in lateral dimensions, the n-GaAs wafer features a rough but washed out surface with elevations up to 1 μ m lateral size. As long as the QW follows the up to 4 nm high elevations, the effects on the potentials are minor.

The growth defect difference can be explained by the distinct lattice mismatches from the substrate to a CdTe buffer, grown prior to the (Cd,Hg)Te/HgTe QW layers. With a strain of only $\approx 0.3\%$, CdTe grows nearly lattice matched on the (Cd,Zn)Te substrate. On n-GaAs, however, a lattice mismatch of $\approx 14.7\%$ only allows a fully relaxed growth of the CdTe buffer. The different start conditions might be a reason for the different

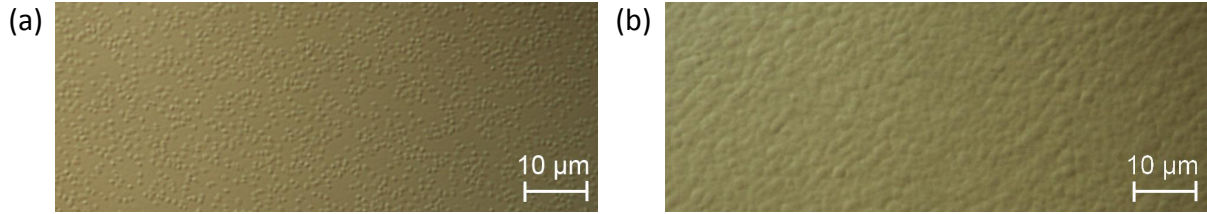


Figure 1.5: Micrograph of the wafers QC0285 on (Cd,Zn)Te substrate **(a)** and Q2745 on n-GaAs substrate **(b)**.

morphology.

Despite the surface roughness, the gap conductance in Hall bars of both wafer types quantize to the $2e^2/h$ of the QSH edge channels [see Fig. 1.2]. Thus, the surface inhomogeneities of such wafers do not seem to disable proper QSH measurements. For a detailed description of the MBE growth of the wafers see [77, 87].

The n-GaAs has two advantages over the 10×10 mm sized (Cd,Hg)Te substrate:

First, up to 35 sample pieces can be cleaved from the 1/4 of a 2" wafer. This allows to optimize sample design and process details in reproducible lithography tests. Furthermore, it enables series of measurements that would not be covered with the nine pieces grown on a (Cd,Zn)Te substrate.

Second, the n-GaAs can be used as a back gate when the substrate is contacted to the chip carrier via conductive silver glue.

Below, two QSH samples on both wafer types are presented in further detail. Temperature and magnetic field dependence of the QSH signal in QC0285 and Q2745 V are discussed. Top and back gate performance are compared on Q2745 V, equipped with a contacted n-GaAs substrate.

1.1 Temperature and Magnetic Field Dependence

QC0285 is grown on a (Cd,Zn)Te substrate. Doped via an MBE grown I:(Cd,Hg)Te bottom layer 70 nm below the QW, the contact leads to the structure are intrinsically conducting. The Hall bars are only contacted in the overlap to the optical leads. The dimensions of the optical HfO₂ insulator gate electrode thereby determine the length of required edge conductance for a quantized QSH to about 12 μm [see Fig 3.24 on page 56].

Temperature Dependence. Figure 1.6 shows the longitudinal resistances of both Hall bars on QC0285 for different temperatures in top and bottom measurement configurations plotted against top gate voltage on the left. To observe the maximum of the gap resistance, the gate voltage range is extended at higher temperatures. Their (average) gap resistance as a function of temperature is given on the right. The values for the gap resistances are averaged over the plateau width or taken from the clear maximum value.

Hall bar 1 in Figure 1.6 exhibits a uniform temperature dependence for the top **(a)** and bottom edge of the Hall bar **(b)**. Similar in both, their longitudinal resistance at 2.4 K (black) shows minor fluctuations and a peaked – not a plateau-like – resistance in the energy gap [$-0.55 \text{ V} < V_g < -0.4 \text{ V}$]. With increasing temperature, the maximum gap resistances decrease from more than 16 kΩ at 2.4 K (black) down to a minima below the 12.9 kΩ at 35 K (red). Towards even higher temperatures, the peak in resistance slightly increases again while its position is shifting in gate voltage and sweep direction to more negative V_g . With more and more charged trap states between gate electrode and QW available at increasing temperature, the down gate sweeps are increasingly hysteretic to their back sweeps (not shown). Effectively shielding the influence, the gap maximum is found towards more negative gate values and the peak width broadens.

In **Hall bar 2**, the resistances along the top **(c)** and bottom mesa edge **(d)** are different. At 2.4 K, R_{xx}^{top} (black) remains below 12.9 kΩ, whereas R_{xx}^{bottom} (black) quantizes in a QSH plateau from $V_g = -0.35 \text{ V}$ to -0.42 V [see Fig. 1.6].

Both **(c)** and **(d)** resemble each other in their shift of peak position with increasing gate hysteresis. Other than in Hall bar 1, their (average) gap resistances exhibit a distinct temperature dependency. Whereas R_{Gap}^{top} in **(c)** shows no clear dependence, R_{Gap}^{bottom} in **(d)** remains quantized up to 11 K and then increases linear in the log-log scale with R_{Gap} proportional to $T^{1/4}$.

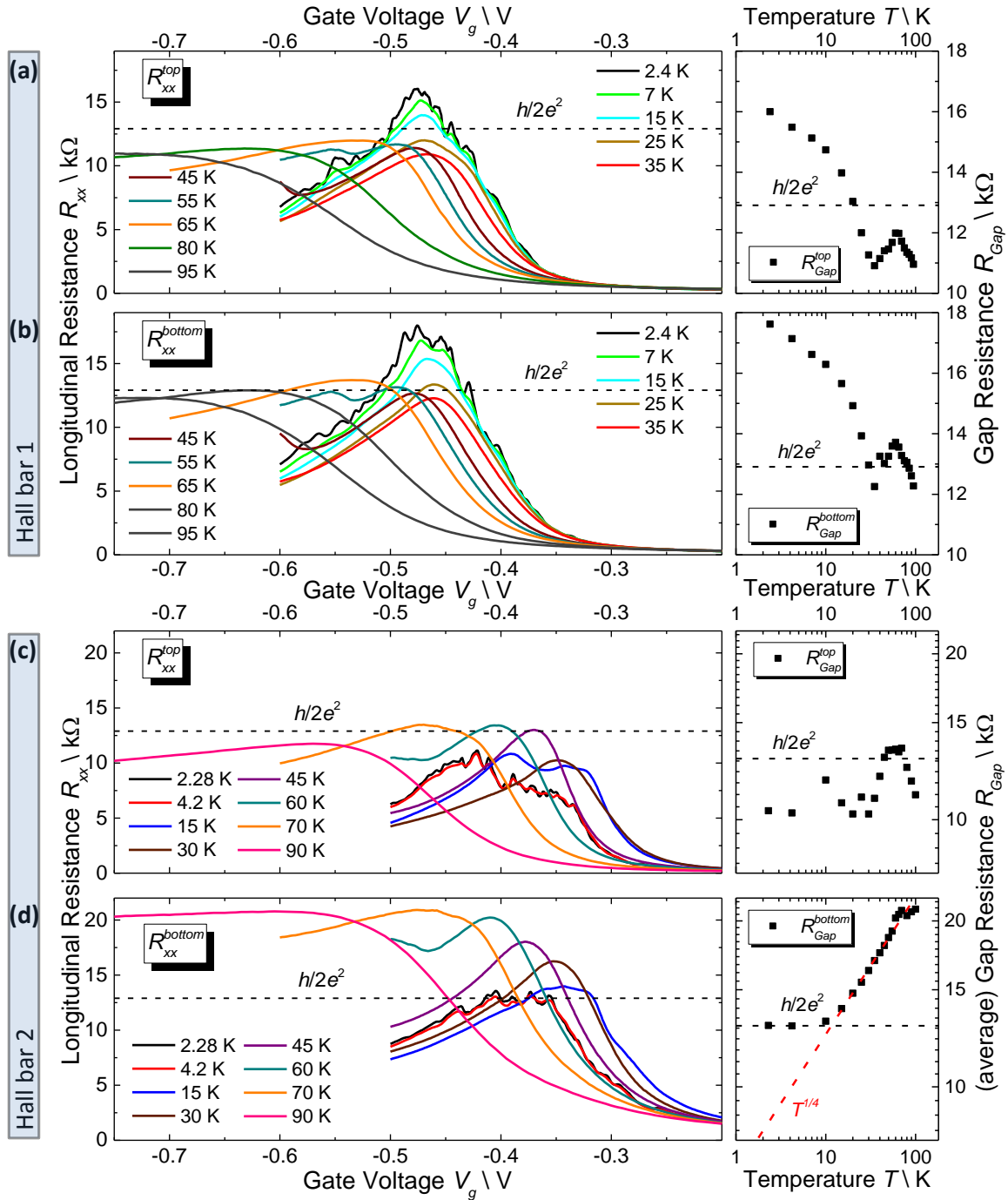


Figure 1.6: **QC0285**. Longitudinal resistance as a function of (top) gate voltage for different temperatures in the top (a) and bottom configuration (b) of Hall bar 1 and the top (c) and bottom configuration (d) of Hall bar 2 on the left and their (average) gap resistance plotted against the temperature in log-log scale on the right. The gate voltage is swept from low to high negative voltage and the range is chosen to be large enough to observe the resistance decrease to the p-conducting regime.

In the interplay of temperature and applied gate voltage, the position and amplitude of R_{Gap}^{max} is a superposition of a number of effects.

Gate hysteresis. At increasing temperature, more trap states within the QW surrounding can be occupied by charges. The potentials from the applied gate voltages further enhance a charging and discharging of the trap states. This reduces the effectiveness of the gate electrode, broadens the peak of the gap resistance and shifts its position towards higher gate voltages.

Potential landscape modification. Shielding the gate influence, the localized trap states result in local potential variations. As for lithography residuals between the gate and QW, they are both populated and modified by the gate voltage. Complementing the local intrinsic potentials arising from donors, growth defects and thickness as well as concentration variations within the crystal [see Fig. 1.4].

Backscattering. According to the gate voltage, the carrier density in the system is altered. The potential inhomogeneities are populated and charge puddles created. Size as well as puddle density are strongly dependent on V_g . With temperature, the carrier localization broadens and charges can tunnel more easily back and forth from QSH channels into puddles near by. Backscattering is enhanced and the gap resistance increases. In case of a high puddle density, inter-puddle hopping can furthermore cause parallel conductivity, leading to a decrease in resistance.

Magnetic Field Dependence. Figure 1.7 (a) shows a color plot of the longitudinal resistance as a function of gate voltage and magnetic field. The n -conducting regime is depicted towards lower negative gate voltages, the p -conductive side towards high negative V_g . The elevated resistance around $V_g = -0.5$ V corresponds to the energy gap. Below a magnetic field of about 4 T, the gap resistance remains in the order of tens of k Ω (green to yellow). Above 4 T, the values increase to hundreds of k Ω (red) and the conduction in the energy gap is strongly suppressed.

This is consistent with results from 8 band k -p calculations of the Landau-level energy dispersion [88]. Landau quantization in magnetic field reverses the band inversion above a critical field B_c and a trivial band gap opens up [see Figure 1.7 (b)]. Below B_c , the QW remains in the QSH, above in the trivial phase. Calculated to 3.9 T for the 7.5 nm thick QC0285 QW [see (c)], the transition from QSH to trivial phase corresponds to the two resistance regimes in the gap resistance measured in increasing magnetic field [see (a)].

In magnetic fields the time-reversal symmetry is broken. An energy is forming at the linear crossing of the Dirac-like surface state dispersion [13, 89, 90]. Small enough to not fully gap the surface states at 4.2 K, edge states remain. Backscattering, however, is enabled as the spin states around the gap are mixed and time-reversal symmetry is broken. In addition to that, the puddle related backscattering adds another dimension to the characteristic fingerprint of the potential background in gate voltage. Tunnel probabilities and spin

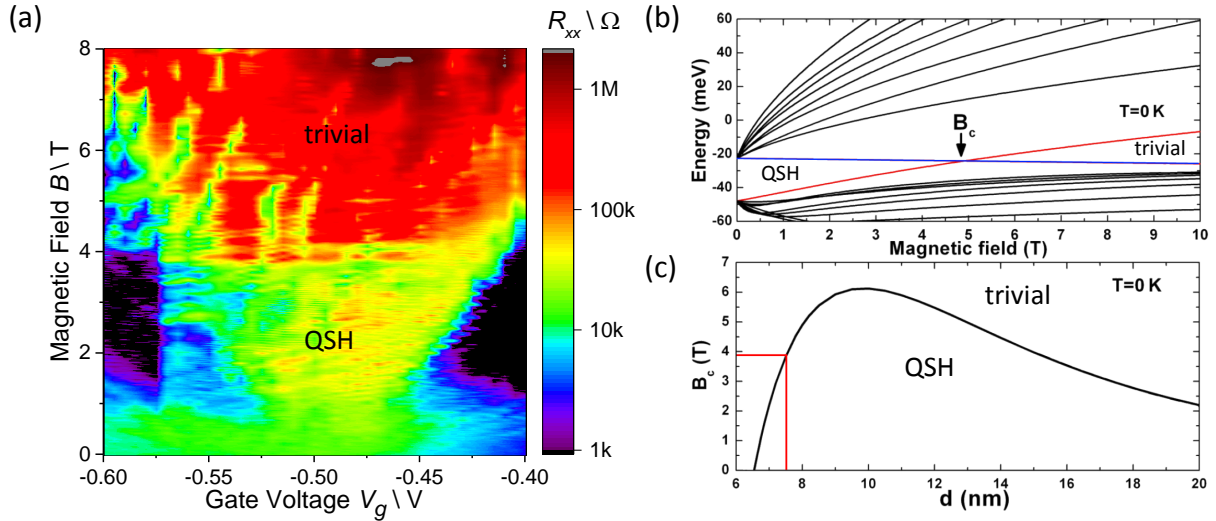


Figure 1.7: **QC0285.** (a) Longitudinal resistance R_{xx} plotted in color against swept gate voltage and stepped magnetic field. (b) Landau levels calculated for a 8 nm HgTe QW in dependency of the magnetic field. The inversion of the lowest Landau levels (blue and red) is reversed above a critical magnetic field B_c . (c) B_c as a function of QW thickness. (b) and (c) are taken and modified from [88].

dephasing mechanisms change with increasing magnetic field. Landau quantization in charge puddles leads to QH edge states and a continuous variation of density. Once more, the complex correlation of parameters does not allow to conclude on any dominant mechanism. Yet, it is remarkable, that the gap resistance appears to remain QSH edge channel dominated up to $B_c = 3.9$ T, as the conductance breaks down above the predicted band inversion lifting.

Q2745 V is grown on a n-GaAs substrate. Fabricated following *The Novel Micro Hall Bar Process*, the state of the art sample is equipped with optical HfO₂ insulator top gate electrodes. They overlap the EBL contacts, in 1 μm distance to the structures. To quantize in the longitudinal resistance, the QSH channels have to propagate about 7 μm along the mesa edge on the left or right side [see Fig. 1.8 (a) and (b)]. The contact lead to the top gate of Hall bar 2 lost contact in the metalization process. Therefore, its top gate potential is floating at all times. Other than QC0285, the conductive growth substrate is contacted and can be used as an integral back gate. It appears to have a different influence onto the potential.

Figure 1.9 shows the longitudinal resistance of both Hall bars as a function of their gate voltages, numbered I to IV following their measurement chronology:

(a), **top gate measurements on Hall bar 1.** The top (red) and bottom R_{xx} (black) [I] are measured directly after the cool down to 4.2 K. They are opposed to re-measurements of the very same configurations (IV), obtained after about 22 B-field sweeps to ± 8 T and 40 back gate sweeps to ± 6 V conducted for measurements on the other Hall bar. The gap resistances of (I) are lower than expected for a quantized Spin Hall conductance, whereas those of [IV] are much closer to $h/2e^2$.

In [77], the repetitive gate sweeps of SiO₂-Si₃N₄ insulator gate electrodes on macroscopic structures have led to a smoothed potential and a resistances decrease closer to quantization. Neutralized charge impurities are accounted responsible for this effect. Therefore, it is most likely, that the repetitive back gate sweeps in between (I) and (IV) have also lead to a change in the potential landscape.

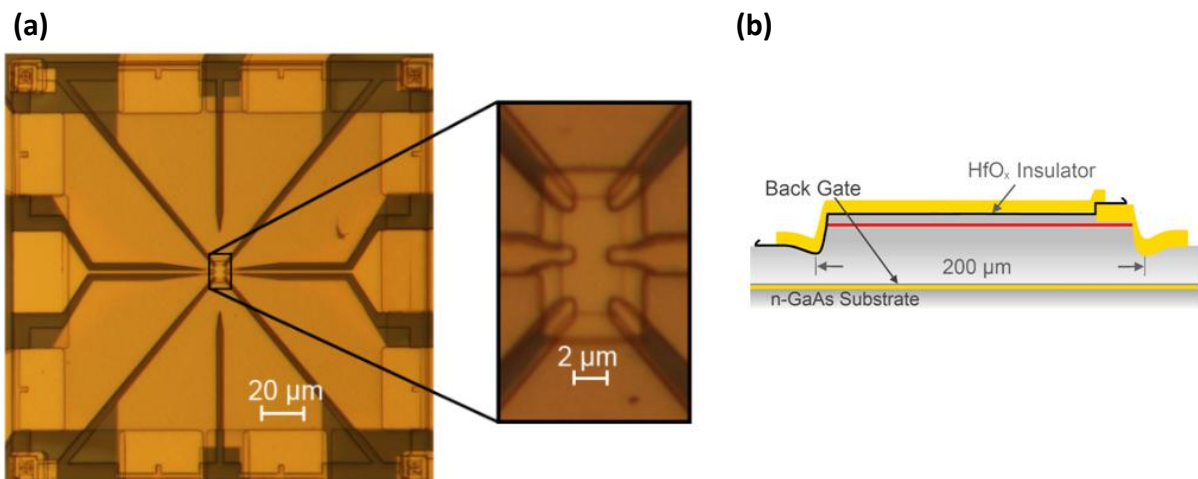


Figure 1.8: **Q2745 V.** (a) Micrograph of the EBL write field and (b) sample schematic. The zoom onto the Hall bar shows the HfO_x insulator gate electrode overlapping the EBL contacts reaching 1 μm close to the Hall bar.

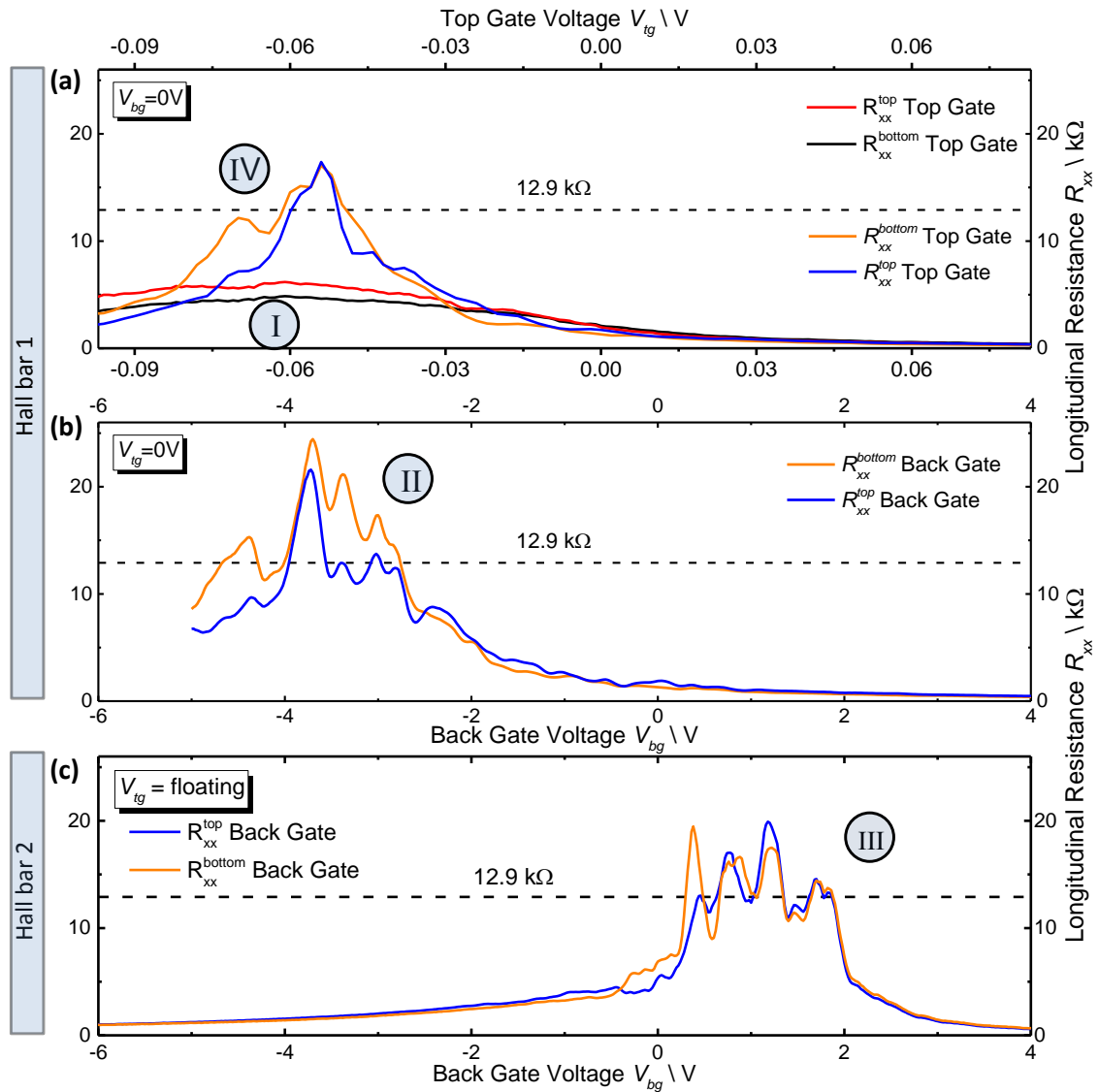


Figure 1.9: **Q2745 V.** Longitudinal resistance as functions of gate voltage at 4.2 K. (a) with the top gate and (b) with the back gate on Hall bar 1 as well as (c) on Hall bar 2. I, II, III and IV order the measurements in their timeline. In between the first top gate sweep I and a later IV the passive Hall bar 1 has experienced about 40 back gate sweeps to ± 6 V and 22 magnetic field sweeps to ± 8 T.

(b), **back gate sweep on Hall bar 1.** Assuming that, the back (II) and the top gate sweep (IV) are both obtained in a stable potential configuration, one can compare the gate performance. The gap resistances show a similar progression but more detailed features on the back gated top (blue) and bottom R_{xx} (orange) (II). The features equally appear in both measurement configurations. They do not have the same amplitude but evolve at the same gate voltage values.

With the substrate as back gate, the resulting potential is different to the top gate poten-

tial. Here, either the top gate electrode results in a more washed out potential, smoothening the features. Or, the MBE grown insulator leads to specific disturbances responsible for the features in first place. Considering the material and interface quality between the gates and the QW, both appears possible. The top gate influence is screened and inhomogeneous due to the surface oxide, possible lithography residuals, thereby introduced trap states and a non perfect insulator morphology. Other than that, the back gate potential is only disturbed by minor defects occurring in the MBE growth of the (Cd,Hg)Te/HgTe QW layer stack under UHV conditions, but might introduce specific potential disturbances. As the first back gated micro Hall bar with quantization, neither of both can be ruled out. More data is required.

(c), back gate sweep on Hall bar 2. The top gate is on a floating potential, as no gate voltage can be applied to the top gate. The features in the QSH resistance (III) are similarly pronounced as in (II) on Hall bar 1. The dips and peaks in the top (blue) and bottom configuration (orange) appear at the same back gate voltage. The QSH edge channels on both sides of the 2 μm distant Hall bar edges are equally influenced. Top and bottom R_{xx} of Hall bar 2 even reproduce each other on the n-conducting side of the energy gap at $V_{bg} = 2\text{ V}$. A slight deviation in the fluctuation amplitude can be observed towards the p -conducting side. They seem to be connected to the pure QSH regime, as they neither appear when the Hall bar is p (below $V_{bg} = 0.2\text{ V}$), nor when it is n conducting (above $V_{bg} = 2\text{ V}$).

The origin of the fluctuations remain unclear. More characteristics can be obtained from the temperature and magnetic field dependence of the QSH signals presented below.

Temperature Dependence. Figure 1.10 show the longitudinal resistances of Hall bar 2 on Q2745 V for different temperatures T in top **(a)** and bottom configuration **(b)** as a function of back gate voltage V_{bg} on the left. On the right, their (averaged) gap resistance are given, plotted against the temperature in log-log scale. Both R_{Gap} along the 2 μm distant sample edges exhibit a similar temperature dependence. Three regimes characterize the T -dependence of their QSH edge channel resistance.

Up to 11 K ($2k_bT = 1.9\text{ meV}$), the resistances remain quantized and the features on the QSH plateaus are well pronounced.

From 11 to 32.8 K, the gap resistances increase in quadratic dependence, $R_{Gap} \propto T^2$. The features remain distinguishable up to $T = 23.4\text{ K}$ (olive), before the gap resistances reach their maxima at $T = 32.8\text{ K}$ (ruby).

Above 32.8 K, the maxima peak positions decrease again with increasing temper-

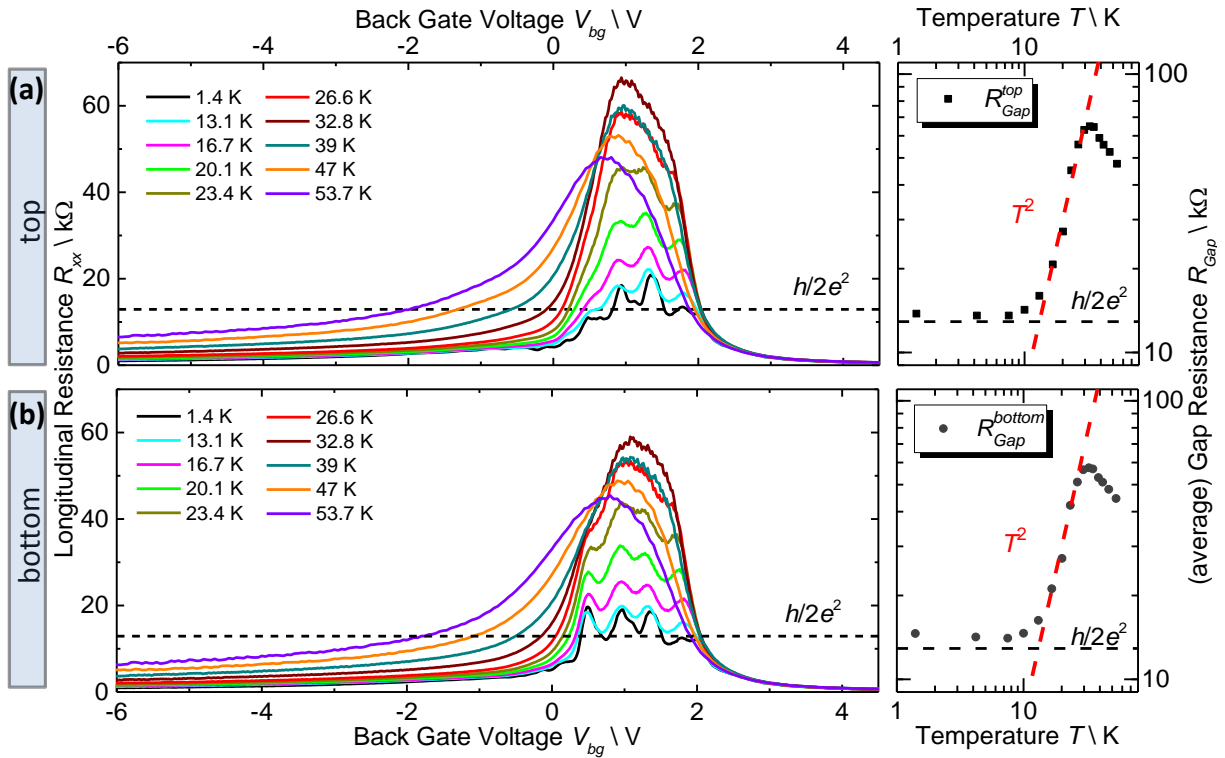


Figure 1.10: **Q2745 V**. Longitudinal resistance of Hall bar 2 as a function of back gate voltage for different temperatures in the top (a) and bottom configuration (b) on the left and their (average) gap resistance plotted against the temperature in log-log scale on the right.

ature, linear on a log-log scale. The maxima slightly shift towards smaller back gate voltages. The broadening of the resistance peaks and the increase in the resistance on the p -conducting side for negative V_{bg} is once more related to temperature accessible trap states effectively reducing the gate influence. Within the MBE grown CdTe/(Cd,Hg)Te layer between QW and substrate, they shield the back gate influence.

The clear $T(R_{max})$ in the gap resistance of Q2745 in Figure 1.10 (right) corresponds to an estimated Fermi-level broadening of $2k_bT = 5.6$ meV. The 7.5 nm QW thickness calculates to an energy gap of 15.6 meV for $T = 30$ K (8-band $k \cdot p$) [77]. With an approximated temperature broadening of 1/3 of the band gap, it seems likely, that electrons can reach the conduction band within the Boltzmann tail. Inter band excitation, therefore, appears plausible as origin for the resistance decrease.

Proportional to T^2 , the temperature dependence in both measurement configurations might indicate the contribution of one or several dominant backscattering effects. However, neither the power law dependence of this, nor the $\alpha = 1/4$ in QC0285 does match with any of those currently discussed in the theoretical community.

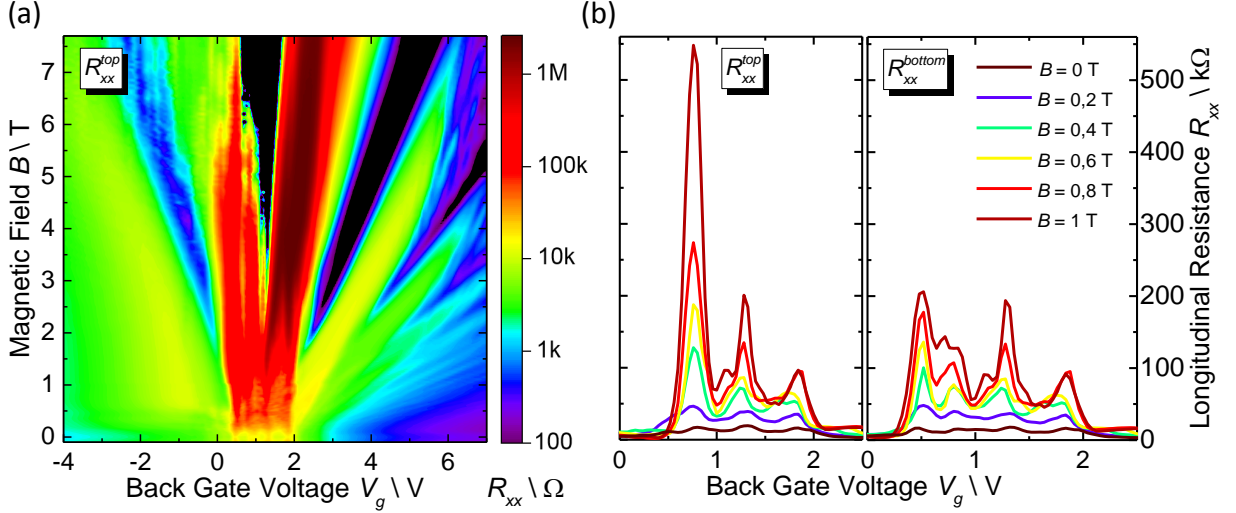


Figure 1.11: **Q2745 V.** (a) Longitudinal resistance R_{xx} plotted in color against stepped magnetic field and swept back gate voltage. (b) R_{xx} as a function of back gate voltage for different magnetic fields.

Q2745 V - magnetic field dependence. Q2745 V does not exhibit the same magnetic field dependency of the gap resistance as QC0285 [see. Fig 1.7 (a)]. Figure 1.11 (a) shows R_{xx}^{top} plotted in color against magnetic field and back gate voltage. Measured in a wide voltage and thereby density range, the position of the Landau-levels in the n - (above $V_{bg} = 2$ V) and the p -conducting regime (below $V_{bg} = -2$ V) can be determined as an increase in resistance. Despite an expected critical magnetic field of $B_c = 5.8$ T (8 nm QW), the gap resistance increases to above one hundred k Ω already at 0.35 T. The QSH conductance is strongly suppressed, even though the bands remain inverted.

Single back gate scans at different magnetic fields in Figure 1.11 (b) show that the increase in gap resistance mainly originates from an increase of the fluctuations on the QSH signal. The features towards the n -conducting regime at $V_{bg} = 1.8$ V stop increasing above 0.8 T and have the same progression in top and bottom measurement configuration. Other than that, the feature towards the p -conducting regime at $V_{bg} = 0.8$ V continue increasing and are clearly different. R_{xx}^{top} reaches a feature peak value, 300 k Ω higher than R_{xx}^{bottom} . If charge puddles are the origin of that difference, the disturbance most likely arises from the p -conducting valence band and might be located closer to the top edge of the Hall bar. A change in the peak position cannot be observed. Thus, Fabry-Pérot modes within a closed loop and magnetic field dependent phase can be excluded as origin for the fluctuations.

The two samples do not allow a conclusive statement on the origin of the backscattering in QSH edge channels. However, their different temperature and magnetic field dependencies

indicate two distinct mechanisms. Whilst the backscattering of the edge channels in QC0285 increases with $R_{Gap} \propto T^{1/4}$ and the gap resistance remains QSH dominated up to B_c , Q2745 V follows $R_{Gap} \propto T^2$, but the QSH conductance is suppressed at fields far below its critical magnetic field predicted for the band inversion lifting.

The results emphasize the necessity of both, temperature and magnetic field dependence for the characterization of possible backscattering mechanisms [91]. Thereby, it must be considered that the magnetic field does not only brake time-reversal symmetry, but also changes density of states within puddles, as the QHE sets in. Further statistics is required.

1.2 Nonlocal Resistance

When current path and voltage probe do not have any overlap, the resistance is nonlocal. In a purely diffusive regime the nonlocal resistance is zero. In the presence of ballistic edge channels, potentials are carried along the edge of the sample charging neighboring contacts and a resistance can be measured dislocated from the excitation. The presence of nonlocal signal is a prove for ballistic edge channel transport [15]. The expected resistance values for a 6-terminal device are calculated using the Landauer-Büttiker formalism [see page 76].

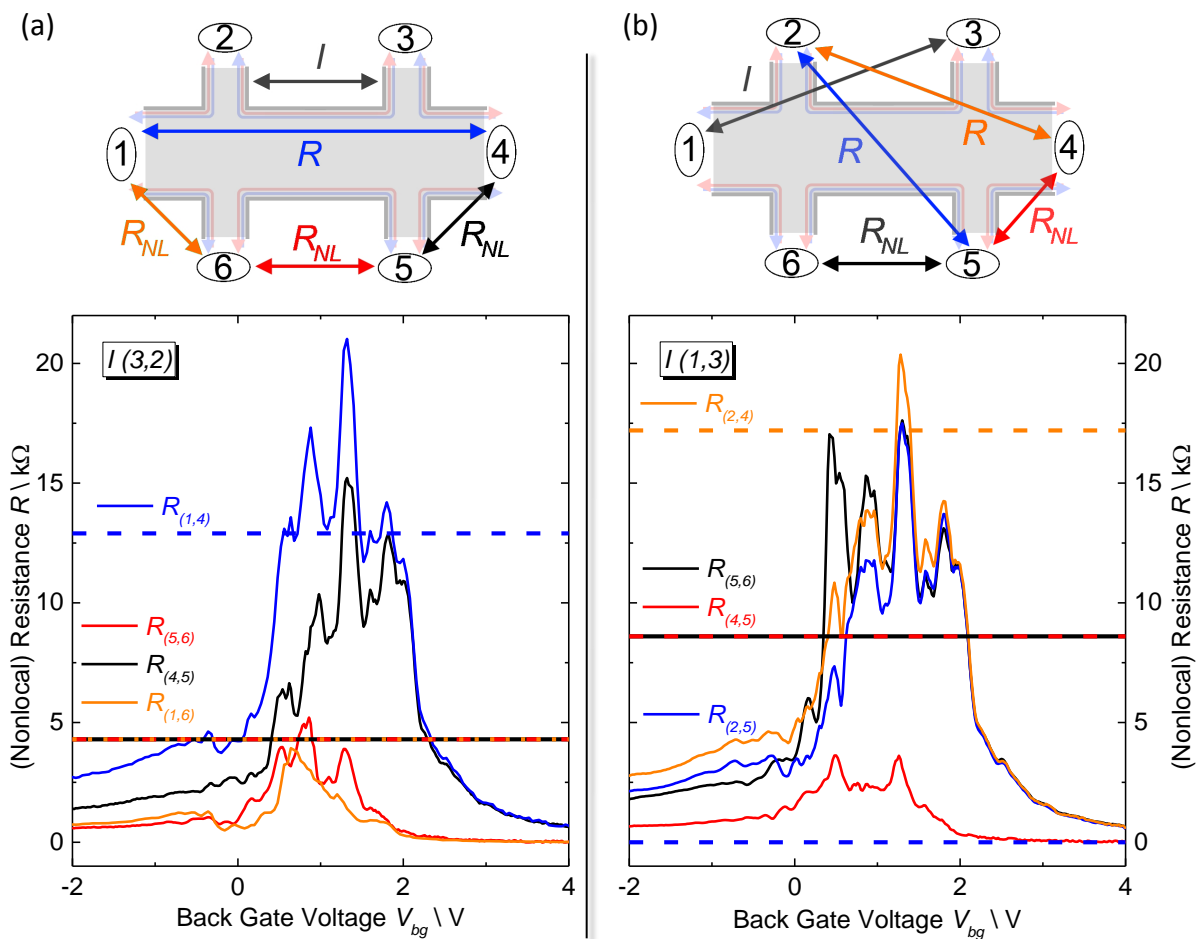


Figure 1.12: **Q2745 V**. Schematic of the Hall bar and measurement configurations on the top. Gap resistance as a function of back gate voltage on the bottom. For a current excitation along contacts 2,3 in (a) and between contacts 1,3 in (b). The expected Landau resistances in 6-terminal geometry is indicated with dashed lines. Their color matches the corresponding measurements and the their configuration in the schemes.

Q2745 V. Figure 1.12 shows resistances measured on Hall bar II of Q2745 V for two different current excitation configurations [(a) and (b)] as a function of back gate voltage. The expected Landau resistances in the 6-terminal configuration are marked as dashed lines in the color of the corresponding measurement and the arrows, indicating the voltage probes in the schematics. All measured signals exhibit fluctuations on the gap resistance in the QSH regime. Whereas some, also nonlocal, configurations remain close to their expected value [see R_{14} (blue), $R_{NL,56}$ (red) in (a)], others are far away from the predicted gap resistance. According to the 6-terminal Landau-Büttiker formalism, R_{25} (blue) in Figure 1.12 (b) is supposed to show no gap resistance at all. Nevertheless, the measured values in the QSH regime range from 10 to more than 17 k Ω .

The fact, that nonlocal resistances are measured, proves the Hall bar to have a QSH edge channel dominated transport. It is not surprising that the values from the 6-terminal Landauer-Büttiker formalism do not match to most resistances. As discussed on page 76, the puddle configuration and thereby the backscattering is dependent on the constantly modified size, carrier density and spin dephasing effects within the puddles. Describing the exact resistance evolution with Landauer-Büttiker would require information about the location and backscattering probability of each and every puddle at given gate voltages. A system with very few backscattering centers may be modelled to data. However, the more terminals are implemented, the more permutations of backscattering configurations are possible. Single gap resistances can thereby be fitted with a random number of terminals, but resistances all around the edges have to add up to one picture to fully explain the values within Landau-Büttiker. Here, they do not.

The features on resistances evolve once more at comparable gate voltages [see Fig. 1.12]. Interconnected by the QSH edge channels, the whole set of resistances is affected as the backscattering changes. The large amplitudes and their regular pattern of features might indicate a reappearance of backscattering reasons with gate voltage e.g. through Coulomb blockade or quantized densities within puddles.

The *Quantum Spin Hall Effect* is resumed, before the whole thesis is concluded in the *Summary*.

The novel mesa wet etch technique and the optimized lithography processes allow for micro structures with unprecedented carrier mobilities. However, not every sample exhibits an undisturbed QSH conductance. The protection against backscattering through time reversal symmetry is not as rigid as previously claimed. Potential inhomogeneities arising from intrinsic crystalline and extrinsic lithography irregularities cause local charge puddles in the QSH phase. Close to the edge and interacting with the QSH states they are discussed to enable backscattering. Small puddles with an odd number of electrons can be considered a magnetic (Kondo) impurity and cause a spin flip. In larger puddles, electrons can change their spin through interaction processes or spin-momentum coupling in the

presence of a Rashba field. The effective backscattering is thereby strongly modified with gate voltage. Interaction, tunneling and dephasing mechanisms as well as puddle size, density of states and Rashba fields are gate voltage dependent. In the complex interplay of these effects, longitudinal resistance values below and above $h/2e^2$ can be obtained in the presence of backscattering. The gate sweeps of the QSH resistance are not exactly quantized, their features are characteristic fingerprints of the potential landscape.

Only if close to $h/2e^2$, the temperature dependence of the average gap resistance proves the edge conductance to remain stable up to 11 K. Above, they follow a power law dependence with $\Delta R \propto T^\alpha$. While the resistance with minor deviations from the quantized value follows $\alpha = 1/4$, the temperature dependence of the resistances with large oscillating features on the QSH plateau in another sample can be fitted with $\alpha = 2$. Two different mechanisms dominate their QSH backscattering. However, none of the power laws confirms the proposed theories.

The distinct magnetic field dependence furthermore reinforces the assumption of two different dominant mechanisms. The gap resistance of the QSH signal with minor deviations remains dominated by the QSH edge channel transport up to the predicted band inversion lifting at B_c . But, an immediate increase of the fluctuations in the gap resistance of the other sample, prove its backscattering mechanism to be strongly dependent on magnetic field.

More statistics is required and will be obtained in further samples fabricated with *The Novel Micro Hall Bar Process*. They are crucial for a deeper understanding of the backscattering in QSH edge channels.

Summary and outlook

Summary

The presented thesis summarizes the results from four and a half years of intense lithography development on (Cd,Hg)Te/HgTe/(Cd,Hg)Te quantum well structures. The effort was motivated by the unique properties of this topological insulator. Previous work from Molenkamp et al. has proven that the transport through such a 2D TI is carried by electrons with opposite spin, counter-propagating in 1D channels along the sample edge. However, up to this thesis, the length of quantized spin Hall channels has never been reported to exceed 4 μm . Therefore, the main focus was put on a reproducible and easy-to-handle fabrication process that reveals the intrinsic material parameters.

Every single lithography step in macro as well as microscopic sample fabrication has been re-evaluated. In the *Development*, the process changes have been presented along SEM pictures, micrographs and, whenever possible, measurement responses.

We have proven the conventional ion milling etch method to damage the remaining mesa and result in drastically lower electron mobilities in samples of microscopic size.

The novel KI:I₂:HBr wet etch method for macro and microstructure mesa fabrication has been shown to leave the crystalline structure intact and result in unprecedented mobilities, as high as in macroscopic characterization Hall bars. Difficulties, such as an irregular etch start and slower etching of the conductive QW have been overcome by concentration, design and etch flow adaptations. In consideration of the diffusive regime, a frame around the EBL write field electrically decouples the structure mesa from the outside wafer. As the smallest structure, the frame is etched first and guarantees a non-different etching of the conductive layer during the redox reaction. A tube-pump method assures reproducible etch results with mesa heights below 300 nm. The PMMA etch mask is easy to strip and leaves a clean mesa with no redeposition. From the very first attempts, to the final etch process, the reader has been provided with the characteristics and design requirements necessary to enable the fabrication of nearly any mesa shape within an EBL write field of 200 μm .

Magneto resistance measurement of feed-back samples have been presented along the development chronology of wet etch method and subsequent lithography steps. With increasing feature quality, more and more physics has been revealed enabling detailed

evaluation of smallest disturbances. The following lithography improvements have been implemented. They represent a tool-box for high quality macro and microstructure fabrication on (CdHg)Te/HgTe of almost any kind.

- **The optical positive resist ECI 3027** can be used as wet and as dry etch mask for structure sizes larger than 1 μm . It serves to etch mesa structures larger than the EBL write field.
- **The double layer PMMA** is used for ohmic contact fabrication within the EBL write field. Its thickness allows to first dry etch the (Cd,Hg)Te cap layer and then evaporate the AuGe contact, in situ and self aligned. Because of an undercut, up to 300 nm can be metalized without any sidewalls after the lift-off. An edge channel mismatch within the contact leads can be avoided, if the ohmic contacts are designed to reach close to the sample and beneath the later gate electrode.
- **The MIBK cleaning step** prior to the gate application removes PMMA residuals and thereby improves gate and potential homogeneity.
- **The novel low T HfO₂ ALD process** enables insulator growth into optical and EBL lift-off masks of any resolvable shape. Directly metalized after the insulator growth, the self aligned method results in thin and homogeneous gate electrode reproducibly withholding gate voltages to ± 10 V.
- **The optical negative resist ARN 4340** exhibits an undercut when developed. Usable as dry etch mask and lift-off resist, it enables an in-situ application of ohmic contacts first etching close to the QW, then metalizing AuGe. Up to 500 nm thickness, the undercut guarantees an a clean lift-off with no sidewalls.

The undertaken efforts have led to micro Hall bar measurements with Hall plateaus and SdH-oscillations in up to now unseen levels of detail.

The gap resistance of several micro Hall bars with a clear QSH signal have been presented in *Quantum Spin Hall*. The first to exhibit longitudinal resistances close to the expected $h/2e^2$ since years, they reveal unprecedented details in features and characteristics. It has been shown that their protection against backscattering through time reversal symmetry is not as rigid as previously claimed. Values below and above 12.9 k Ω have been explained, introducing backscattering within the Landauer-Büttiker formalism of edge channel transport. Possible reasons have been discussed. Kondo, interaction and Rashba-backscattering arising from density inhomogeneities close to the edge are most plausible to explain features on and deviations from a quantized value. Interaction, tunneling and dephasing mechanisms as well as puddle size, density of states and Rashba Fields are gate voltage dependent. Therefore, features in the QSH signal are fingerprints of the characteristic potential landscape.

Stable up to 11 K, two distinct but clear power laws have been found in the higher tem-

perature dependence of the QSH in two samples. However, with $\Delta R = T^\alpha$, $\alpha = 1/4$ in one (QC0285) and $\alpha = 2$ in the other (Q2745), none of the predicted dependencies could be confirmed. Whereas, the gap resistances of QC0285 remains QSH channel dominated up to 3.9 T and thereby confirmed the calculated lifting of the band inversion in magnetic field. The gate-dependent oscillating features in the QSH signal of Q2745 immediately increase in magnetic field. The distinct field dependencies allowed the assumption of two different dominant backscattering mechanisms.

Resulting in undisturbed magneto transport and unprecedented QSH measurements, *The Novel Micro Hall Bar Process* has proven to enable the fabrication of a new generation of microstructures.

Outlook

The process adaptations developed in the frame of this work and presented in this thesis can be implemented in the fabrication of all samples on CdHgTe/HgTe wafers. Applied and adopted to any sample and experiment design, an increase in performance can be expected. Further samples with stable and reproducible QSH signals and undisturbed bulk transport properties will finally allow to examine the nature of the QSH states in more detail. Furthermore, it might enable using the unique properties of the QSH edge channels for possible Majorana detection in combination with a superconductor or as spin-current injector in spin-electronics. However, any of those applications require a deeper understanding of the backscattering mechanisms and the physics of QSH states. Therefore, more temperature, magnetic field but also a length dependent data is required. Here, two more lithography optimizations are proposed to possibly further increase the quality of samples and two experiment designs are presented to examine length dependence and backscattering mechanisms.

- **Pre framing** the EBL write field in an additional etching step before the actual mesa etching, will enable to define smallest mesa distances within the write field. Electrically decoupled from the outside wafer before the actual mesa etch step, the frame does not require to be the narrowest mesa-to-mesa distance in the design. Limited by the diffusive etch character, mesas separated by a small trench can be fabricated. The trench could then be filled with insulator and one mesa can be used as a side-gate for the other, e.g. in quantum point contacts (QPC).
- **Wet-chemical atomic layer etching (WALE)** might minimize the effects of the diffusive etch character and enable a much better depth control [93, 94]. If the oxidation and dissolution of material can be conducted in two different steps, accessible material oxidizes homogeneously thick on all surfaces and is likewise removed. The steps can then be repeated until the required etch depth is achieved. The etch result might exhibit no diffusive etch profile and the depth is independent from the mesa-to-mesa distance. If the depth resolution is small enough, this could also replace the ion milling step in the ohmic contact fabrication and allow a controlled and reproducible (Cd,Hg)Te cap layer removal. Ferromagnetic, superconducting and ohmic contacts could then be applied in a non-invasive and more accurate manor.
- **The length dependence of QSH edge channels** cannot reliably be examined in Hall bars of different lengths. Even if fabricated on the same piece of wafer, the results vary strongly from Hall bar to Hall bar. A simple method to obtain QSH

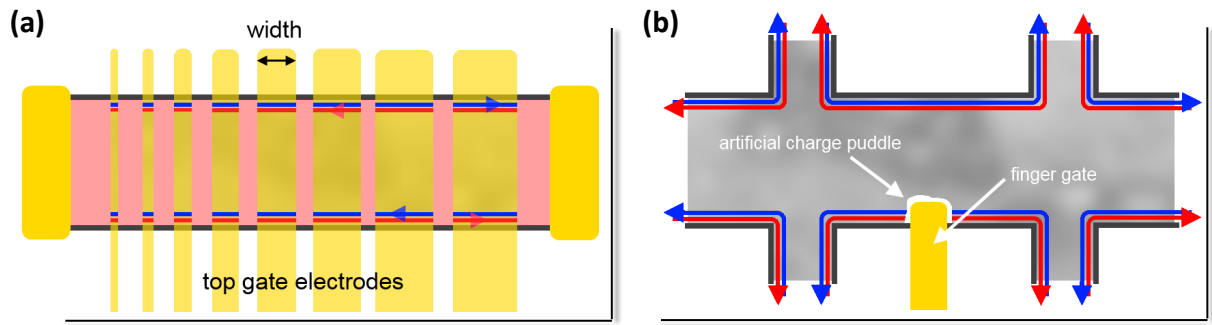


Figure 1.13: **(a)** Schematic of a sample design to determine the length dependence of QSH edge channels. **(b)** Schematic of a sample design with an artificial charge puddle created and controlled via a finger gate.

regimes of different length is schematically pictured in Fig. 1.13 **(a)**. Using a back gate, a mesa stripe can be tuned into the metallic regime. Individual top gate stripes of increasing width can then, stripe by stripe, be gated into the QSH regime. Highly conductive everywhere but the gated area, the 2-point resistance through the stripe will be dominated by the QSH regime beneath the top gate. If the width of the gate electrode exceeds the length of undisturbed QSH edge channel transport, the resistance increases.

- **An artificial backscatterer** can be introduced along the edge of a QSH sample using a so called finger-gate. Figure 1.13 **(b)** schematically pictures the situation. Instead of relying on the random distribution and size of charge puddles, the applied gate voltage might provide a knob to tune and examine the consequences of the artificial potential inhomogeneity at a given spot.

The proposed experiments are thereby only the tip of the iceberg of what could be realized with devices of stable QSH edge channel transport.

Zusammenfassung

In der vorliegenden Dissertation wurden die Ergebnisse von viereinhalb Jahren lithographischer Prozessentwicklung an (Cd,Hg)Te/HgTe/(Cd,Hg)Te Quantum Well Strukturen präsentiert. Motiviert wurde der Aufwand mit den einzigartigen Eigenschaften des zweidimensionalen Topologischen Isolators. In früheren Arbeiten von Molenkamp et al. ist gezeigt worden, dass der Stromtransport im Quantum Spin Hall (QSH) Regime durch zwei Randkanäle mit Elektronen entgegengerichteter Spin- und Propagationsrichtung erfolgt. Trotz der Vorhersage geschützten Randkanaltransports durch Zeit-Umkehr Invarianz, gab es bis zu der hier vorgenommenen Prozessoptimierung keine ungestörten Quantum Spin Hall Messungen oberhalb einer Länge von 4 μm . Deswegen wurde das Hauptaugenmerk der Entwicklung auf einen möglichst einfachen, reproduzierbaren und ungestörten Herstellungsprozess für QSH Mikrostrukturen gelegt.

Die Ergebnisse der vollständigen Überarbeitung jedes einzelnen Lithographie-Schrittes für marko- und mikroskopische Probenstrukturierung wurden in *Development* erläutert. Die Anpassungen wurden anhand von Elektronen-, Lichtmikroskop-aufnahmen und wann immer möglich auch Messungen motiviert, überprüft und für besser befunden.

Es wurde aufgezeigt, dass das bisher übliche Verfahren zum ätzen der Mesa mit beschleunigten Argon-Ionen das Material auch lateral beschädigt und mit drastisch reduzierten Elektronen-Beweglichkeiten in mikroskopischen Proben einhergeht.

Ein neuartiger KI:I₂:HBr nass-Ätzprozess hingegen, hat sich als nicht invasiv erwiesen. Ohne die Kristallstruktur zu zerstören lassen sich damit Mikrostrukturen herstellen, welche sich durch beispiellos hohe Beweglichkeiten und Signalgüte auszeichnen. Schwierigkeiten, wie der unregelmäßige Ätz-Start und das langsamere Ätzen der leitfähigen Schicht sind durch Konzentrations-, Design- und Flussanpassungen sukzessive gelöst worden. Unter Beachtung des diffusiven Ätz-Charakters, sorgt ein schmaler Rahmen um das Schreibfeld des Elektronen Mikroskops für eine elektrische Entkopplung der späteren Mesa innen, mit dem Elektronen-Reservoir außen. Damit wird sicher gestellt, dass die Leitfähigkeit des Quantentroges in der Redoxreaktion des Ätzens eine untergeordnete Rolle spielt. Durch den regulierbaren Fluss einer Schlauchpumpe lassen sich so reproduzierbar saubere Mesas auch unterhalb 300 nm Höhe herstellen. Die PMMA Ätzmaske kann rückstandsfrei entfernen werden.

Über die ersten Versuche, bis hin zum letztendlichen Prozess, wurde dem Leser dabei das

notwendige Wissen und Verständnis zur Durchführung der Mikrostrukturierung an die Hand gegeben. Unter Beachtung der charakteristischen Eigenheiten des nasschemischen Prozesses, lassen sich so nahezu alle Mesa-Formen innerhalb eines $200 \times 200 \mu\text{m}^2$ Schreibfeldes realisieren.

Anhand von Hall-Messungen an Kontrollproben, wurde die sukzessive Erhöhung der Probenqualität durch den Ätzprozess und die vollständige Überarbeitung der darauf folgenden Lithographie-Prozesse bewiesen. Mit mehr und mehr Physik in den Messungen haben sich selbst kleine Auswirkungen des Lithographie-Prozesses auf die Probeneigenschaften testen lassen. Die folgenden Verbesserungen tragen maßgeblich zu diesem Ergebnis bei. Hier angewendet auf Mikro-Hall-Bars, lassen sich die Prozesse für die Herstellung fast jedweder Struktur auf (Cd,Hg)Te/HgTe anpassen.

- **Der optische positiv Photo-Lack ECI 3027** kann sowohl als Nass- und auch Trockenätzmaske verwendet werden. Mit einer minimalen Auflösung größer $1 \mu\text{m}$ wurde er hier eingesetzt, um Strukturen um das Elektronenmikroskop-Schreibfeld zu ätzen.
- **Der PMMA Doppellagen Resist** ist dick und weist nach dem Entwickeln ein unterhöhltes Lackprofil auf. Dies erlaubt ihn zuerst zum Heranätzen und dann zum Metallisieren der Ohmschen Kontakte zu nutzen. Bis zu 300 nm Metall können dabei ohne Überhöhungen in-situ und selbstjustierend aufgebracht werden. Es wurde gezeigt, dass Kontakte nahe der Hall-Bar bis unterhalb der späteren Gate-Elektrode, in höheren Magnetfeldern nicht zu Störungen der Messung führen.
- **Der MIBK Reinigungs Schritt** vor dem Aufbringen der Gate-Elektrode entfernt PMMA Rückstände vorheriger Prozesse. In Hall-Messungen wurde gezeigt, dass dies die Homogenität des Gate-Einflusses deutlich verbessert.
- **Der neuartige Tieftemperatur HfO_2 ALD Prozess** ermöglicht Isolatorwachstum auf Photo-Resist und PMMA Lift-off Masken. Dies wiederum ermöglicht eine Gate-Metallisierung direkt im Anschluss. Dadurch lassen sich auch kleine Gate-Elektroden mit homogenem Potential-Einfluss herstellen, welche reproduzierbar Spannungen bis $\pm 10 \text{ V}$ aushalten.
- **Der optische negativ Photo-Lack ARN 4340** ermöglicht das Heranätzen und Metallisieren von Ohmschen Kontakten in Strukturgrößen größer $1 \mu\text{m}$. Das ebenfalls unterhöhlte Lackprofil erlaubt dabei die Aufbringung von bis zu 500 nm dicken Schichten und einen problemlosen Lift-off.

Die unternommenen Anstrengungen haben dabei zu den bisher Besten und Detailsreichsten Messungen von Hall-Plateaus und Shubnikov-De Haas Oszillationen in (Cd,Hg)Te/HgTe Mikrostrukturen geführt.

Messungen mit einem klaren QSH Signal im Längswiderstand von mehreren Mikro-Hall-

Bars wurden präsentiert. Nach jahrelangen Bemühungen weisen diese Proben erstmalig wieder einen Bandlücken-Widerstand nahe der erwarteten Quantisierung von zwei Randkanälen auf.

Es wurde aufgezeigt, dass die vermeintliche geschützten Randzustände durchaus rückstreuen. Mit der Implementierung von Streuern im Landauer-Büttiker Formalismus für Randkanaltransport lassen sich Abweichungen unter- und oberhalb der erwarteten $12.9 \text{ k}\Omega$ begründen. Als mögliche Ursachen wurden Dichte-Inhomogenitäten ausgemacht, welche in Kondo-, Wechselwirkungs- und Rashba-Rückstreu Prozessen resultieren. Im komplexen Zusammenspiel von Wechselwirkung, Tunnelprozessen und Spin-Dephasierung, der unbekanntem Verteilung von Inhomogenitäten, ihrer Größe und Dichte sowie der Feldabhängigkeit aller Parameter, hat sich keiner der diskutierten Mechanismen als dominant bewiesen. In noch nie dagewesenen Details, erwies sich die Gate- und Magnetfeldabhängigkeit des QSH Signals als ein Fingerabdruck der hintergründigen Potential-Landschaft.

Die Signale von zwei unterschiedlichen Proben sind Temperatur- und Magnetfeldabhängig untersucht worden. Dabei haben mehrere Argumente zu der Schlussfolgerung geführt, dass unterschiedliche Rückstreumechanismen in den Proben dominieren:

- Mit einem flachen QSH Plateau in der einen (QC0285), und in Gate-Spannung oszillierender Merkmale auf dem QSH Signal der anderen Probe (Q2745), zeigen sich erste Unterschiede bereits in den Gate-Messungen.
- In Temperatur-abhängigen Messungen erweist sich deren QSH Signal zwar als stabil bis 11 K, folgt dann aber $\Delta R = T^\alpha$ mit $\alpha = 1/4$ in QC0285 und $\alpha = 2$ in Q2745.
- Im Magnetfeld bleibt die Bandlücke in QC0285 bis zum kritischen Feld der Invertierungsaufhebung Randkanal-Transport dominiert. Die Oszillierenden Merkmale auf dem QSH Signal in Q2745 dagegen, reagieren schon auf kleine Felder mit einer Erhöhung im Widerstand.

Die unvergleichliche Qualität der hier präsentierten Hall-Messungen und QSH Signale und das bis ins letzte Detail optimierte Herstellungsverfahren, rechtfertigen es von einer neuen Generation an QSH Mikrostrukturen zu sprechen.

References

- [1] P. W. Shor “Polynomial-Time Algorithms for Prime Factorization and Discrete Logarithms on a Quantum Computer”, *SIAM J. Comput.* **26**, 5, 1484-1509 (1997).
- [2] J.-P. Aumasson “The impact of quantum computing on cryptography”, *Computer Fraud & Security* **6**, 8-11 (2017).
- [3] Article by S. Rich and B. Gellman “NSA seeks to build quantum computer that could crack most types of encryption”, *The Washington Post* January 2, (2014).
- [4] Article by D. Castelvecchi “Quantum computers ready to leap out of the lab”, *Nature* **541**, 9, (2017).
- [5] A. Yu. Kitaev “Fault-tolerant quantum computation by anyons”, *Ann. Phys. (N.Y.)* **303**, 2 (2003).
- [6] Article, “Computing with Quantum Knots”, *Scientific American* **294**, 56-63 (2006).
- [7] S. D. Sarma, M. Freedman, C. Nayak, Review “Majorana zero modes and topological quantum computation”, *npj Quantum Information* **1**, 15001, (2015).
- [8] L. Fu and C. L. Kane “Superconducting Proximity Effect and Majorana Fermions at the Surface of a Topological Insulator”, *Phys. Rev. Lett.* **100**, 036407 (2008).
- [9] L. Weithofer and P. Recher “Chiral Majorana edge states in HgTe quantum wells”, *New J. Phys.* **15**, 085008, (2013).
- [10] M. König, S. Wiedmann, C. Brüne, A. Roth, H. Buhmann, L. W. Molenkamp, X.-L. Qi, and S.-C. Zhang, “Quantum Spin Hall Insulator State in HgTe Quantum Wells”, *Science* **318**, 5851, pp. 766-770 (2007).

-
- [11] C. L. Kane and E. J. Mele “Quantum Spin Hall Effect in Graphene”, *Appl. Phys. Lett.* **95**, 226801 (2005).
- [12] B. A. Bernevig, T. L. Hughes and S.-C. Zhang “Quantum Spin Hall Effect and Topological Phase Transition in HgTe Quantum Wells”, *Science* **314**, 5806 (2006).
- [13] L. Fu and C. L. Kane “Topological insulators with inversion symmetry”, *Phys. Rev. B* **76**, 045302, (2007).
- [14] J. Chu and A. Sher, “Physics and properties of narrow gap semiconductors” Springer Verlag, (2008).
- [15] A. Roth, C. Brüne, H. Buhmann, L. W. Molenkamp, J. Maciejko, X.-L. Qi and S.-C. Zhang “Nonlocal Transport in the Quantum Spin Hall State”, *Science* **325**, 5938 (2010).
- [16] K. C.. Nowack, E. M. Spanton, M. Baenninger, M. König, J. R. Kirtley, B. Kalisky, C. Ames, P. Leubner, C. Brüne, H. Buhmann, L. W. Molenkamp, D. Goldhaber-Gordon and K. A. Moler, “Imaging currents in HgTe quantum wells in the quantum spin Hall regime”, *Nature Mat.* **12**, (2013)
- [17] S. Hart, H. Ren, T. Wagner, P. Leubner, M. Mühlbauer, C. Brüne, H. Buhmann, L. W. Molenkamp and A. Yacoby “Induced superconductivity in the quantum spin Hall edge”, *Nature Physics* **10**, 638-643, (2013).
- [18] C. Brüne, A. Roth, H. Buhmann, E. M. Hankiewicz, L. W. Molenkamp, J. Maciejko, X.L. Qi and S.C. Zhang “Spin polarization of the quantum spin Hall edge states”, *Nature Physics* **8**, 485-490 (2012).
- [19] Lingjie Du, I. Knez G. Sullivan and Rui-Rui Du “Robust Helical Edge Transport in Gated InAs/GaSb Bilayers”, *Appl. Phys. Lett.* **114**, 096802 (2015)
- [20] I. Knez and Rui-Rui Du “Evidence for Helical Edge Modes in Inverted InAs/GaSb Quantum Wells”, *Appl. Phys. Lett.* **107**, 136603 (2011)
- [21] Fanming Qu, Arjan A. Beukman, Stevan Nadj-Perge, Michael Wimmer, Binh-Minh Nguyen, Wei Yi, Jacob Thorp. Marko Sokolich, Andrey A. Kisilev, Michael J. Manfra, Charles M. Marcus, Leo P. Kouwenhoven “Electric and Magnetic Tuning Between the Trivial and Topological Phases in InAs/GaSb Double Quantum Wells”, *Appl. Phys. Lett.* **115**, 036803 (2015)

- [22] S. Tang, C. Zhang, D. Wong, Z. Pedramrazi, H.-Z. Tsai, C. Jia, B. Moritz, M. Claassen, H. Ryu, S. Kahn, J. Jiang, H. Yan, M. Hashimoto, D. Lu, R. G. Moore, C.-C. Hwang, C. Hwang, Z. Hussain, Y. Chen, M. M. Ugeda, Z. Liu, X. Xie, T. P. Devereaux, M. F. Crommie, S.-K. Mo et al. “Quantum spin Hall state in monolayer 1T'-WTe₂”, *Nature Physics* **13**, 683-687 (2017).
- [23] Z. Fei, T. Palomaki, S. Wu, W. Zhao, X. Cai, B. Sun, P. Nguyen, J. Finney, X. Xu and D. H. Cobden “Edge conduction in monolayer WTe₂”, *Nature Physics* **13**, 677-682 (2017).
- [24] C. Wu, B. A. Bernevig, and Shou-Cheng Zhang “Helical Liquid and the Edge of Quantum Spin Hall Systems”, *Phys. Rev. Lett.* **96**, 106401 (2006).
- [25] Cenke Xu and J. E. Moore “Stability of the quantum spin Hall effect: Effects of interactions, disorder, and Z₂ topology”, *Phys. Rev. B* **73**, 045322 (2006).
- [26] T. L. Schmidt, S. Rachel, F. v. Oppen, and L. I. Glazman “Inelastic Electron Backscattering in a Generic Helical Edge Channel”, *Phys. Rev. Lett.* **108**, 156402 (2012).
- [27] J. I. Väyrynen, M. Goldstein, and L. I. Glazman “Helical Edge Resistance Introduced by Charge Puddles”, *Phys. Rev. Lett.* **110**, 216402 (2013).
- [28] J. Maciejko, C. Liu, Y. Oreg, X.-L. Qi, C. Wu, and S.-C. Zhang. “Kondo Effect in the Helical Edge Liquid of the Quantu Spin Hall State”, *Phys. Rev. Lett.* **102**, 256803 (2009).
- [29] A. Pfeuffer-Jeschke, “Bandstruktur und Landau-Niveaus quecksilberhaltiger II-VI Heterostrukturen”, Dissertation , University of Würzburg (2000).
- [30] D. J. Chadi, J. P. Walter and M. L. Cohen “Reflectivities and Electronic Band Structures of CdTe and HgTe”, *Phys. Rev. B* **5**, 8, (1972).
- [31] V. S. Pribiag, A. J. A. Beukman, F. Qu, M. C. Cassidy, C. Charpentier, W. Wegscheider and L. P. Kouwenhoven “Edge-mode superconductivity in a two-dimensional topological insulator”, *Nature Nano.* **10**, 593-597 (2015)
- [32] E. H. Hall, “On a New Action of the Magnet on Electric Currents”, *Am. J. Math.* **2**, 3, pp. 287-292 (1879)
- [33] K. von Klitzing, “The quantized Hall effect”, *Rev. Mod. Phys.* **58**, 519 (1986).

-
- [34] N. W. Ashcroft and N. D. Mermin, “Solid State Physics”, Thomson Learning (1979).
- [35] A. Tzalenchuk, S. Lara-Avila, A. Kalaboukhov, S. Paolillo, M. Syväjärvi, R. Yakimova, O. Kazakova, T.J.B.M. Janssen, V. Fal’ko and S. Kubatkin “Towards a quantum resistance standard based on epitaxial graphene”, *Nat. Nano.* **5**, 3, pp. 186-189 (2010).
- [36] S. Hunklinger, “Festkörperphysik”, 2. Auflage, Oldenbourg Wissenschaftsverlag, München (2009).
- [37] P.-H. Chen, H.-Y Peng, C.-M. Hsieh and M. K. Chyu “The characteristic behavior of TMAH water solution for anisotropic etching on both Silicon substrate and SiO₂ layer”, *Sens. Actuators, A* **93**, 2 (2001)
- [38] Yue Kuo “Plasma enhanced chemical vapor deposited silicon nitride as a gate dielectric film for amorphous silicon thin film transistors - a critical review”, *Vacuum* **51**,4 (1998)
- [39] A. Boogaard, “Plasma-Enhanced Chemical Vapour Deposition of Silicon Dioxide”, Dissertation, University of Twente (2011).
- [40] Yue Kuo “Plasma-enhanced chemical vapour deposition of silicon nitride below 250 °C”, *Vacuum* **66**, 3-4, pp. 299-303 (2002)
- [41] M. Deminsky, A. Knizhnik, I. Belov, S. Umanskii, E. Rykova, A. Bagatur’yants, B. Potapkin, M. Stoker and A. Korokin “Mechanism and kinetics of thin zirconium and hafnium oxide film growth in an ALD reactor”, *Surf. Sci.* **549**, 1 (2004)
- [42] J. Robertson “High dielectric constant oxides”, *Phys. J. Appl. Phys.* **26**, pp. 265-291 (2004)
- [43] J. Hinz, H. Buhmann, M. Schäfer, V. Hock, C. R. Becker, and L. W. Molenkamp “Gate control of the giant Rashba effect in HgTe quantum wells”, *Semicond. Sci. Technol.* **21**, 4 (2006)
- [44] D. M. Hausmann and R. G. Gordon “Surface morphology and crystallinity control in the atomic layer deposition (ALD) of hafnium and zirconium oxide thin films” *J. Cryst. Growth* **249**, pp. 251-261 (2003)

- [45] W. Mantei, “Niedertemperatur ALD zum Wachstum von Al_2O_3 und HfO_2 ”, Bachelorarbeit, Universität Würzburg (2014).
- [46] M. R. Amirzada “Surface roughness analysis of SiO_2 for PECVD, PVD and IBD on different substrates”, *Appl. Nanosci.* **6**, pp. 215-222 (2016)
- [47] S. Arulkumaran, T. Egawa, H. Ishikawa, T. Jimbo, and M. Umeno “Investigations of $\text{SiO}_2/\text{n-GaN}$ and $\text{Si}_3\text{N}_4/\text{n-GaN}$ insulator-semiconductor interfaces with low interface state density”, *Appl. Phys. Lett.* **73**, 809 (1998)
- [48] H. K. Kuiken, J. J. Kelly and P. H. L. Notten “Etching Profiles at Resist Edges”, *J. Electrochem. Soc.* **1336**, pp. 1217-1226 (1986)
- [49] G. Tkachov, C. Thienel, V. Pinneker, B. Büttner, C. Brüne, H. Buhmann, L. W. Molenkamp, and E. M. Hankiewicz “Backscattering of Dirac Fermions in HgTe Quantum Wells with a Finite Gap”, *Appl. Phys. Lett.* **106**, 076802 (2011)
- [50] C. M. Stahle and C. R. Helms “Ion sputter effects on HgTe, CdTe and Cd-HgTe”, *J. Vac. Sci. Technol. A* **10**, 5, pp. 3239-3245 (1992)
- [51] J. L. Elkind “Ion mill damage in n-HgCdTe”, *J. Vac. Sci. Technol. B* **10**, 1460 (1992)
- [52] E. Belas, P. Höschl, R. Grill, J. Franc, P. Moravec, K. Lischka, H. Sitter and A. Toth “Ultrafast diffusion of Hg in $\text{Hg}_{1-x}\text{Cd}_x\text{Te}$ ($x \approx 0.21$)”, *J. Cryst. Growth* **138**, pp. 940-943 (1994)
- [53] E. Belas *et. al.* “Type conversion of p-(HgCd)Te using H_2/CH_4 and Ar reactive ion etching”, *Semicond. Sci. Technol.* **11**, pp. 1116-1120 (1996)
- [54] E. Belas, J. Franc, A. Toth, P. Moravec, R. Grill, H. Sitter and P. Höschl “Determination of the migration energy of Hg interstitials in (HgCd)Te from ion milling experiments”, *J. Cryst. Growth* **159**, pp. 1117-1122 (1996)
- [55] R. Haakenaasen, T. Colin, H. Steen and L. Trosdahl-Iversen “Electron Beam Induced Current Study of Ion Beam Milling Type Conversion in Molecular Beam Epitaxy Vacancy-Doped $\text{Cd}_x\text{Hg}_{1-x}\text{Te}$ ”, *J. Electron. Mater.* **29**, 6 (2000)
- [56] P. W. Leech, P. J. Gwynn and M. H. Kibel “A selective etchant for $\text{Hg}_{1-x}\text{Cd}_x\text{Te}$, CdTe and HgTe on GaAs”, *Appl. Surf. Sci.* **37**, pp. 291-298 (1989).

-
- [57] P. W. Leech, M. H. Kibel and P. J. Gwynn “The Chemical Etching of II-VI/GaAs Heterostructures in Aqueous I:KI:HBr Solutions”, *J. Electrochem. Soc.* **127**, 2 (1990).
- [58] R. Tenne, R. Brener, r. Triboulet “Chemical modifications of $\text{Hg}_{0.1}\text{Cd}_{0.9}\text{Te}$ surfaces: Analysis with Auger electron spectroscopy”, *J. Vac. Sci. Technol., A* **7**, 2570 (1989).
- [59] G. Wang, Y. Meir and Y. Gefen “Spontaneous Breakdown of Topological Protection in Two Dimensions”, *Phys. Rev. Lett.* **118**, 046801 (2017)
- [60] J. Schneider “Transportanomalien und spinabhängige Effekte in Hg-Quantentrogstrukturen”, *Diplomarbeit, Universität Würzburg* (2007)
- [61] R. J. F. Hughest, J. T. Nicholls, J. E. F. Frost, E. H. Linfield, M. Pepper, C. J. B. Ford, D. A. Ritchie, G. A. C. Jones, E. Kogan and M. Kaveh “Magnetic-field-induced insulator-quantum Hall-insulator transition in a disordered two-dimensional electron gas”, *J. Phys.: Condens. Matter* **6**, pp. 4763-4770, (1994)
- [62] E. Shimshoni “Classical versus quantum transport near quantum Hall transitions”, *Phys. Rev. B* **60**, 15, (1999).
- [63] E. Shimshoni, A. Auerbach, A. Kapitulnik “Transport through Quantum Melts”, *Phys. Rev. B* **80**, 15, (1998).
- [64] L. P. Pryadko and A. Auerbach “Hall Resistivity and Dephasing in the Quantum Hall Insulator”, *Phys. Rev. B* **82**, 6, (1999).
- [65] R. Joynt and R. E. Prange “Conditions for the quantum Hall Effect”, *Phys. Rev. B*, **29**, 6, (1984)
- [66] B. I. Halperin “Quantized Hall conductance, current-carrying edge states, and the existence of extended states in a two-dimensional disordered potential”, *Phys. Rev. B* **25**, 4, (1982).
- [67] A. H. MacDonald “Quantized Hall Effect and edge currents”, *Phys. Rev. B* **29**, 1616, (1984).
- [68] J. K. Jain and S. A. Kivelson “Landauer-type formulation of quantum-Hall transport: Critical currents and narrow channels”, *Phys. Rev. B* **37**, 8, (1988).

- [69] L. A. Ponomarenko, D. T. N. de Lang, A. de Visser, V. A. Kulbachinskii, G. B. Galiev, H. Künzel and A. M. M. Pruisken “The effect of carrier density gradients on magnetotransport data measured in Hall bar geometry”, *Solid State Commun.* **130**, pp 705-710, (2004).
- [70] B. Karmakar, M. R. Gokhale, A. P. Shah, B. M. Arora, D. T. N. de Lang, A. de Visser, L. A. Ponomarenko, A. M. M. Pruisken “The effects of macroscopic inhomogeneities on the magnetotransport properties of the electron gas in two dimensions”, *Physica E* **24**, pp 187-210, (2004).
- [71] S. Washburn, A. B. Fowler, H. Schmid and D. Kern “Quantized Hall Effect in the Presence of Backscattering” *Phys. Rev. Lett.* **61**, 24, (1988)
- [72] C. Brüne, A. Roth, H. Buhmann, E. M. Hankiewicz, L. W. Molenkamp, J. Maciejko, X.L. Qi and S.C. Zhang, Supplementary Material “Spin polarization of the quantum spin Hall edge states”, *Nature Physics* **8**, 485-490 (2012).
- [73] P. A. Lee and A. D. Douglas Stone “SU(2) Universal Conductance Fluctuations in Metals”, *Phys. Rev. Lett.* **55**, 15 (1985).
- [74] M. Mühlbauer “Nanolithography on Mercure Telluride”, *Dissertation, University of Wuerzburg* (2015)
- [75] M. Parikh and D. F. Kyser “Energy deposition functions in electron resist films on substrates” *J. Appl. Phys.* **50**, 2, (1979)
- [76] X. Dai, T. L. Hughes, X.L. Qi, Z. Fang and S.C. Zhang “Helical edge and surface states in HgTe quantum wells and bulk insulators”, *Phys. Rev. B* **77**, 12, 125319 (2008).
- [77] P. Leubner, “Strain-engineering of the Topological Insulator HgTe”, PhD Thesis, University of Wuerzburg (2016)
- [78] M. Büttiker “Absence of backscattering in the quantum Hall effect in multi-probe conductors”, *Phys. Rev. B* **38**, 14 (1988).
- [79] B. L. Altshuler, I. L. Aleiner and V. I. Yudson “Localization at the Edge of a 2D Topological Insulator by Kondo Impurities with Random Anisotropies”, *Phys. Rev. Lett.* **102**, 256803 (2009).
- [80] R. Winkler “Rashba spin splitting in two-dimensional electron and hole systems”, *Phys. Rev. B* **62**, 7 (2000).

-
- [81] A. Ström, H. Johannesson, and G. I. Japaridze “Edge Dynamics in a Quantum Spin Hall State: Effects from Rashba Spin-Orbit Interaction”, *Phys. Rev. Lett.* **104**, 256804 (2010).
- [82] J. I. Väyrynen, M. Goldstein, Y. Gefen and L. I. Glazman “Resistance of helical edges formed in a semiconductor heterostructure”, *Phys. Rev. B* **90**, 115309 (2014).
- [83] F. Geissler, F. Crepin, and B. Trauzettel “Random Rashba spin-orbit coupling at the quantum spin Hall edge”, *Phys. Rev. B* **89**, 235136 (2014).
- [84] X. C. Zhang, A Pfeuffer-Jeschke, K. Ortner, V. Hock, H. Buhmann, C. R. Becker, and G. Landwehr “Rashba splitting in n-type modulation-doped HgTe quantum wells with an inverted band structure”, *Phys. Rev. B* **63**, 245305 (2001).
- [85] Y. S. Gui, C. R. Becker, n. Dai, j. Liu, Z. j. Qui, E. G. Novik, M. Schäfer, X. Z. Shu, J. H. Chu and H. Buhmann, “Giant spin-orbit splitting in a HgTe quantum well”, *Phys. Rev. B* **70**, 115328 (2004).
- [86] G. Tkachov, C. Thienel, V. Pinneker, B. Büttner, C. Brüne, H. Buhmann, L. W. Molenkamp, and E. M. Hankiewicz “Backscattering of Dirac Fermions in HgTe Quantum Wells with a Finite Gap”, *Phys. Rev. Lett.* **106**, 07682 (2011).
- [87] C. Ames, “Molecular Beam Epitaxy of 2D and 3D HgTe, A Topological Insulator”, PhD Thesis, University of Wuerzburg (2015)
- [88] S.S.Krishtopenko, I.Yahniuk, D.B.But, V.I.Gavrilenko, W.Knap, and F.Teppe “Pressure- and temperature- driven phase transitions in HgTe quantum wells”, *Phys. Rev. B* **94**, 245402 (2016).
- [89] X.-L. Qi, T. L. Hughes and S.-C. Zhang “Topological field theory of time-reversal invariant insulators”, *Phys. Rev. B* **78**, 195424 (2008).
- [90] M. Z. Hazan and C. L. Kane “Colloquium: Topological insulators”, *Rev. Mod. Phys.* **82**, 3045-3067 (2010).
- [91] G. Tkachov, and E. M. Hankiewicz “Ballistic Quantum Spin Hall State and Enhanced Edge Backscattering in Strong Magnetic Fields”, *Phys. Rev. Lett.* **104**, 166803 (2010).

- [92] M. Büttiker “Absence of backscattering in the quantum Hall effect in multi-probe conductors”, *Phys. Rev. B* **38**, 14 (1988).
- [93] K. J. Kanarik, T. Lill, E. A. Hudson, S. Sriraman, S. Tan, J. Marks, V. Vahedi, and R. A. Gottscho “Overview of atomic layer etching in the semiconductor industry”, *J. Vac. Sci. Technol. A* **33**, 020802 (2015).
- [94] D. H. van Dorp, S. Arnauts, F. Holeyteyns, and S. De Gendt “Wet-Chemical Approaches for Atomic Layer Etching of Semiconductors: Surface Chemistry, Oxide Removal and Redoxidation of InAs (100)”, *ECS J. Solid State Sci.* **4**, 6 (2015).

Acknowledgments

The results presented in this thesis are not the work of one single person. Many people have contributed to their successful realization. I want to thank:

- Prof. Dr. Laurens W. Molenkamp for accepting me at his chair and providing the infrastructure of Experimental Physics III,
- Prof. Dr. Hartmut Buhmann for giving me the opportunity to work in his Quantum Transport group, for supervising my doctoral dissertation and his continuous moral support,
- Volkmar Hock, Petra Wolf-Müller, Carmen Bundschuh, Martin Zipf, Dr. Claus Schumacher, Angelika Berger, Roland Ebert and Cornelius Ziga for their (technical) assistance and daily effort to keep everything running,
- Dr. Erwann Bocquillon, one of the best scientist to my knowledge, for his advice, moral support and friendship,
- Dr. Christoph Brüne for his consult, expertise and company for many years,
- Dr. Tanja Borzenko for the introduction into the cleanroom,
- the Master students Kristina Kletzel, Raimund Schlereth, Florian Wallaschowski, Nicolai Bunzmann and Tobias Mauder as well as the Bachelor students Willi Mantei, Lisa Schraut-May, Lucas Gold, Johannes Brehm and Jonas Strunz and for their valuable input to this thesis,
- my colleagues and friends Matthias Mühlbauer, Holger Thierschmann, Cornelius Thienel, Phillip Leubner, David Mahler, Jonas Wiedenmann, Simon Hartinger, Christopher Ames, Graciely Santos and Martin Baussenwein for their contributions, moral support, enriching discussions and help,
- Prof. Dr. Hartmut Buhmann as well as Anna Menth for proofreading the thesis,
- and Pragya Shekar and Dr. Saquib Shamim who will continue the research on this project. I am happy to know it in such talented hands.

Special thanks go to my good friends and office colleagues Maximilian Kessel and Andreas Budewitz. I would not have succeeded without you.

Last but not least i want to express my heartfelt thanks to my family and friends who have been supporting me tremendously throughout the years of my study and work.

List of Publications

- **K. Bendias** , S. Shamim, O. Herrmann, A. Budewitz, P. Shekhar, P. Leubner, J. Kleinlein, E. Bocquillon, H. Buhmann, and L.W. Molenkamp “High Mobility HgTe Microstructures for Quantum Spin Hall Studies”, *Nano Lett.* **18**,**8**, 4831-4836 (2018).
- A. Josta, **M. Bendias**, J. Böttcher, E. Hankiewicz, C. Brüne, H. Buhmann, L.W. Molenkamp, J.C. Maan, U. Zeitler, N. Hussey, and S. Wiedmann “Electron–hole asymmetry of the topological surface states in strained HgTe”, *Phys. Rev. Materials* **2**, 0 (2018).
- A. Budewitz, **K. Bendias**, P. Leubner, T. Khouri, S. Shamim, S. Wiedmann, H. Buhmann, and L.W. Molenkamp “Quantum anomalous Hall effect in Mn doped HgTe quantum wells”, arXiv:1706.05789v1, (2017).
- V. Dziom, A. Shuvaev, A. Pimenov, G.V. Astakhov, C. Ames, **K. Bendias**, J. Böttcher, G. Tkachov, E.M. Hankiewicz, C. Brüne, H. Buhmann, and L.W. Molenkamp “Observation of the universal magnetoelectric effect in a 3D topological insulator”, *Nature Communications* **8**, 15197 (2017).
- A. Inhofer, S. Tchoumakov, B.A. Assaf, G. Fève, J.M. Berroir, V. Jouffrey, D. Carpentier, M.O. Goerbig, B. Plaçais, **K. Bendias**, D.M. Mahler, E. Bocquillon, R. Schlereth, C. Brüne, H. Buhmann, and L.W. Molenkamp “Observation of Volkov-Pankratov states in topological HgTe heterojunctions using high-frequency compressibility”, *Phys. Rev. B* **96**, 195104 (2017).
- T. Khouri, **M. Bendias**, P. Leubner, C. Brüne, H. Buhmann, L. W. Molenkamp, U. Zeitler, N. E. Hussey, and S. Wiedmann “High-temperature quantum Hall effect in finite gapped HgTe quantum wells”, *Phys. Rev. B* **93**, 125308 (2016).